Doctoral Thesis

Interface Engineering of Semiconductor Nanomaterials for Efficient Optoelectronic Devices

Hyeonjung Kim

School of Energy and Chemical Engineering
(Chemical Engineering)

Ulsan National Institute of Science and Technology

2023

Interface Engineering of Semiconductor Nanomaterials for Efficient Optoelectronic Devices

Hyeonjung Kim

School of Energy and Chemical Engineering
(Chemical Engineering)

Ulsan National Institute of Science and Technology

Interface Engineering of Semiconductor Nanomaterials for Efficient Optoelectronic Devices

A thesis/dissertation submitted to
Ulsan National Institute of Science and Technology
in partial fulfillment of the
requirements for the degree of
Doctor of Philosophy

Hyeonjung Kim

12.15.2022 of submission
Approved by

_____

Advisor
Jongnam Park

Interface Engineering of Semiconductor Nanomaterials for Efficient Optoelectronic Devices

Hyeonjung Kim

This certifies that the thesis/dissertation of Hyeonjung Kim is approved.

12.15.2022 of submission

Signature

_____

Advisor: Jongnam Park

Signature

_____

Jin Young Kim

Signature

_____

Tae-Hyuk Kwon

Signature

_____

Myoung Hoon Song

Signature

_____

Yu Jin Jung

Abstract

Optoelectronic devices are essential components that exploit electromagnetic radiation based on light-matter interactions and have been developed with the advance of nanotechnology. In particular, communication between materials at interfaces is crucial because optoelectronic devices are made up of multilayer structures. Interface/surface engineering allows the regulation of physical stress, energy barrier, interfacial band alignment, and defect passivation, all of which are directly related to the performance of devices. The arrangement of energy levels affects charge transport and can be adjusted by the dipole moment on the surface of nanomaterials. Defect passivation on the interface/surface of the materials reduces trap states that induce charge accumulation as a charge injection barrier or act as nonradiative recombination centers. These effects are prominent in nanomaterials because of their high surface-area-to-volume ratio. Furthermore, since the nanomaterial layer of optoelectronics is a microscopic assembly, surface engineering can regulate the communication between nanomaterials by changing the interparticle distance and packing density. This dissertation describes surface engineering strategies for semiconductor nanomaterials to improve the efficiency of optoelectronic devices.

Chapter 2 demonstrates the interface engineering between the graphene electrode and the hole transport layer for organic solar cells. A thin layer of norepinephrine, an amphiphilic catecholamine derivative, is applied to the graphene electrode as a hydrophilic surface modifier to enable efficient surface modification without significantly decreasing the optical transmittance or the electrical conductivity. The power conversion efficiency of organic solar cells fabricated with this poly(norepinephrine)-coated graphene electrode is 7.93%, close to that of the ITO-based reference device with a power conversion efficiency of 8.73%.

In Chapter 3, we demonstrate the surface engineering of InP@ZnSeS quantum dots for a color filter. Phenylethyl mercaptan ligands are used as surface modifiers, substituting the original oleic acid ligands. In the propylene glycol monomethyl ether acetate solvent, more than 75% of photoluminescence quantum yields are retained without a peak shift in the emission spectrum during the ligand exchange procedure. Surface-engineered quantum dots show high colloidal stability in propylene glycol monomethyl ether acetate for more than one month under ambient conditions.

Chapter 4 demonstrates the interface engineering between $CsPbBr_3$ and Cs_4PbBr_6 perovskite nanocrystals for blue light-emitting diodes. Highly emissive blue $CsPbBr_3$ quantum dots are developed by controlling the reactivity of metal precursors. *In situ* generated Cs_4PbBr_6 nanocrystals eliminate the surface defects of $CsPbBr_3$ quantum dots, resulting in high colloidal and thermal stability. The fabricated blue light-emitting diode shows an external quantum efficiency of 4.65% at 480 nm and excellent spectral stability under operational conditions.

As previously discussed, we have developed a catechol-based nanocoating method, a thiol-based ligand exchange method, and a surface reconstruction strategy for perovskite materials. Our strategies can accelerate the development of a wide range of optoelectronic applications thanks to their versatility.

Contents

List of Figures

Chapter 1.

the QD diameter is reduced from 6 to 2 nm. Reproduced with permission from ref. 16. Copyright © 2012, Royal Society of Chemistry.

Figure 1.7. Overview of the main features of polymeric nanoparticles. Reproduced with permission from ref. 22. Copyright © 2012, Frontiers Media SA.

Figure 1.8. Changes in the surface area to volume ratio of a cube. The smaller the cube (object), the higher surface area to volume ratio, which has a key role in the interaction of a nanoscale material with its surrounding environment. Reproduced with permission from ref. 23. Copyright © 2019, Springer Nature.

Figure 1.9. The qualitative behavior of the size-dependent coercivity of magnetic particles. The magnetic behavior of superparamagnetic nanoparticles is demonstrated by the solid line, while ferromagnetic particles are presented by dashed lines. Here H denotes the applied magnetic field strength and M is the measured magnetization. Reproduced with permission from ref. 26. Copyright © 2011, IOP Publishing Ltd.

Figure 1.10. Experimental and theoretical values of the melting-point temperature of gold particles. Reproduced with permission from ref. 28. Copyright © 1976, American Physical Society.

Figure 1.11. Amphiphilic Polymer encapsulation of the nanocrystals. The hydrophobic alkyl chains of the polymer intercalate with the surfactant coating. The anhydride rings are located on the surface of the polymer-coated nanocrystal. The amino end groups of the cross-linker molecule open the rings and link the individual polymer chains. The surface of the polymer shell becomes negatively charged, stabilizing the particles in water by electrostatic repulsion. Reproduced with permission from ref. 33. Copyright © 2004, American Chemical Society.

Figure 1.12. (a) Schematic illustration for the synthesis of quantum dots@SiO_2 using Stöber approach. Reproduced with permission from ref. 34. Copyright © 2014, The Royal Society of Chemistry. (b) Schematic representation of the incorporation mechanism of hydrophobic quantum dots in silica spheres by the reverse microemulsion method. (c) TEM images of quantum dots (6.4 ± 0.8 nm) in silica spheres of 37.2 ± 1.5 nm in diameter; inset shows a magnification of the same sample. Reproduced with permission from ref. 35. Copyright © 2008, American Chemical Society.

Figure 1.13. The covalent bond classification of L, X, and Z ligands. Note that the ligands are always classified in their neutral forms. L-type ligands (2-electron donors) are identified as Lewis bases, X-type ligands (1-electron donors) as radicals, and Z-type ligands (0-electron donors) as Lewis acids. Reproduced with permission from ref. 43. Copyright © 2014, American Chemical Society.

Figure 1.14. (a) Sketch of a CdSe NC capped with $Sn_2S_6^{4-}$ ions. (b) Stable colloidal solutions of 3.6 nm CdSe NCs capped with various metal chalcogenide complexes in hydrazine. (c) Stable colloidal solutions obtained by combining $(N_2H_5)_4Sn_2S_6$ (d) CdSe-$Sn_2S_6^{4-}$ nanoparticles dispersed in various solvents. (e) Photograph of photoluminescence excited by an ultra-violet lamp. (f) z-Potential measured for $Sn_2S_6^{4-}$ capped CdSe NCs in hydrazine. (g) Size histogram obtained from dynamic light scattering for 8 nm CdSe-$Sn_2S_6^{4-}$ nanocrystals in hydrazine. Reproduced with permission from ref. 44. Copyright © 2009, American Association for the Advancement of Science.

Figure 1.15. Modular design of surface ligands for biocompatible nanomaterials. (a) Anchor links capping molecules to the crystallite through hydrophobic interaction with native ligands or through atoms that bind directly to the nanocrystal surface. (b) Stabilizer region incorporates polyethylene glycol or zwitterionic chains that strongly bind water molecules to impart hydrophilicity and prevent nonspecific adsorption. (c) Capping molecules may feature reactive groups serving as a tether point for covalent conjugation to biofunctional molecules after ligand exchange. (d) The biofunctional units can offer targeting, therapeutic or sensing capability. Reproduced with permission from ref. 46. Copyright © 2016, Springer Nature.

Figure 1.16. (a) A mussel is shown attached to a sheet of mica. One of its plaques (red circle) is enlarged as a schematic drawing to illustrate the approximate distribution of known proteins. Reproduced with permission from ref. 47. Copyright © 2010, The American Society for Biochemistry and Molecular Biology, Inc. (b) Structural formula of the mussel foot proteins, mfp-5 showing the alternating amino acids that contain amine (blue) and catechol (red) units in their side chains. Reproduced with permission from ref. 48. Copyright © 2014, Wiley-VCH. (c) A schematic illustration of thin film deposition of polydopamine by dip-coating an object in an alkaline dopamine solution. Possible structural evolution and polymerization mechanisms of dopamine. Reproduced with permission from ref. 49. Copyright © 2007, American Association for the Advancement of Science.

Figure 1.17. Types of optoelectronic devices. Reproduced with permission from ref. 53. Copyright © 2020, Frontiers Media S.A.

Figure 1.18. (a) Schematic depicting the device structure of an organic light-emitting diode (OLED) and band diagram of the OLED. (b) Typical current–voltage characteristics of an OLED. (c) Schematic depicting the device structure of an organic photodiode (OPD) and photovoltaic (OPV), and diagrams of the OPD and OPV. (d) Typical current–voltage characteristics of an OPD (top) and OPV (bottom). Reproduced with permission from ref. 54. Copyright © 2021, Elsevier B.V.

Figure 1.19. (a) Scheme of the two-step surface modification of InAs QDs and Energy levels ECB, EVB, and EF (vs. the vacuum level) of InAs QD films, deduced from UPS measurements.

(ref. 55) (b) Complete energy level diagrams of PbS QDs exchanged with the various ligands. Reproduced with permission from ref. 56. Copyright © 2014, American Chemical Society. (c) Dipole moments of TP, 4-MTP, and 4-DMATP molecules, and energy level diagram of interface between QDs and hole transport part based on measured VBM of QDs in all-solution-processed inverted-structure green QLEDs. Reproduced with permission from ref. 57. Copyright © 2020, Wiley-VCH.

Figure 1.20. (a) Multilayered device schematic of all-solution-processed red QLED and (b) cross-sectional TEM image of a representative device integrated with 3 mmol-ZA-ZMO NP-based ETL. (c) Energy band levels, (d) current density−voltage, (e) luminance−current density, and (f) EQE−current density of red QLEDs integrated with p-ZMO and a series of acrylate-functionalized ZMO ETLs. Reproduced with permission from ref. 58. Copyright © 2022, American Chemical Society.

Figure 1.21. Schematic representation of different preparations for semiconductive NCs films (a) Solid-state ligand exchange: the NCs are first deposited on substrate and then ligand exchanged. The cracks formed in the bottom layer can be filled or covered by the subsequent layers. (b) Solution-phase ligand exchange: the ligand exchange process is conducted in solution. Then, the exchanged NC ink is dispersed in solvents such as dimethylformamide, formamide, and butylamine, which can be deposited into solid film directly. (c) Advanced solid-state ligand exchange: the NC mixture (dots and dimers) dispersed in nonpolar solution (hexane, octane etc.) is deposited on a substrate, which is then ligand exchanged to obtain crack-free, thick, and semiconductive NC film in only 1 step. Reproduced with permission from ref. 64. Copyright © 2020, Cell Press.

Figure 1.22. (a) Schematic illustration of PDA-sensitized solar cells showing the photoinduced charge transfer process. Reproduced with permission from ref. 66. Copyright © 2012, Wiley-VCH. (b) Possible binding modes for anchoring groups on TiO_2 and molecular structures of porphyrin sensitizers. Reproduced with permission from ref. 67. Copyright © 2019, Wiley-VCH.

Figure 1.23. (a) Schematic representation of type-I DSSC and type-II DSSC, (b) Chemical structures of D–π–Cat dye sensitizers YM-1, YM-2 and YM-3. Reproduced with permission from ref. 68. Copyright © 2014, The Royal Society of Chemistry. (c) Electron-injection pathway from the dye to the CB of the TiO_2 electrode for a type-II DSSC based on CAT dye and a type-II DSSC based on CAT-PET dye. (d) Chemical structures of CAT and CAT-PET dyes with various substituents. Reproduced with permission from ref. 69. Copyright © 2017, The Royal Society of Chemistry.

Figure 1.24. (a) Molecular structures of catechol derivatives. (b) Typical *J–V* curves of Pero-SCs with neat PEDOT:PSS (black, empty square), and DOPA- (red, empty circle), NE- (blue, triangle) and DOBD-PEDOT:PSS (green, solid triangle) as HTLs. (c) The size analysis of the crystal grains in the perovskite films on the neat/doped PEDOT:PSS. Reproduced with permission from ref. 70. Copyright

Figure 1.25. (a) Considerable differences in doping of PEDOT:PSS and DA-PEDOT:PSS: DA semiquinone radicals yield a greater electron donating effect for trap passivation. (b) Potential passivation effect: interactions between undercoordinated Pb atoms on the perovskite crystal and DA-PEDOT:PSS with amino and hydroxyl groups. Reproduced with permission from ref. 71. Copyright © 2018, Wiley-VCH.

Figure 1.26. (a) The molecular structure of PM6, Y6, and PNDIT-F3N. (b) Schematic energy level diagrams of the materials and device structure of the OSCs. (c) *J–V* and (e) IPCE curves of the devices with the as-cast PM6:Y6 system. (d) *J–V* and (f) IPCE curves of the devices with optimized PM6:Y6 system. Reproduced with permission from ref. 72. Copyright © 2020, Wiley-VCH.

Figure 1.27. (a) Schematic diagram of the dopamine self-assembled monolayer between SnO_2 ETL and perovskite, (b) Best PCE of the devices with different DA treatment times and (c) histogram of efficiencies among 20 devices. (d) *J−V* curves measured under reverse and forward voltage scanning and (e) EQE of the devices deposited on SnO_2 ETL with or without a DA SAM modification. Reproduced with permission from ref. 73. Copyright © 2018, American Chemical Society.

Figure 1.28. (a) Scheme of perovskite crystal structure. Reproduced with permission from ref. 75. Copyright © 2014, Springer Nature. (b) Near unity photoluminescence quantum yield of CsPbX3 (X=Cl, Br, and I) nanocrystals (NCs). Reproduced with permission from ref. 76. Copyright © 2019, Wiley-VCH. (c) Emission from CsPbX3 NCs (black data points) plotted on CEI chromaticity coordinates and compared to most common color standards. Reproduced with permission from ref. 77. Copyright © 2015, American Chemical Society. (d) Anion exchange reactions on CsPbX3 NCs. Reproduced with permission from ref. 78. Copyright © 2015, American Chemical Society. (e) Solution processes for preparing perovskite films. Reproduced with permission from ref. 79. Copyright © 2015, The Royal Society of Chemistry. (f) Schematics comparing electronic structures that are defect-intolerant and defect-tolerant. Reproduced with permission from ref. 80. Copyright © 2017, American Association for the Advancement of Science.

Figure 1.29. (a) Schematic illustrations of single-layered $CsPbBr_3$, bilayered $CsPbBr_3$/MABr, and quasi-core/shell $CsPbBr_3$/MABr structures, all fabricated on ITO substrates. (b) Photographs of the three as-prepared perovskite films under ultraviolet light. (c) SIMS depth analysis of the as-prepared quasi-core/shell $CsPbBr_3$/MABr structure on ITO glass. (d) Cross-sectional TEM image of the quasi-core/shell $CsPbBr_3$/MABr structure on PEDOT:PSS. White arrows indicate the MABr shell (the grain boundary). Reproduced with permission from ref. 86. Copyright © 2018, Springer Nature.

Figure 1.30. Schematic of LED structures and chemical structures of various ligand materials with different bulkiness and length. Reproduced with permission from ref. 87. Copyright © 2019, American Chemical Society.

Figure 1.31. Schematic illustration of ligand exchange process driven by acid etching. Reproduced with permission from ref. 61. Copyright © 2021, Wiley-VCH.

Figure 1.32. (a)–(d) ζ potentials (left) and schematics (right) of QD surfaces. (a) The surface of as-synthesized perovskite QDs showing near-zero ζ potential. (b) Purified QDs with surface defects and exhibiting slight positive charges. (c) QD resurfacing with isopropylammonium bromide. Surface vacancies were passivated and a bipolar solvent shell formed around the surface of the QDs. (d) QD surface following cation substitution using Na^+. (e) Solids formed with resurfaced perovskite QDs with high PLQYs. (f) QD surface passivated with traditional long-chain organic ligands. (g) Film cast from perovskite QDs with long-chain organic ligands. Reproduced with permission from ref. 81. Copyright © 2020, Springer Nature.

Chapter 2.

Figure 2.1. Formation of the pNE film on graphene. (a) Molecular structure of norepinephrine. (b) Schematic of the process of coating and polymerization of norepinephrine on graphene. (c) Scheme for the polymerization pathway of norepinephrine. (d) Digital image of pristine and pNE-coated graphene on glass substrates.

Figure 2.2. AFM images of pNE-coated graphene samples incubated for 6 h with and without AEE.

Figure 2.3. Water contact angles on pNE-coated graphene samples incubated for 6 h with and without AEE.

Figure 2.4. Optical transmittance of pNE-coated graphene films before annealing.

Figure 2.5. Surface morphology analysis of pristine and pNE-coated graphene without annealing. (a) Topography images of pristine graphene and pNE-coated graphene formed with various incubation times. (b) RMS values representing the roughness of graphene and pNE-coated graphene. (c) Thickness of the pNE film as a function of the incubation time.

Figure 2.6. SEM images of (a–d) pNE-coated graphene and (e–h) pDA-coated graphene according to incubation time.

Figure 2.7. (a–c) AFM images of pNE-coated graphene after annealing with different incubation time. Comparison of (d) root mean square values and (e) thicknesses of pNE-coated graphene before and after annealing.

Chapter 3.

Chapter 4.

QDs (C-QD_{113}) with incubation time under ambient conditions (relative humidity: 65%, temperature: 25 °C). Emission stability of (b) ISNCs and (e) C-QD_{113} in toluene at 120 °C; the insets show photographs of the respective NCs acquired under UV light illumination. XRD patterns of (c) ISNCs and (f) C-QD_{113} after annealing in toluene at 120 °C over various periods of time.

Figure 4.7. Water contact angles of (a) ISNCs, (b) C-QD_{113}, and (c) separated $CsPbBr_3$ QDs (S-QD_{113}) on SiO_2 wafer.

Figure 4.8. (a) UV-vis absorption spectrum, (b) PL spectrum, and (c,d) TEM images of pure Cs_4PbBr_6 NCs (NC_{416}).

Figure 4.9. (a) UV-vis absorption spectra, (b) magnified view of the absorption spectra in the region 300-600 nm, and (c) Photoluminescence (PL) spectra of NCs washed with methyl acetate and the mixture of acetonitrile and toluene. TEM images of NCs washed with (d) the mixture of acetonitrile and toluene and (e) methyl acetate. (f) XRD patterns according to the washing method.

Figure 4.10. Characterization of the interaction between $CsPbBr_3$ QDs and Cs_4PbBr_6 NCs. (a) UV–vis absorption and (b) PL spectra for various ratios of separately prepared $CsPbBr_3$ QDs (S-QD_{113}) and Cs_4PbBr_6 NCs (NC_{416}). (c) NC size histograms before and after mixing S-QD_{113} and NC_{416} at a weight ratio of 1:2. (d) PL decay curves of S-QD_{113} and mixed S-QD_{113} and NC_{416}. (e) Photographs acquired under UV light illumination of the as-prepared sample (left) and the sample after storage for 12 h under ambient conditions (right). (f) PL spectra of film in part A and B of the sample slide after 0 h and 12 h. Part A of the film was coated with S-QD_{113} only and part B was sequentially coated with NC_{416} and then S-QD_{113}. (g) Schematics of S-QD_{113} surfaces produced by mixing S-QD_{113} and NC_{416} in weight ratios from 1:0 to 1:2. Imperfect octahedrons on the S-QD_{113} surface were peeled off upon addition of NC_{416}.

Figure 4.11. Photographs under (a) room light and (b) 365 nm UV light of the mixture according to the weight ratio of S-QD_{113} and NC_{416}.

Figure 4.12. (a) The schematic illustration of the experiment mixing S-QD_{113} and NC_{416} at a weight ratio is 1:2. TEM images of (b) S-QD_{113}, (c) NC_{416}, and (d) mixed S-QD_{113} and NC_{416}.

Figure 4.13. TEM images with different magnifications at (a) 13.5k, (b) 26.5k (c) 88k, and (d) 255k when S-QD_{113} and NC_{416} are mixed in a 1:2 weight ratio.

Figure 4.14. ^1H nuclear magnetic resonance spectra of (a) NC_{416}, (b) S-QD_{113}, (c) oleylamine, and (d) oleic acid dissolved in $CDCl_3$.

Figure 4.15. PL spectra of (a) S-QD_{113} and (b) ISNCs as a function of excitation wavelength. UV-vis absorption and PL excitation spectra of (c) S-QD_{113} and (d) ISNCs.

Figure 4.16. Temperature-dependent PL spectra of (a) S-QD_{113} and (b) ISNCs in the temperature range

of 20-300k. (c) Normalized PL intensities of S-QD_{113} and ISNCs as a function of temperature.

Figure 4.17. The schematic illustration of the mixing S-QD_{113} and NC_{416} in solid state.

Figure 4.18. Blue perovskite LED device structure and performance characteristics. (a) Cross-sectional SEM image of ISNCs LED. (b) Energy band diagram of the materials employed in LEDs. (c) Current density–voltage (*J–V*) curve and luminance–voltage (*L–V*) curve, (d) luminous efficiency–current density (LE–*J*) curve, and (e) EQE–current density (EQE–*J*) curve of ISNCs LEDs. (f) EL spectra of ISNCs LEDs at various voltages.

Figure 4.19. Histogram of maximum EQEs of ISNCs LEDs.

List of Tables

Chapter 2.

Chapter 3.

Chapter 4.

Abbreviation/Nomenclature

ACN	Acetonitrile
AEE	2-(2-aminoethoxy)ethanol
AFM	Atomic force microscopy
BA	*n*-butylammonium
C-QD$_{113}$	Conventional $CsPbBr_3$ QDs
CVD	Chemical vapor deposition
DAT	*n*-dodecylammmonium thiocyanate
DOBD	4-dihydroxybenzhydrazide
DOPA	3,4-dihydroxyphenylalanine
DSSC	Dye-sensitized solar cells
EL	Electroluminescence
EQE	External quantum efficiency
ETL	Electron transport layer
FA	Formamidinium
FF	Fill factor
FT-IR	Fourier transform-infrared spectroscopy
FWHM	Full widths at half maximum
HOMO	Highest occupied molecular orbital
HTL	Hole transport layer
ISNCs	*In situ* generated $CsPbBr_3$–Cs_4PbBr_6 NCs
ITO	Indium tin oxide
ITU	International telecommunication union
J_{sc}	Short-circuit current density
LCD	Liquid crystal display
LED	Light-emitting diode
Lys	Lysine
MA	Methylammonium
MHP	Metal halide perovskite
NC$_{416}$	Monodisperse Cs_4PbBr_6 NCs
NCs	Nanocrystals
NE	Norepinephrine
OA	Oleic acid

ODE	1-octadecene
OLAM	Oleylamine
OLAM-Br	Oleylammonium bromide
OSCs	Organic solar cells
$PC_{71}BM$	[6,6]-phenyl-C71-butyric acid methyl ester
PCE	Power conversion efficiency
pDA	Polymerized dopamine
PDA	Polydopamine
PEDOT:PSS	Poly(3,4-ethylenedioxythiophene):poly(styrenesulfonate)
PEM	Phenylethyl mercaptan
PGMEA	Propylene glycol monomethyl ether acetate
PLE	Photoluminescence excitation
PLQY	Photoluminescence quantum yield
PM6	Poly[(2,6-(4,8-*bis*(5-(2-ethylhexyl)-4-fluorothiophen-2-yl)benzo[1,2-b:4,5-b′]dithio-phene))-*co*-(1,3-di(5-thiophene-2-yl)-5,7-*bis*(2-ethylhexyl)-benzo[1,2-c:4,5-c′]dithiophene-4,8-dione))]
pNE	Polymerized norepinephrine
PTB7-Th	Poly[4,8-bis(5-(2-ethylhexyl)thiophen-2-yl)benzo[1,2-b;4,5-b′]-dithiophene-2,6-diyl-alt-(4-(2-ethylhexyl)-(3-fluorothieno[3,4-b]thiophene-)-2-carboxylate-2,6-diyl)]
PVK	Poly(9-vinylcarbazole)
QAB	Quaternary ammonium bromide
QD	Quantum dot
QDCF	Quantum dot color filter
QDEF	Quantum dot enhancement film
RMS	Root mean square
SEM	Scanning electron microscopy
TCE	Transparent conducting electrode
TEM	Transmission electron microscopy
TFB	Poly[(9,9-dioctylfluorenyl-2,7-diyl)-*co*-(4,4″-(*N*-(4-sec-butylphenyl)diphenylamine)]
THAM	Tris(hydroxymethyl) aminomethane
TMSP	Tri(methylsilyl)phosphine
TOP	Tri-*n*-octylphosphine
TPBi	2,2″,2″- (1,3,5-benzinetriyl)-tris(1-phenyl-1-*H*-benzimidazole)
TRPL	Time resolved photoluminescence

UPS	Ultraviolet photoelectron spectroscopy
V_{oc}	Open-circuit voltage
XPS	X-ray photoelectron spectroscopy
XRD	X-ray powder diffraction

Chapter 1.

Introduction of Thesis

1.1 Introduction to nanomaterials

The concept of nanotechnology was introduced in Richard P. Feynman's famous lecture "There's Plenty of Room at the Bottom" in 1959.[1] nanotechnology has advanced significantly and is still expanding into new fields such as physics, chemistry, material science, and biosciences. The term "nano" is derived from the Greek word nanos or the Latin word nanus, which means "dwarf." Nanotechnology is the study and application of nanomaterials, which have at least one dimension and a size range of 1 to 100 nanometers (Figure 1.1).[2]

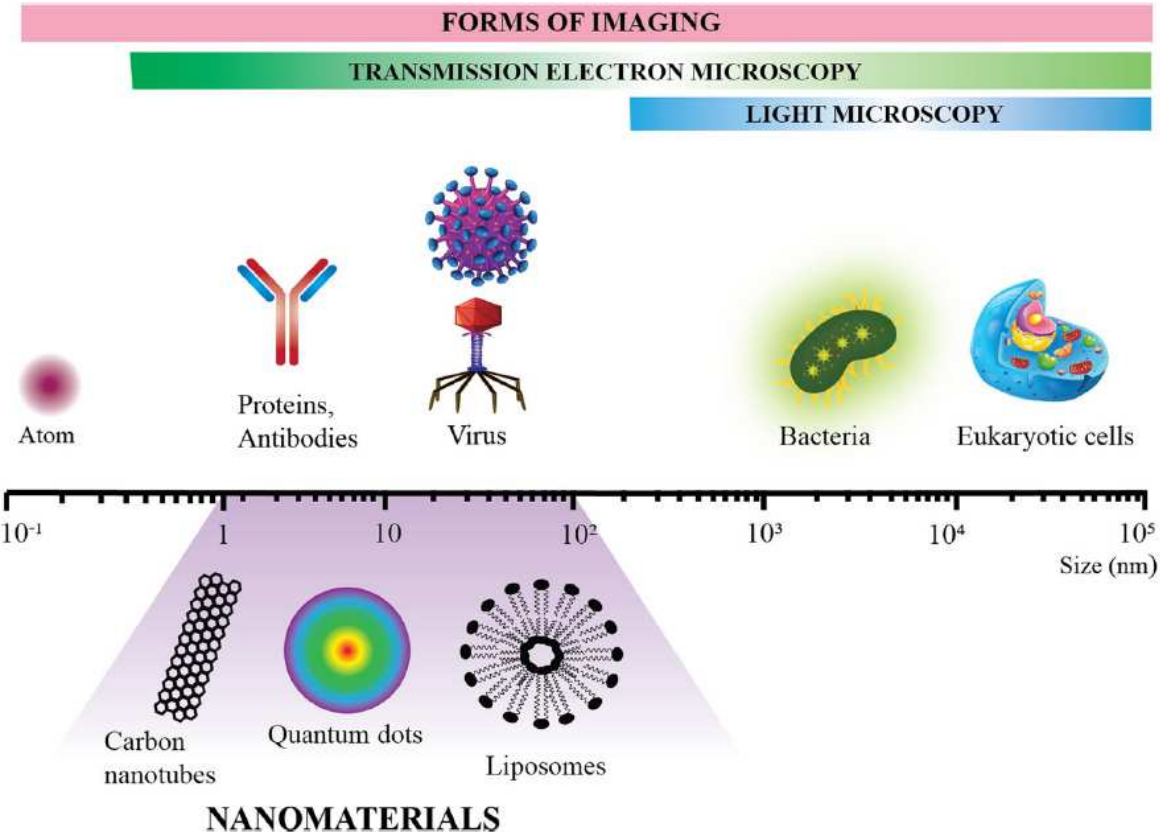

Figure 1.1. Relative size comparison of nanomaterials, microbiological, and other biological entities. Bodies visible by light and transmission electron microscopy are indicated and a scale bar denotes the size range of the respective biological entities and nanomaterials (1-100 nm). Reproduced with permission from ref. 2. Copyright © 2018, BioMed Central Ltd.

Nanomaterials are divided into different categories based on their dimensions and chemical properties. Typically, four different nanomaterials depend on their size and morphology (figure 1.2).[2] Zero-dimensional nanomaterials are materials in the nanoscale range in all three dimensions, and examples include semiconductor quantum dots, gold nanoparticles, and fullerenes. One-dimensional nanomaterials are materials in the nanoscale range of two dimensions, such as nanorods, nanowires, and carbon nanotubes. Two-dimensional nanomaterials are materials with any one dimension in the nanoscale range, examples of which are nanoplates, graphene, nanofilms, and layered nanomaterials. Finally, three-dimensional nanomaterials are out of the nanoscale range in any dimension, and examples include liposomes, polycrystalline materials, and dendrimers.

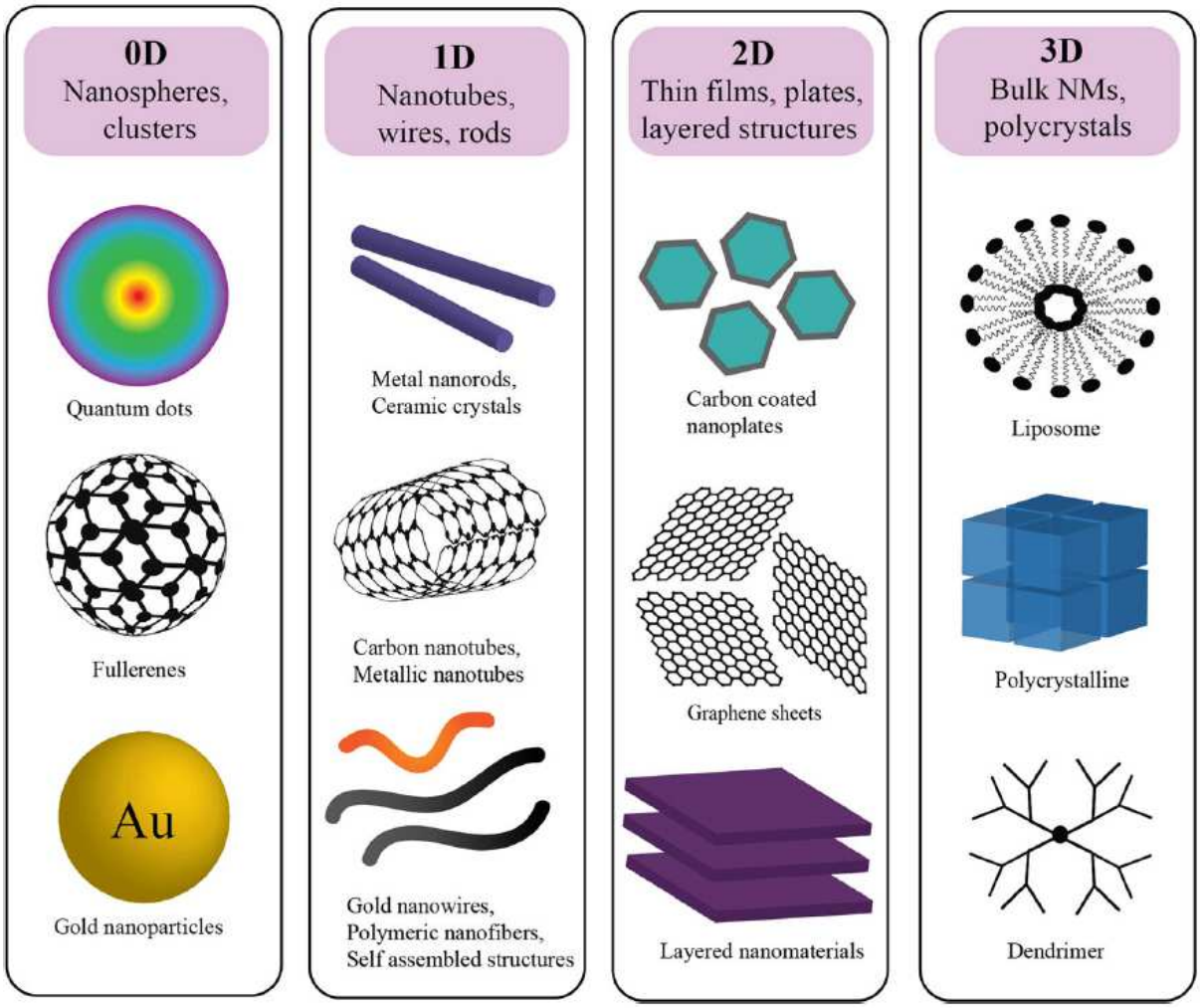

Figure 1.2. Schematic illustrating the relative dimensions of nanoparticles with examples of each category. Nanomaterials exist in different dimensionality and current classification schemes of nano-structured materials are proposed as zero (OD), one (1D), two (2D), and three-dimensional (3D). Reproduced with permission from ref. 2. Copyright © 2018, BioMed Central Ltd.

Based on their physical and chemical characteristics, nanomaterials can be classified as follows:

Carbon-based nanomaterials

Carbon-based nanomaterials include fullerenes, carbon nanotubes, graphene, graphene oxide, nanodiamonds, and carbon dots (Figure 1.3).[3] Fullerene, also known as the C_{60} molecule, was the first carbon nanostructure discovered and reported in 1985.[4] The C_{60} molecule has a spherical structure with the arrangement of its sp^2 carbon atoms in a succession of hexagons and pentagons. Moreover, six years later, carbon nanotubes were reported by Iijima.[5-7] The carbon nanotube is a tubular structure with a diameter of 1-2 nm, similar to the shape of a rolled graphite sheet. Then, single-layer graphene was isolated and characterized by A.K. Geim and K.S. Novoselov.[8] These carbon nanoallotropes show similar and unique properties because they consist of the sp^2 carbon atom, having a hexagonal network. They are all comparable in terms of optical properties, electrical conductivity, mechanical strength, and reactivities. Other types of carbon nanomaterials are carbon dots and nanodiamonds. Carbon dots contain combinations of sp^3 and sp^2 carbon atoms in various ratios, whereas nanodiamonds are composed of tetrahedral sp^3 carbon atoms.

Metal nanomaterials

Metal nanomaterials have unique characteristics, such as localized surface plasmon resonance and optical properties (Figure 1.4).[9] The coherent electron oscillations induced by the incident light lead to strong light absorption, scattering, and so forth at the surface of metal nanomaterials.[10, 11] As a result, the alkali and noble metal nanomaterials (e.g. Cu, Ag, and Au) have a strong and broad absorption band in the visible region. This localized surface plasmon resonance property can be easily modified by controlling the structure, shape, and size of metal nanomaterials (Figure 1.5).[12] For example, the color of the solution changes from blue to red when the size of Au nanoparticles is reduced to 3 nm. Due to their advanced optical properties, metal nanomaterials are widely used in different research areas, energy conversion, optoelectronic devices, and bioimaging.[13, 14]

Semiconductor nanomaterials

A semiconductor is a material that has a bandgap and an electrical conductivity between a conductor and an insulator. When a semiconductor absorbs photons with energy greater than the band gap, electrons are excited from the valence band to the conduction band, leaving holes and generating excitons. An exciton means that an electron and hole are bound by Coulomb interaction.

Semiconducting nanomaterials have a specific length scale called exciton Bohr radius ranging from 2 to 50 nm. When the size of the semiconductor is smaller than the exciton Bohr radius, spatial confinement occurs in the exciton wave function.[15] This difference in the density of the electronic state induces a change in the bandgap depending on the size of the semiconductor (Figure 1.6).[16] The effect

is referred to as quantum confinement and is applied to various optoelectronic devices such as solar cells, photodetectors, and light-emitting diodes. Semiconductor nanomaterials are formed from a variety of different compounds. Typical examples include Si, Ge of group IV, GaN, GaP, GaAs, InP, and InAs of group III-V, and ZnO, ZnS, CdS, CdSe, and CdTe of group II-VI.[17]

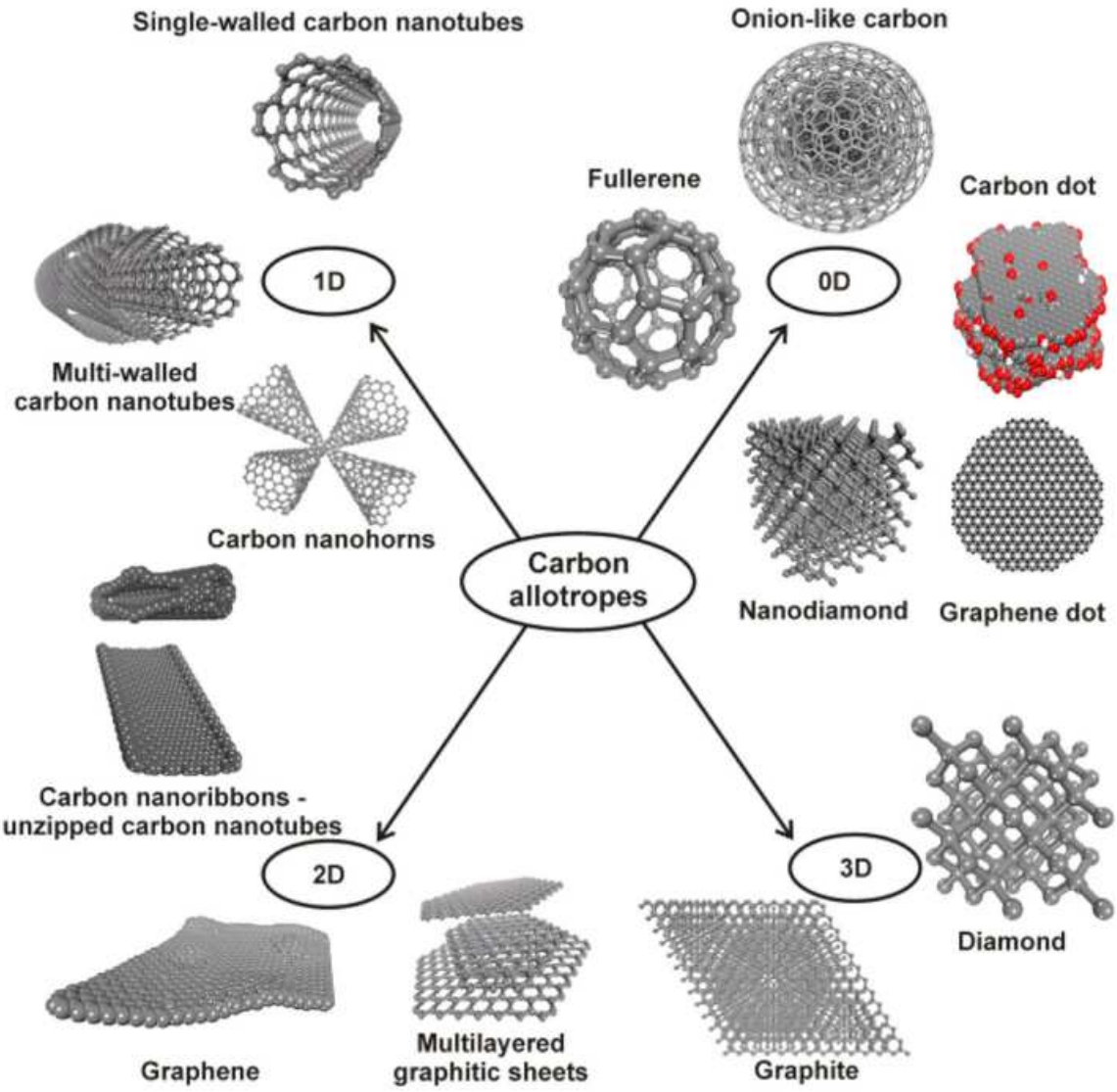

Figure 1.3. The classification of carbon-based nanomaterials based on their dimension. Reproduced with permission from ref. 3. Copyright © 2015, American Chemical Society.

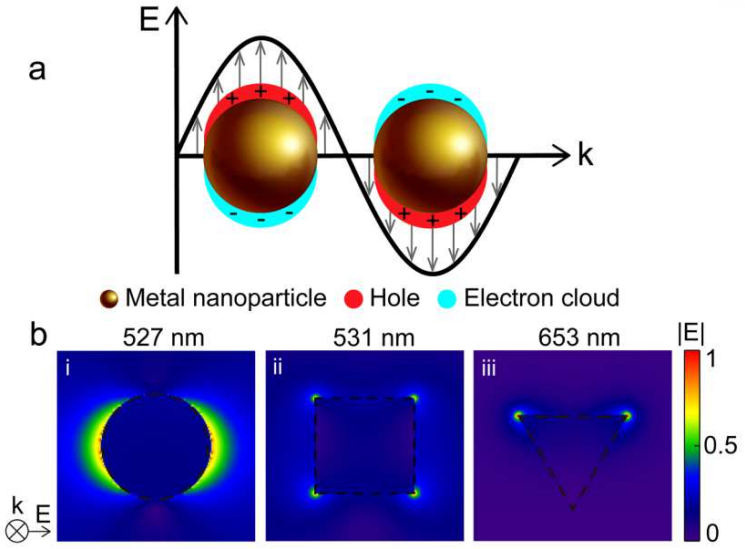

Figure 1.4. Localized surface plasmon resonance on plasmonic nanoparticles. (a) Scheme of the electron clouds oscillating opposite from the direction of electric field close around the NPs with a size much smaller than the incident wavelength. (b) Finite difference time domain calculation of the on-resonance (wavelength labeled on the top of each figure) normalized electric field (|E|) distribution of (i) a nanosphere, (ii) a nanocube, and (iii) a nanotriangle, demonstrating the highly localized enhancement especially at the sharp tips and rapid attenuation with the distance. Reproduced with permission from ref. 9. Copyright © 2021, American Institute of Physics.

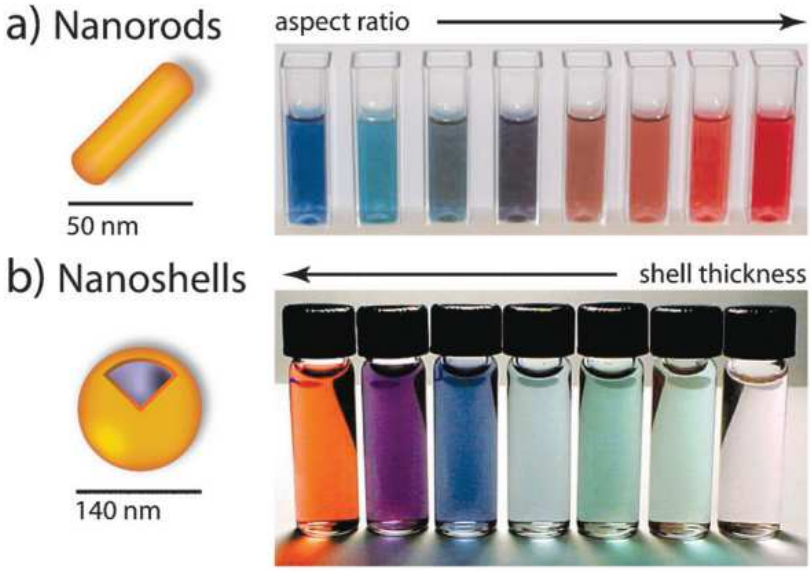

Figure 1.5. (a) Gold nanorods, and (b) silica–gold core–shell nanoparticles. The intense color of these nanoparticles arises from the collective excitation of their conduction electrons, or surface plasmon resonance modes, which results in photon absorption at wavelengths which varies with (a) aspect ratio and (b) shell thickness. Reproduced with permission from ref. 12. Copyright © 2012, Royal Society of Chemistry.

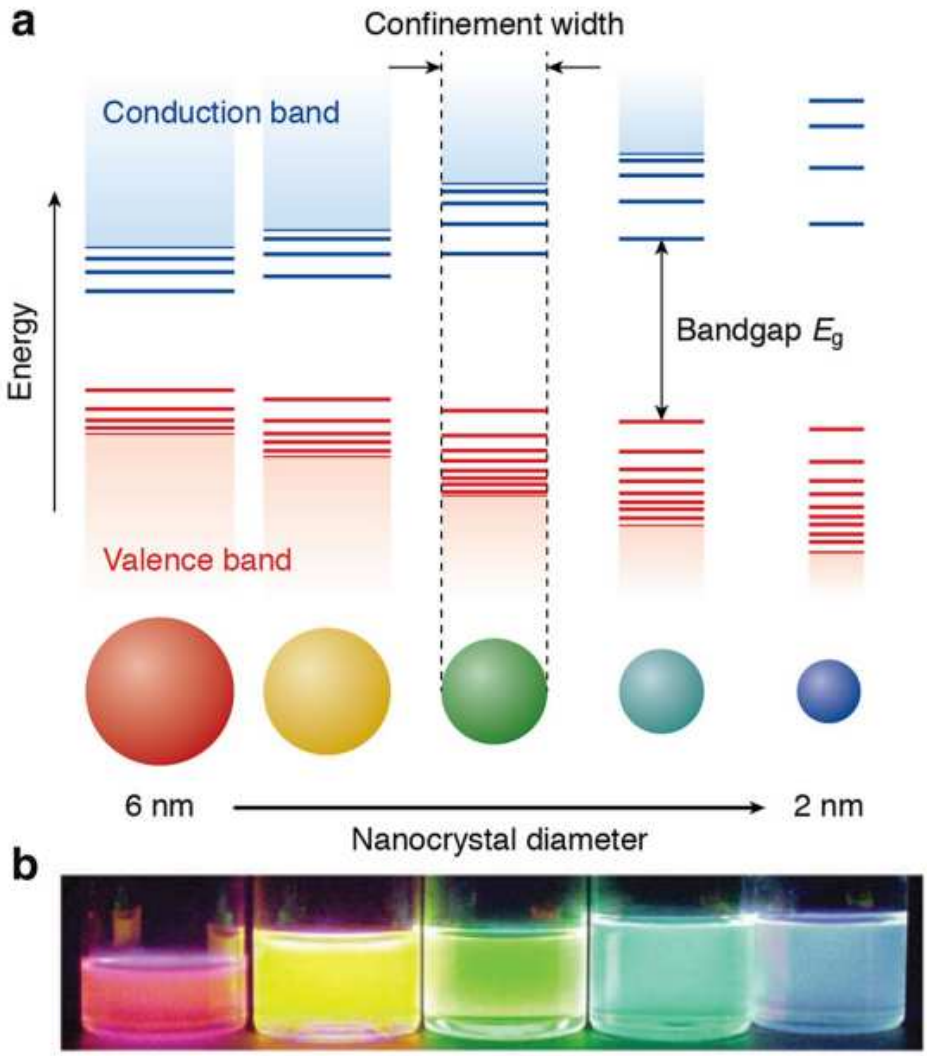

Figure 1.6. (a) Schematic representation of the quantum confinement effects: the bandgap (or HOMO–LUMO gap) of the semiconductor nanocrystal increases with decreasing size, while discrete energy levels arise at the band edges. The energy separation between the band-edge levels also increases with decreasing size. (b) Photograph of colloidal dispersions of CdSe QDs with different sizes under excitation with a UV lamp in the dark. The color of the photoluminescence changes from red to blue as the QD diameter is reduced from 6 to 2 nm. Reproduced with permission from ref. 16. Copyright © 2012, Royal Society of Chemistry.

Polymeric nanomaterials

Polymer nanomaterials are colloidal organic nanoparticles with dimensions in the nano regime. Depending on the synthetic method, they are mainly divided into nanosphere and nanocapsule structures.[18] The nanosphere is a matrix-like structure in which a polymer has a single large sphere morphology, and other molecules are adsorbed on the sphere surface. On the other hand, the nanocapsule has a core-shell structure, and the polymeric shell encapsulates external substances.[19-21] Polymeric nanomaterials are widely used for drug delivery and diagnostics purposes because they have the advantages of protection and controlled release of specific substances such as drugs, easy functionalization, and biocompatibility. (Figure 1.7).[22]

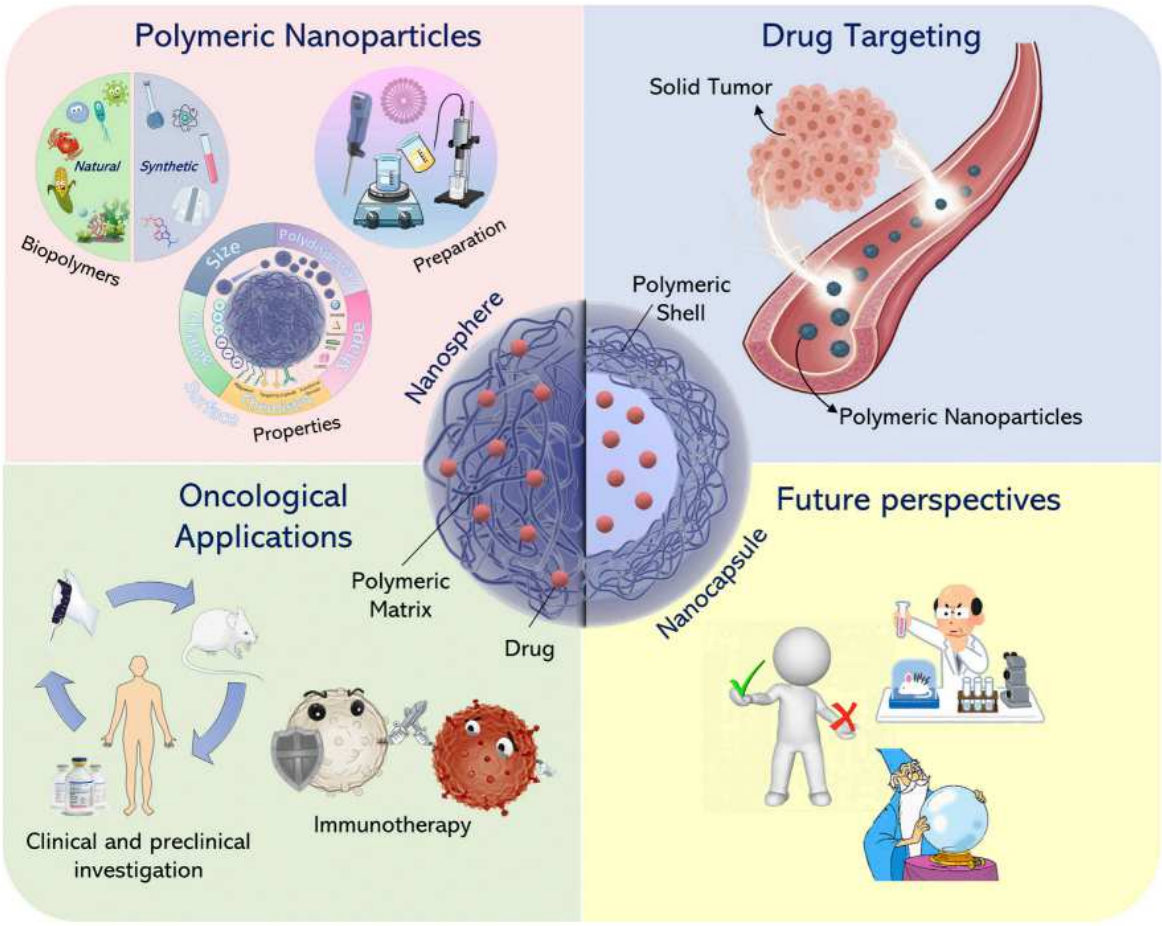

Figure 1.7. Overview of the main features of polymeric nanoparticles. Reproduced with permission from ref. 22. Copyright © 2012, Frontiers Media SA.

Physicochemical properties of nanomaterials

The nanomaterials have a high surface-area-to-volume ratio compared to the bulk, exhibiting new magnetic, electrical, optical, mechanical, and catalytic properties that are not expressed in their bulk counterparts. (Figure 1.8).[23] The following section discusses some of their key characteristics.

Electronic and optical properties

Some nanomaterials display a distinct color from their bulk counterparts. These phenomena appear due to the confinement of electrical carriers within nanomaterials. The electromagnetic field of the incident light on the metal nanoparticle induces coherence oscillation with free electrons of the metal. Electron oscillation causes charge separation at the metal surface and generates dipole oscillation. This localized surface plasmon resonance strongly absorbs the incident light and changes the optical properties of the material.[24] Semiconductor nanoparticles are in the spotlight as optical materials because they have an appropriate bandgap and its tunability. Semiconductor nanomaterials adjust the bandgap of the material as desired within a size smaller than the exciton Bohr radius by the quantum confinement effect.[25]

Magnetic properties

The magnetic dipoles known as magnetons are created by spinning electric-charged nanomaterials. Magnetons in ferromagnetic materials are reorganized into Weiss domains. This magnetic domain is a volume in which magnetons are aligned in the same direction by an external magnetic field. The response of a ferromagnetic material to an applied magnetic field is interpreted as a hysteresis loop. Remanence and coercivity are the two main parameters in a hysteresis loop, and coercivity is strongly correlated with the size of materials. As the size of the ferromagnetic material gradually decreases, the multi-domain becomes a single domain and then the coercivity reaches zero (Figure 1.9).[26, 27] This is called superparamagnetism, and superparamagnetic nanomaterials become nanomagnets that respond only to external magnetic fields without hysteresis.

Thermal properties

In general, as the number of grain boundaries increases, phonon scattering increases at the disordered boundary, resulting in a decrease in thermal conductivity. However, when the grain size is reduced to the nano regime, it becomes comparable to the phonon's mean free path. The nanomaterials differ from the general trend due to the photon confinement and quantization effect of photon transport. The shape of nanomaterials, in particular, has an impact on their thermal conductivity. For instance, strong phonon-phonon interactions cause 1D nanowires to have reduced thermal conductivity, whereas tubular architectures have excellent thermal conductivity. Additionally, the melting point of the substance tends to decrease in nanomaterials. (Figure 1.10).[28] This is because nanoparticles have a high surface area-to-volume ratio that modifies the thermodynamic and thermal properties of the material.

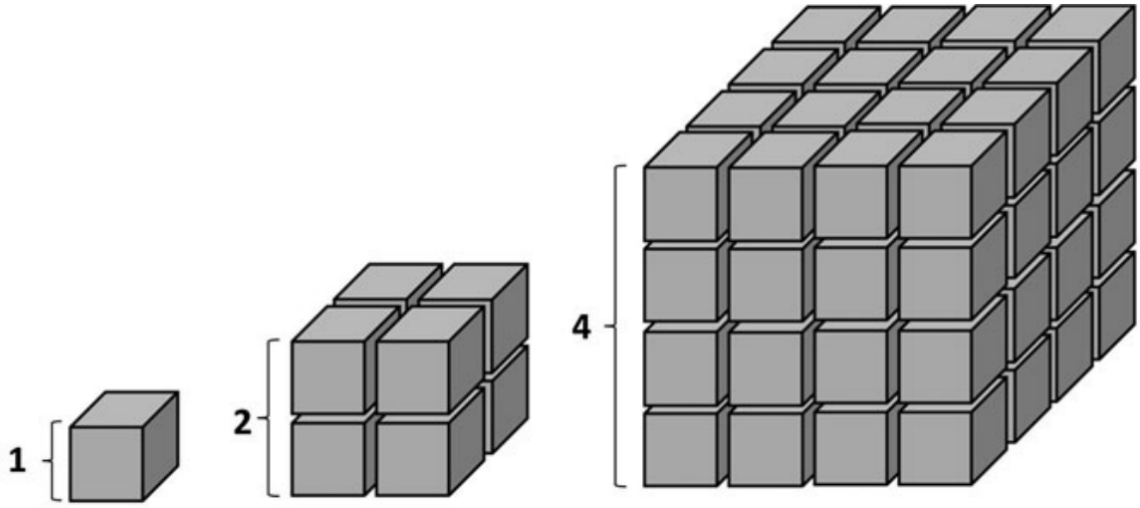

Side of Cube	Area of side	Area of cube surface	Volume	Ration of surface area to volume
1 cm	1 cm^2	6 * 1 cm^2	1 cm^3	6/1
2 cm	4 cm^2	6 * 4 cm^2	8 cm^3	24/8 =3/1
4 cm	16 cm^2	6 * 16 cm^2	64 cm^3	96/64 = 3/2

Figure 1.8. Changes in the surface area to volume ratio of a cube. The smaller the cube (object), the higher surface area to volume ratio, which has a key role in the interaction of a nanoscale material with its surrounding environment. Reproduced with permission from ref. 23. Copyright © 2019, Springer Nature.

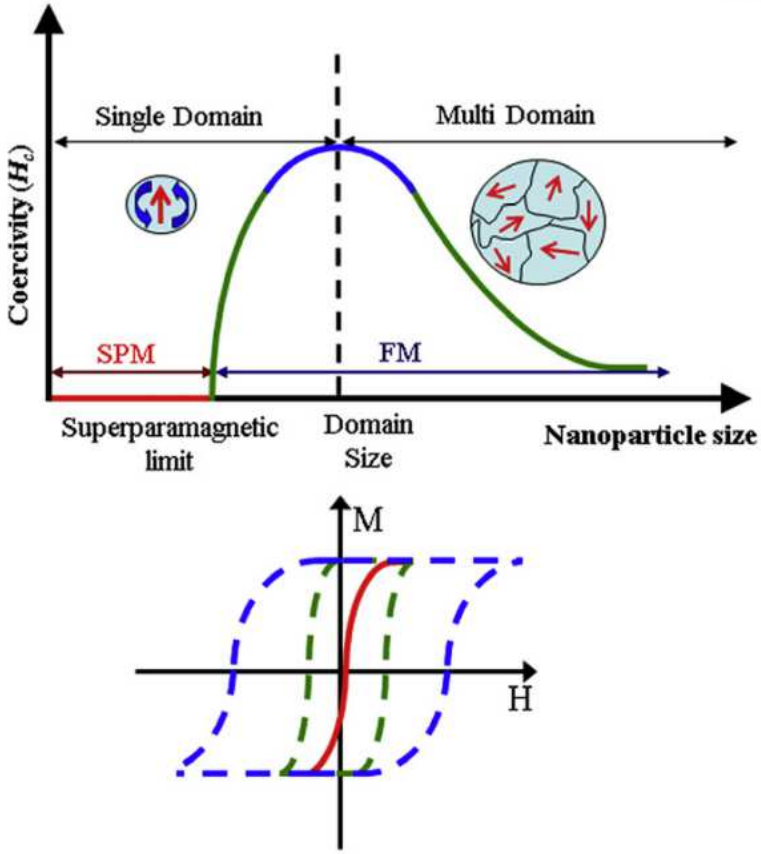

Figure 1.9. The qualitative behavior of the size-dependent coercivity of magnetic particles. The magnetic behavior of superparamagnetic nanoparticles is demonstrated by the solid line, while ferromagnetic particles are presented by dashed lines. Here H denotes the applied magnetic field strength and M is the measured magnetization. Reproduced with permission from ref. 26. Copyright © 2011, IOP Publishing Ltd.

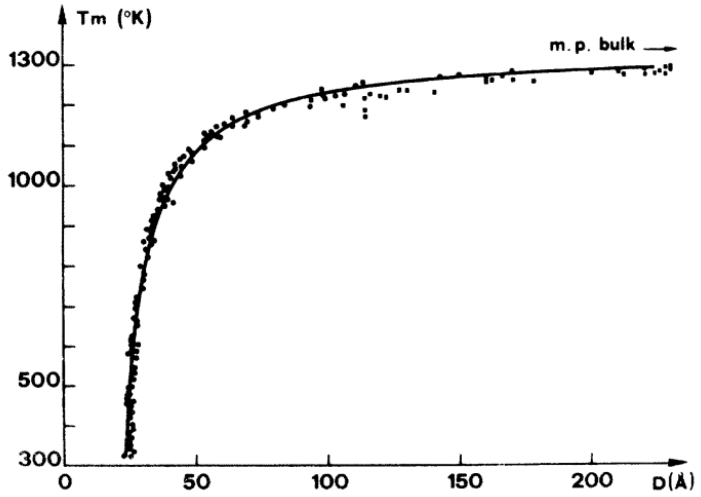

Figure 1.10. Experimental and theoretical values of the melting-point temperature of gold particles. Reproduced with permission from ref. 28. Copyright © 1976, American Physical Society.

1.2 Interface/surface engineering strategies for nanomaterials

Encapsulation with amphiphilic species

Surface engineering is essential to apply the outstanding and unique characteristics of nanomaterials to various research fields. Highly crystalline and monodisperse nanocrystals are often synthesized by high temperatures in organic solvents and have hydrophobic long-chain ligands. The encapsulation method forms an additional ligand layer on the original ligand layer based on the hydrophobic interaction. Hydrophobic parts are intercalated between the original ligands in amphiphilic species (e.g., polymers, proteins, and lipids), while the hydrophilic parts are exposed to the outside to change solubility. [29-32] This method has the advantage of reducing defects on the surface of nanoparticles and enhancing stability because the original ligand is preserved without detaching. Furthermore, functional groups can be added to hydrophilic parts to introduce conjugation points and make the organic complex shell robust via crosslinking. W. J. Parak's group improved the stability of the encapsulated nanocrystal by locating an anhydride ring on the surface and using amino end groups as the cross-linker molecule (Figure 1.11).[33] However, as a second ligand layer is formed on the surface, the hydrodynamic diameter increases and the encapsulation is easily collapsed in organic solvents.

Encapsulation with silica

Silica encapsulation is also a promising surface engineering method due to its excellent stability, nontoxicity, and biocompatibility. There are two methods for encapsulating silica on nanomaterials: the Stöber approach and the water-in-oil reverse microemulsion approach (Figure 1.12).[34, 35] The Stöber approach uses nanomaterials as seeds for silica growth and requires making the surface of nanomaterials hydrophilic and replacing them with silane groups.[36-38] In this process, 3-mercaptopropyl-trimethoxysilane and 3-aminopropyl-trimethoxysilane are frequently used. This approach has the disadvantage of the low uniformity of the encapsulated nanoparticles. In the second method, the water-in-oil reverse microemulsion method, small water droplets are stabilized by a nonionic surfactant in the hydrophobic solvent.[39, 40] The silica precursor undergoes hydrolysis and condensation at the water/oil interface, which allows for uniform and controllable silica shelling. This method is widely used because the encapsulation method is simpler than the Stöber approach, and it is easy to control the silica morphology. The simplicity of functionalization is another advantage of silica coating. Functional groups are introduced through numerous silane coupling agents with a series of processes including, hydrolysis, condensation, hydrogen bonding, and bond formation.

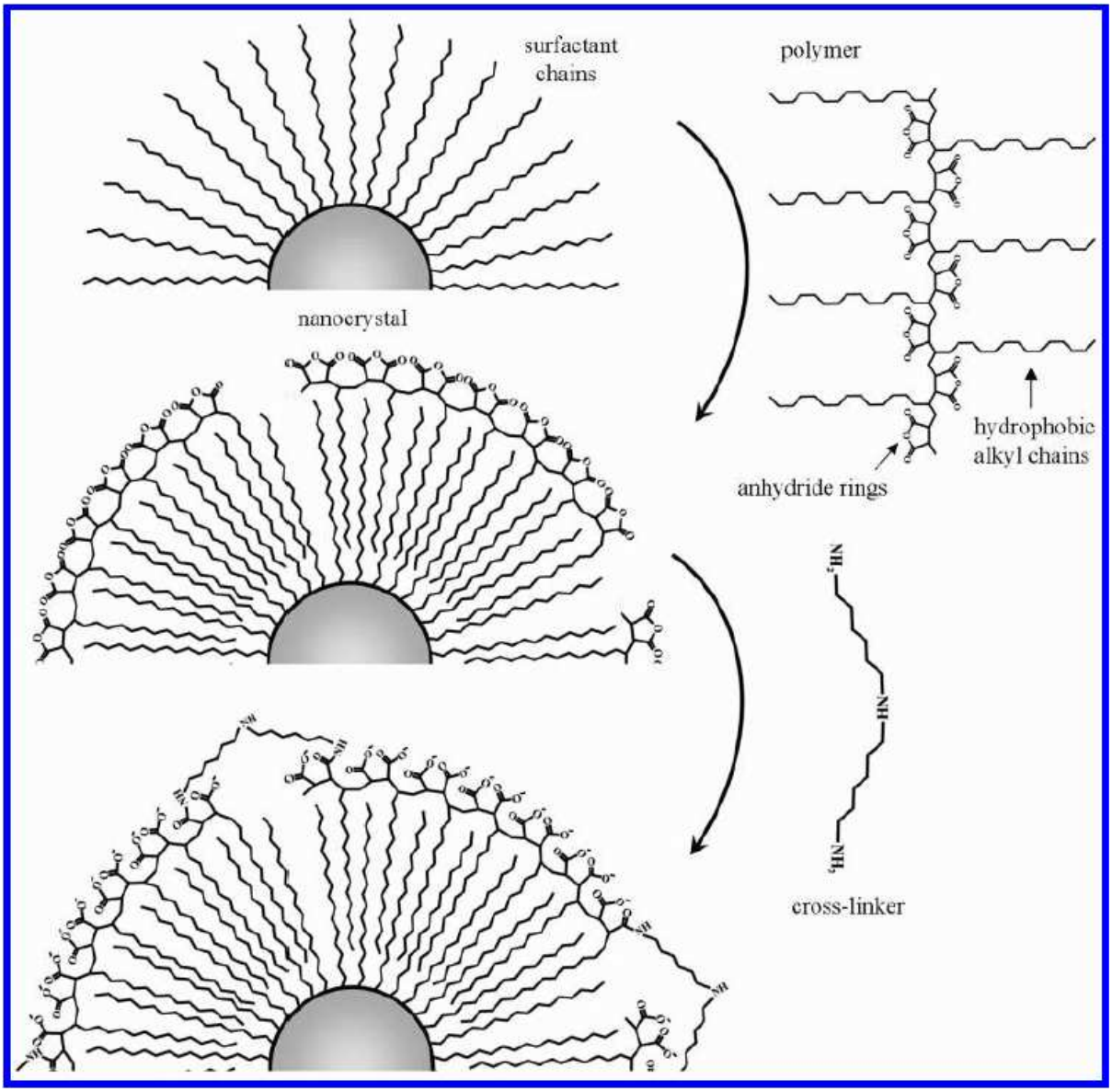

Figure 1.11. Amphiphilic Polymer encapsulation of the nanocrystals. The hydrophobic alkyl chains of the polymer intercalate with the surfactant coating. The anhydride rings are located on the surface of the polymer-coated nanocrystal. The amino end groups of the cross-linker molecule open the rings and link the individual polymer chains. The surface of the polymer shell becomes negatively charged, stabilizing the particles in water by electrostatic repulsion. Reproduced with permission from ref. 33. Copyright © 2004, American Chemical Society.

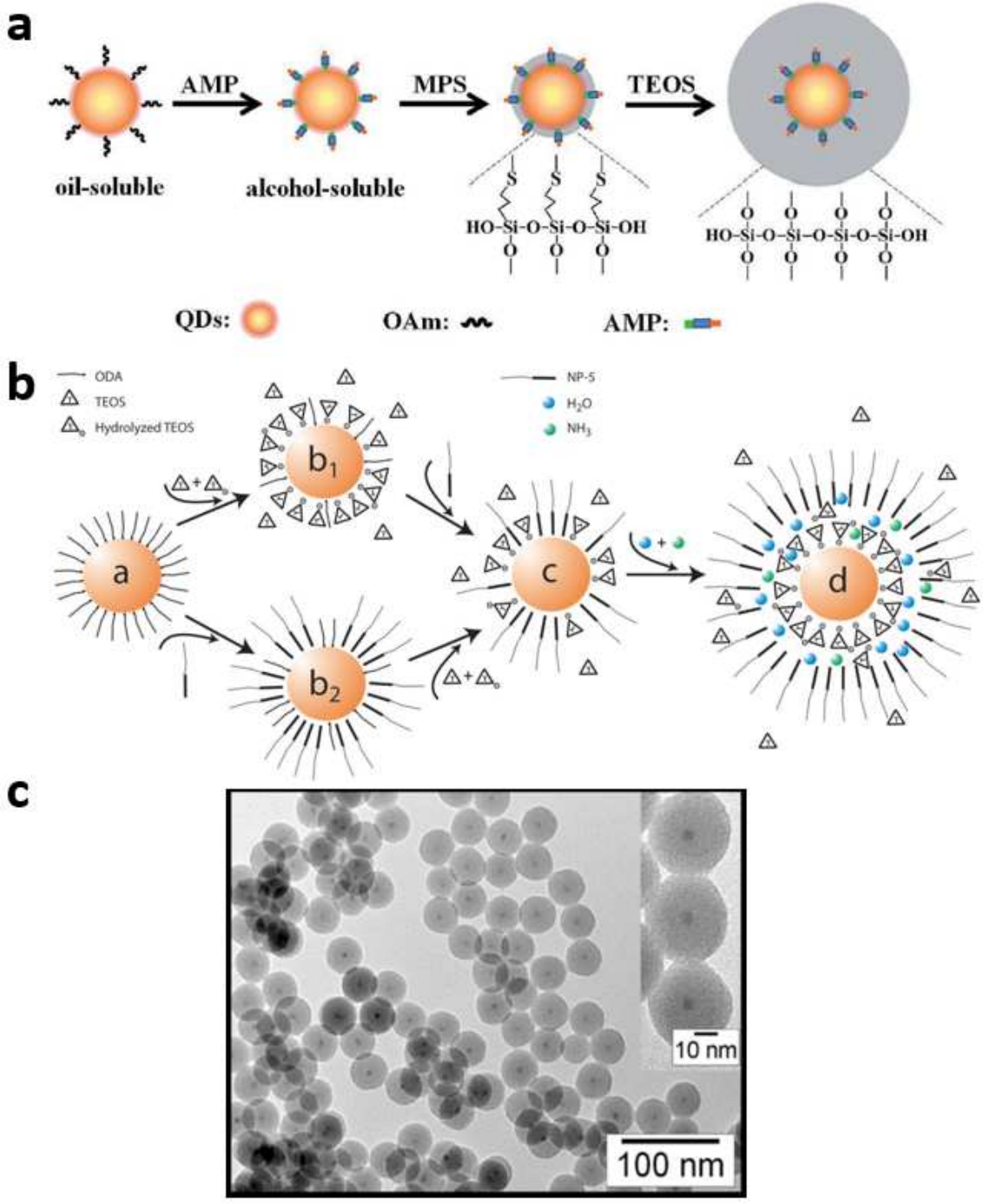

Figure 1.12. (a) Schematic illustration for the synthesis of quantum dots@SiO_2 using Stöber approach. Reproduced with permission from ref. 34. Copyright © 2014, The Royal Society of Chemistry. (b) Schematic representation of the incorporation mechanism of hydrophobic quantum dots in silica spheres by the reverse microemulsion method. (c) TEM images of quantum dots (6.4 ± 0.8 nm) in silica spheres of 37.2 ± 1.5 nm in diameter; inset shows a magnification of the same sample. Reproduced with permission from ref. 35. Copyright © 2008, American Chemical Society.

Ligand exchange with small molecules

The reactive dangling bonds are exposed on the surface of nanomaterials and are passivated by ligands. Ligands play important roles, such as improving the colloidal stability of nanomaterials and electronic communication between nanomaterials. Ligand exchange refers to detaching existing ligands and replacing them with newly designed ligands. In order to resolve the surface dangling bonds and charge-trapping centers produced during this process, it is crucial to understand how the ligand binds to the surface of nanomaterials. Ligands are classified into three types depending on the metal-ligand interaction: X-type, L-type, and Z-type ligands (Figure 1.13).[41-43] X-type ligands interact with a singly occupied orbital on a surface site as a one electron donor and typically include carboxylate, thiolates, inorganic ions, and halides. L-type ligands are two electron donors that interact with unoccupied surface metal orbitals and typically include amines, phosphines, and phosphine oxides. Z-type ligands are two electron acceptors interacting with an occupied lone pair on a surface anion site and typically have metal halides. A binding affinity stronger than the original ligands is required for ligand exchange with small molecules, and ligands should be carefully chosen based on the material's surface. In addition to organic-based ligands, Talapin and co-workers developed molecular metal chalcogenide complexes, so-called MCCs in 2009 (Figure 1.14).[44] These ligands enhance the electronic coupling between neighboring nanocrystals by removing the organic ligand and implementing an inorganic solid.

Ligand exchange with polymeric ligand

The direct ligand exchange method is more accessible to achieve compact nanocrystals than the encapsulation method, but it has the drawback of being unstable in the external environment. Multidentate polymer ligands with more binding sites than monodentate ligands have been developed to increase the stability of nanomaterials.[45] These polymeric ligands effectively passivate the nanoparticles and minimize the defects caused by the desorption of the binding group. The ability to easily control the ratio and amount of anchoring, stabilizing, tethering, and functional groups is another benefit of polymeric ligands (Figure 1.15).[46] Thiol, catechol, carboxylic acid, and imidazole groups are utilized as anchoring groups, accounting for 10 to 30% of the total ratio. Zwitterion and poly(ethylene glycol) are frequently employed as stabilizers for bio applications. The versatility for nanomaterials is considerably increased by the additional conjugation points provided by tethering groups and functional groups.

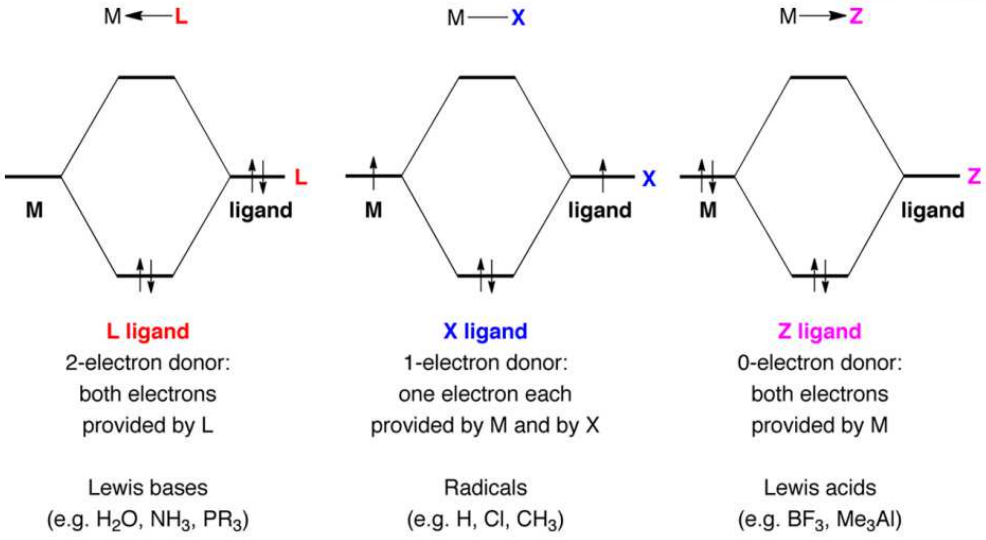

Figure 1.13. The covalent bond classification of L, X, and Z ligands. Note that the ligands are always classified in their neutral forms. L-type ligands (2-electron donors) are identified as Lewis bases, X-type ligands (1-electron donors) as radicals, and Z-type ligands (0-electron donors) as Lewis acids. Reproduced with permission from ref. 43. Copyright © 2014, American Chemical Society.

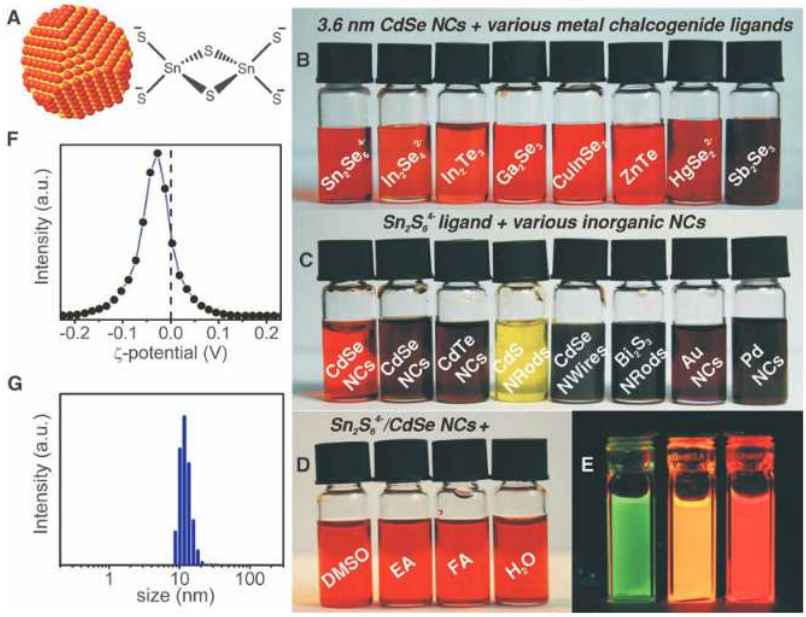

Figure 1.14. (a) Sketch of a CdSe NC capped with $Sn_2S_6^{4-}$ ions. (b) Stable colloidal solutions of 3.6 nm CdSe NCs capped with various metal chalcogenide complexes in hydrazine. (c) Stable colloidal solutions obtained by combining $(N_2H_5)_4Sn_2S_6$ (d) CdSe-$Sn_2S_6^{4-}$ nanoparticles dispersed in various solvents. (e) Photograph of photoluminescence excited by an ultra-violet lamp. (f) z-Potential measured for $Sn_2S_6^{4-}$ capped CdSe NCs in hydrazine. (g) Size histogram obtained from dynamic light scattering for 8 nm CdSe-$Sn_2S_6^{4-}$ nanocrystals in hydrazine. Reproduced with permission from ref. 44. Copyright © 2009, American Association for the Advancement of Science.

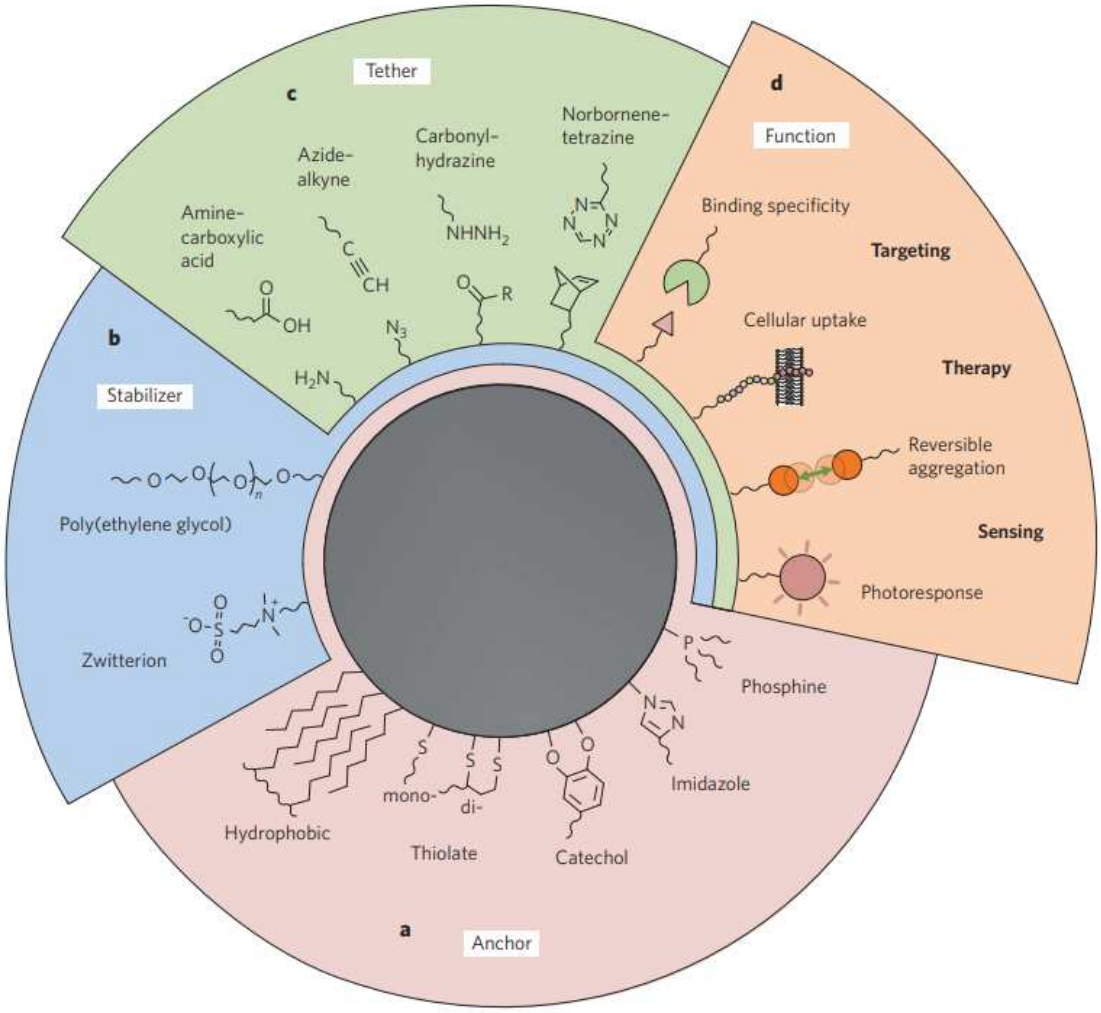

Figure 1.15. Modular design of surface ligands for biocompatible nanomaterials. (a) Anchor links capping molecules to the crystallite through hydrophobic interaction with native ligands or through atoms that bind directly to the nanocrystal surface. (b) Stabilizer region incorporates polyethylene glycol or zwitterionic chains that strongly bind water molecules to impart hydrophilicity and prevent nonspecific adsorption. (c) Capping molecules may feature reactive groups serving as a tether point for covalent conjugation to biofunctional molecules after ligand exchange. (d) The biofunctional units can offer targeting, therapeutic or sensing capability. Reproduced with permission from ref. 46. Copyright © 2016, Springer Nature.

Mussel-inspired universal coating

Mussels are marine organisms that stick strongly to both inorganic and organic surfaces, even in the harsh environment of waves. In order to mimic the adhesion of mussels, a sticky plaque is examined, and it is discovered that mussel foot proteins 3 and 5 are present on the surface (Figure 1.16a).[47] These proteins are particularly rich in lysine (Lys, K) and 3,4-dihydroxyphenylalanine (DOPA, Y) (Figure 1.16b).[48] Based on these findings, H. Lee and co-workers reported universal polydopamine coating with a substance called dopamine, where the catechol of DOPA and amine of Lysine exists in a single molecule (Figure 1.16c).[49] The oxidative polymerization of catecholamine is able to coat various substrates via adhesion and cohesion. Afterward, similar 1) polyphenol coating found in tea leaves, wine, and chocolate, 2) coordination complexes of polyphenols and Fe^{3+} ions, and 3) 5-pyrogallol 2-aminoethane coating methods were developed.[50-52] Coating methods based on catechol and polyphenol are expected to be applied in various fields because they have the advantages of being facile, universal, versatile, thin, biocompatible, eco-friendly, and inexpensive.

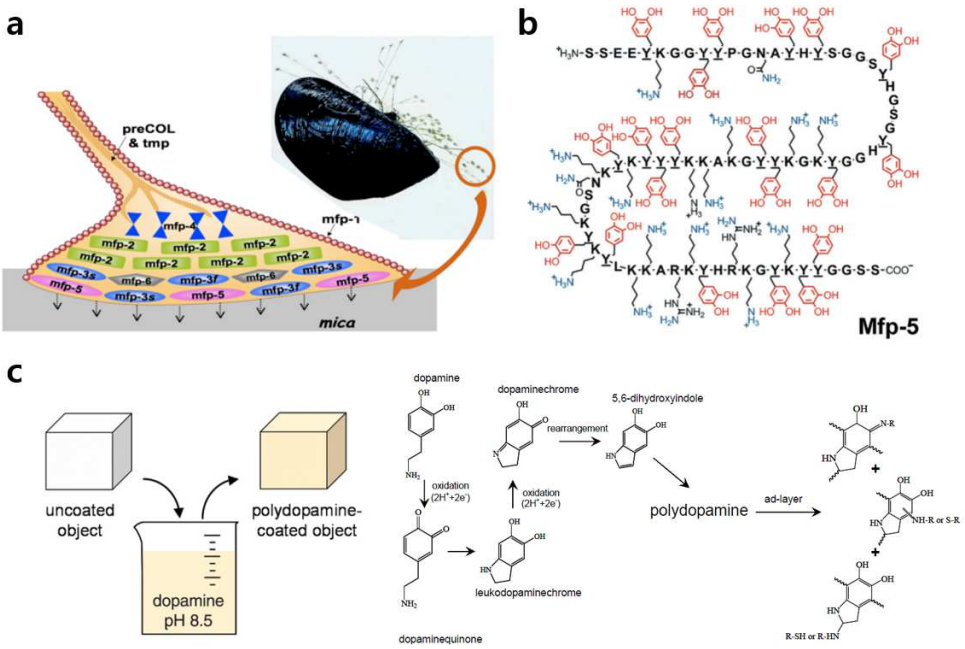

Figure 1.16. (a) A mussel is shown attached to a sheet of mica. One of its plaques (red circle) is enlarged as a schematic drawing to illustrate the approximate distribution of known proteins. Reproduced with permission from ref. 47. Copyright © 2010, The American Society for Biochemistry and Molecular Biology, Inc. (b) Structural formula of the mussel foot proteins, mfp-5 showing the alternating amino acids that contain amine (blue) and catechol (red) units in their side chains. Reproduced with permission from ref. 48. Copyright © 2014, Wiley-VCH. (c) A schematic illustration of thin film deposition of polydopamine by dip-coating an object in an alkaline dopamine solution. Possible structural evolution and polymerization mechanisms of dopamine. Reproduced with permission from ref. 49. Copyright © 2007, American Association for the Advancement of Science.

1.3 Interface/surface engineering for optoelectronic devices

Optoelectronic devices

Optoelectronic devices are components that detect, emit, convert, and exploit electromagnetic radiation based on light-matter interaction. These are essential to our lives, along with today's technological developments, typically including photovoltaics, light-emitting diodes (LEDs), photodetectors, lasers, and so on (Figure 1. 17).[53] Photovoltaics convert light energy into electricity via the photoelectric effect. LEDs are devices that convert electric current into light emission, and materials that emit light in the visible range are primarily used. Communication between materials at interfaces is crucial because optoelectronic devices are made up of multilayer structures, as shown in Figure 1.18. [54] Interface/surface engineering allows for the regulation of physical stress, energy barrier, interfacial band alignment, and defect, all of which are directly related to the performance of devices. Furthermore, the impact of the interface is prominent because nanomaterials have a high surface-area-to-volume ratio and numerous surface defects.

Figure 1.17. Types of optoelectronic devices. Reproduced with permission from ref. 53. Copyright © 2020, Frontiers Media S.A.

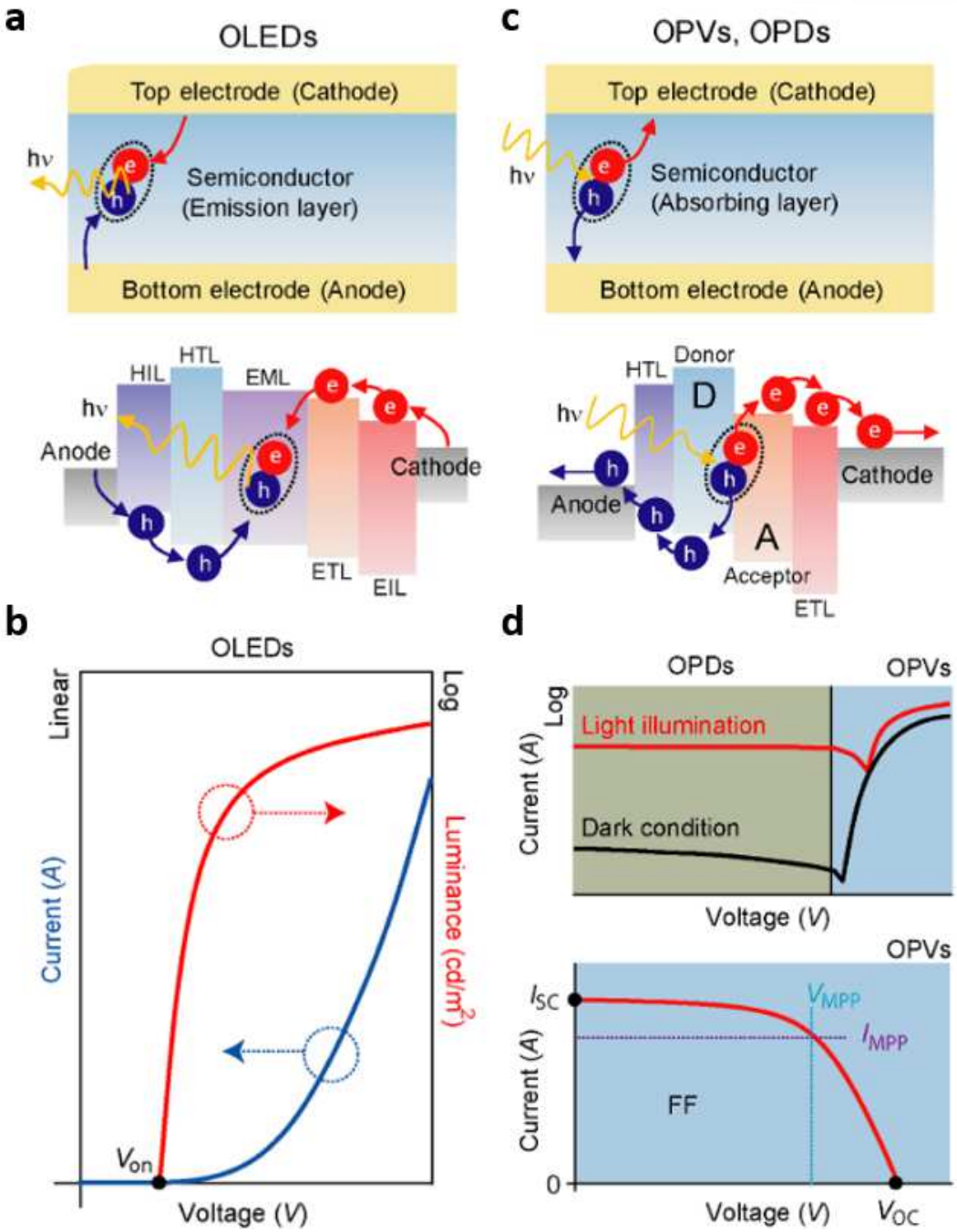

Figure 1.18. (a) Schematic depicting the device structure of an organic light-emitting diode (OLED) and band diagram of the OLED. (b) Typical current–voltage characteristics of an OLED. (c) Schematic depicting the device structure of an organic photodiode (OPD) and photovoltaic (OPV), and diagrams of the OPD and OPV. (d) Typical current–voltage characteristics of an OPD (top) and OPV (bottom). Reproduced with permission from ref. 54. Copyright © 2021, Elsevier B.V.

Role of interface/surface engineering: Energy level alignment

The arrangement of energy levels in each layer is crucial for fabricating highly efficient optoelectronic devices because it affects the transport of electrons and holes. In order to guarantee the high efficiency and stability of the devices, it is required to lower the barrier to charge transport and balance electron and hole transport. The energy level of the materials modulates when the dipole moment on the surface is controlled by ligand exchange. (Figure 1.19).[55-57]

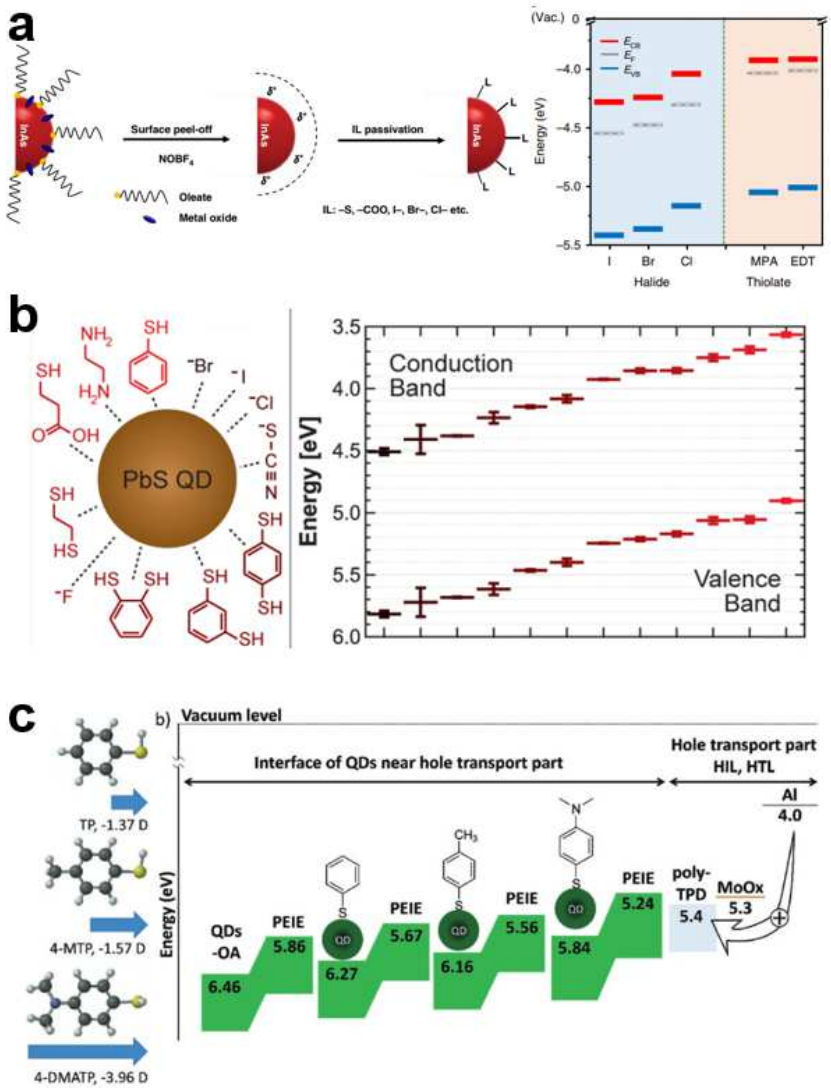

Figure 1.19. (a) Scheme of the two-step surface modification of InAs QDs and Energy levels ECB, EVB, and EF (vs. the vacuum level) of InAs QD films, deduced from UPS measurements. (ref. 57) (b) Complete energy level diagrams of PbS QDs exchanged with the various ligands. Reproduced with permission from ref. 56. Copyright © 2014, American Chemical Society. (c) Dipole moments of TP, 4-MTP, and 4-DMATP molecules, and energy level diagram of interface between QDs and hole transport part based on measured VBM of QDs in all-solution-processed inverted-structure green QLEDs. Reproduced with permission from ref. 55. Copyright © 2020, Wiley-VCH.

P. R. Brown *et al*. shifted the energy level of PbS quantum dots (QDs) by up to 0.9 eV without changing the size of core QDs by exchanging various thiol-based and halide ligands.[56] The change of the dipole moment of the QDs-ligand surface shifted the vacuum energy level and changed the position of the valence band maximum and conduction band minimum. As a result, they achieved an optimized PbS QDs solar cell efficiency of 8.55%.

H. Moon *et al*. performed ligand exchange with three thiol ligands with different dipole moments on CdSe@ZnS QDs.[55] Only the valence band maximum was upshifted during this process; the bandgap and photoluminescence barely changed. As electron and hole transfer accelerated and charge balance was matched, QLEDs performance of maximum luminance of 106400 cd/m^2 and external quantum efficiency of 24.8% was achieved.

Role of interface/surface engineering: Defect passivation

Defects on the interface/surface of the materials generate trap states to induce charge accumulation as a charge injection barrier or act as nonradiative recombination centers. Defect passivation thus contributes significantly to improving the performance of optoelectronic devices. For instance, the efficiency can be increased by passivating the defects of metal oxides such as SnO_2, TiO_2, ZnO, and NiO employed as the charge transport layer in the device. S-.Y. Yoon *et al*. suppressed emission quenching at the QDs emitting layer/electron transport layer interface by passivating ZnMgO nanocrystals with acrylate species (Figure 1. 20).[58] The short carboxylic acid with acrylate positively affects QLEDs by reducing hydroxyl species and oxygen vacancies on the surface of ZnMgO nanocrystals. Furthermore, F. Chen *et al*. confirmed the effects of energy band alignment and defect elimination simultaneously via Cl-passivation on ZnMgO nanocrystals.[59] By upshifting the conduction band level, the electron injection barrier was lowered and the exciton quenching of QDs was suppressed.

The most critical factor for high performance is defect control of the active layer material as well as interface passivation between layers. D. Park *et al*. developed new halide ligands for oleic acid-capped PbS nanocrystals.[60] They adapted triethylamine hydroiodide, which is optimized for stripping oleate ligands rather than conventional tetra-*n*-butylammonium iodide. In turn, the trap density of the active layer was reduced, and the electron mobility was improved. Defect engineering is particularly vital in perovskite materials owing to their ionic bonding feature and facile ion mobility. By acid etching, C. Bi *et al*. removed numerous defects in 4 nm sizes of $CsPbBr_3$ nanocrystals.[61] The surface energy of nanocrystals was increased by the etching step, and the uncoordinated sites were reduced with didodecylamine and phenethylamine ligands. They achieved an efficiency of 4.7% in the blue region and a high operating lifetime of 12 h.

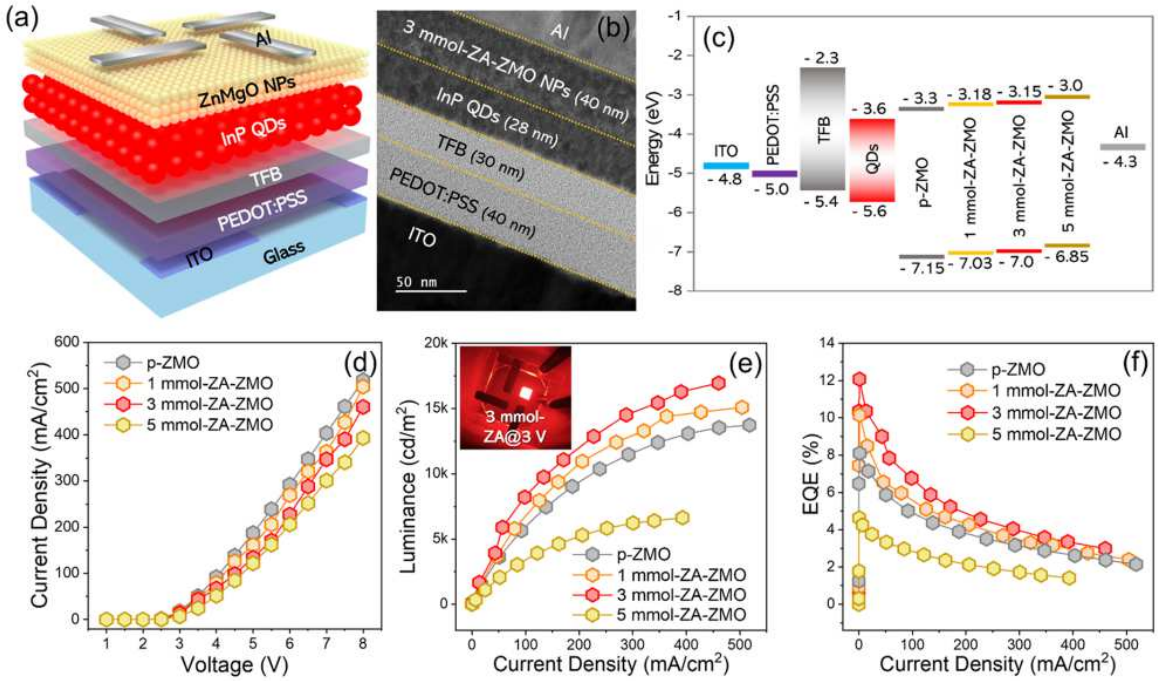

Figure 1.20. (a) Multilayered device schematic of all-solution-processed red QLED and (b) cross-sectional TEM image of a representative device integrated with 3 mmol-ZA-ZMO NP-based ETL. (c) Energy band levels, (d) current density−voltage, (e) luminance−current density, and (f) EQE−current density of red QLEDs integrated with p-ZMO and a series of acrylate-functionalized ZMO ETLs. Reproduced with permission from ref. 58. Copyright © 2022, American Chemical Society.

Role of interface/surface engineering: Communication between materials

Since the nanomaterial layer of optoelectronics is a microscopic assembly, interparticle distance, packing density, and orientation are significant characteristics. They regulate optical and electrical communication between nanomaterials. For example, nanoparticles containing short alkyl chain ligands increase charge transport efficiency in LEDs. Y-.H. Won *et al*. decreased the organic content from 13 wt% to 8 wt% by replacing the oleic acid ligand of InP QDs with hexanoic acid.[62] Additionally, as the interparticle distance shrank, the hole current multiplied four times, and the stability of devices was significantly enhanced. L. Sun *et al*. compared the efficiency of QLEDs by adjusting the thiol ligand length of PbS nanocrystals in angstrom units.[63] The ligand with the highest external quantum efficiency of 2.0% was 8-mercaptooctanoic acid with 7 CH_2 groups in the linker molecule. Moreover, the morphology and thickness of the film can be managed through the interface/surface engineering of the material. K. Lu *et al*. reported a novel solid-state ligand exchange method that forms PbS films with a thickness of ~1 um in one step.[64] They adjusted the packing of the nanocrystal to produce a smooth film without crack formation.

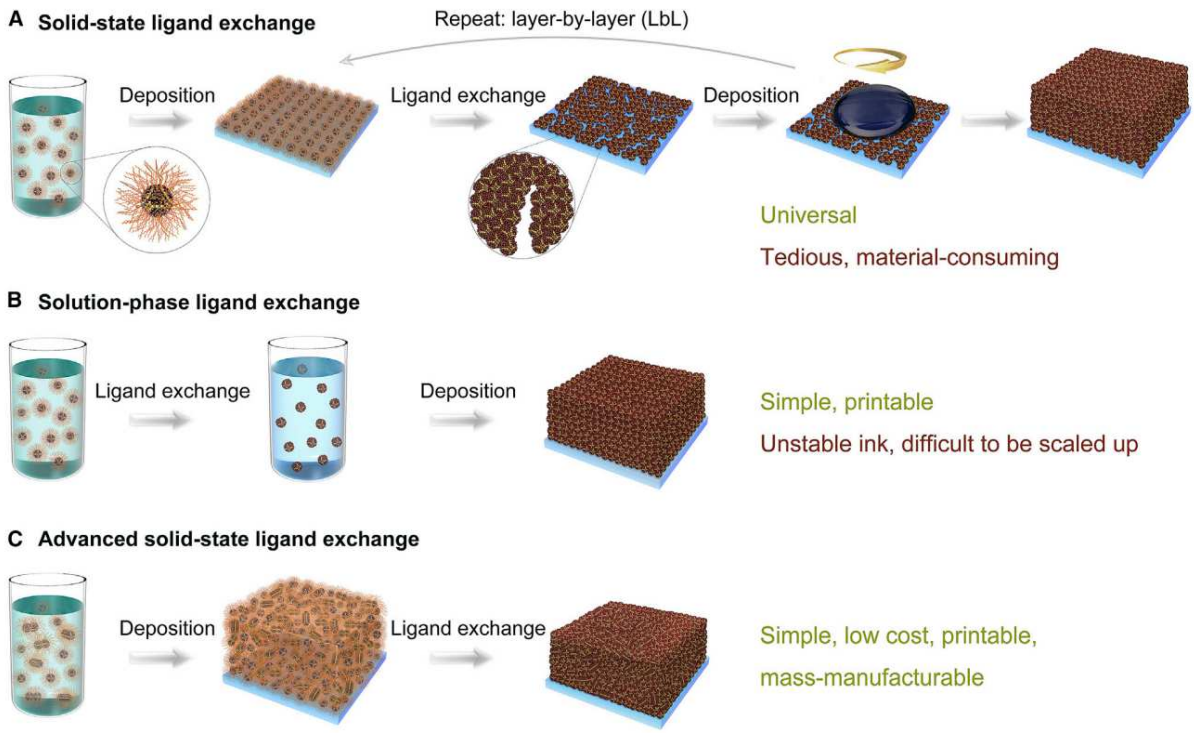

Figure 1.21. Schematic representation of different preparations for semiconductive NCs films (a) Solid-state ligand exchange: the NCs are first deposited on substrate and then ligand exchanged. The cracks formed in the bottom layer can be filled or covered by the subsequent layers. (b) Solution-phase ligand exchange: the ligand exchange process is conducted in solution. Then, the exchanged NC ink is dispersed in solvents such as dimethylformamide, formamide, and butylamine, which can be deposited into solid film directly. (c) Advanced solid-state ligand exchange: the NC mixture (dots and dimers) dispersed in nonpolar solution (hexane, octane etc.) is deposited on a substrate, which is then ligand exchanged to obtain crack-free, thick, and semiconductive NC film in only 1 step. Reproduced with permission from ref. 64. Copyright © 2020, Cell Press.

Surface modification based on catechol groups for photovoltaics

Catechol-containing structures found in living organisms such as mussels, sandcastle worms, and geckos show a variety of physicochemical properties like antioxidant, anti-inflammatory, redox capacity, metallic chelation, and adhesion.[65] In this section, we introduced examples of surface engineering with catechol groups for highly efficient photovoltaics.

The catechol group has been widely used in dye-sensitized solar cells (DSSC) due to a strong binding affinity with TiO_2 electrodes. H. J. Nam *et al*. introduced polydopamine layers into the TiO_2 electrodes as photosensitizers (Figure 1.22a).[66] Although polydopamine is suitable as a sensitizer because of forming a strong bidentate complex with unsaturated Ti atom, it has disadvantages such as structure uncertainty and difficulty in coating control by self-polymerization. They modulated the polymerization of dopamine with an N_2-saturated pH 8.5 tris(hydroxymethyl) aminomethane (THAM) solution. Additionally, the performance of DSSCs was evaluated by coating them using two different techniques: dip coating and electrochemical oxidation with cyclic voltammetry. The fabricated DSSCs showed the highest efficiency of 1.2% when the polydopamine layer was obtained by dip coating. The THAM buffer solution increases the solubility of dopamine more than five times and inhibits indiscriminate polymerization. They confirmed that the efficiency of DSSCs dropped rapidly to less than 0.1% when the polydopamine was coated with TiO_2 in alcohol and water. This paper demonstrates the feasibility of using polydopamine layers in polymer-sensitized solar cells.

T. Higashino *et al*. introduced the thiazolocatechol group as an anchoring group to the TiO_2 electrode in DSSCs (Figure 1.22b).[67] The carboxylic acid is often used as an anchoring group because it can be easily synthesized and bound to TiO_2. However, the binding with TiO_2 is lost during cell operation, resulting in poor long-term stability. The catechol group has been extensively studied as a substitute for carboxylic acid, but the performance of DSSCs is low due to the electron-donating ability of the hydroxyl group in the catechol group. The authors introduced an electron-withdrawing thiazole moiety to the anchoring group to minimize the electron-donating ability of catechol groups. They substituted thiazolocatechol for the carboxylphenyl group of YD2-*o*-C8, a famous push-pull porphyrin sensitizer. The designed thiazolocatechol anchor showed the binding mode of symmetrical bidentate coordination to TiO_2. The photovoltaic performance of the DSSC exhibited an efficiency of 4.87%, which is the first time broken through the 4% barrier in catechol-based sensitizers.

Donor-π-catechol sensitizers suitable for type II DSSCs were developed in 2014 by Y. Ooyama *et al* (Figure 1.23).[68] They designed sensitizers using the diphenylamine moiety as the electron-donating group and changing the π-conjugation system to fluorene, carbazole, or carbazole-terthiophene. In type II DSSCs, electrons are directly injected from the highest occupied molecular orbital (HOMO) of the sensitizer into the conduction band of TiO_2 upon photoexcitation. This structure has the advantage of light harvesting over a wide spectral range.

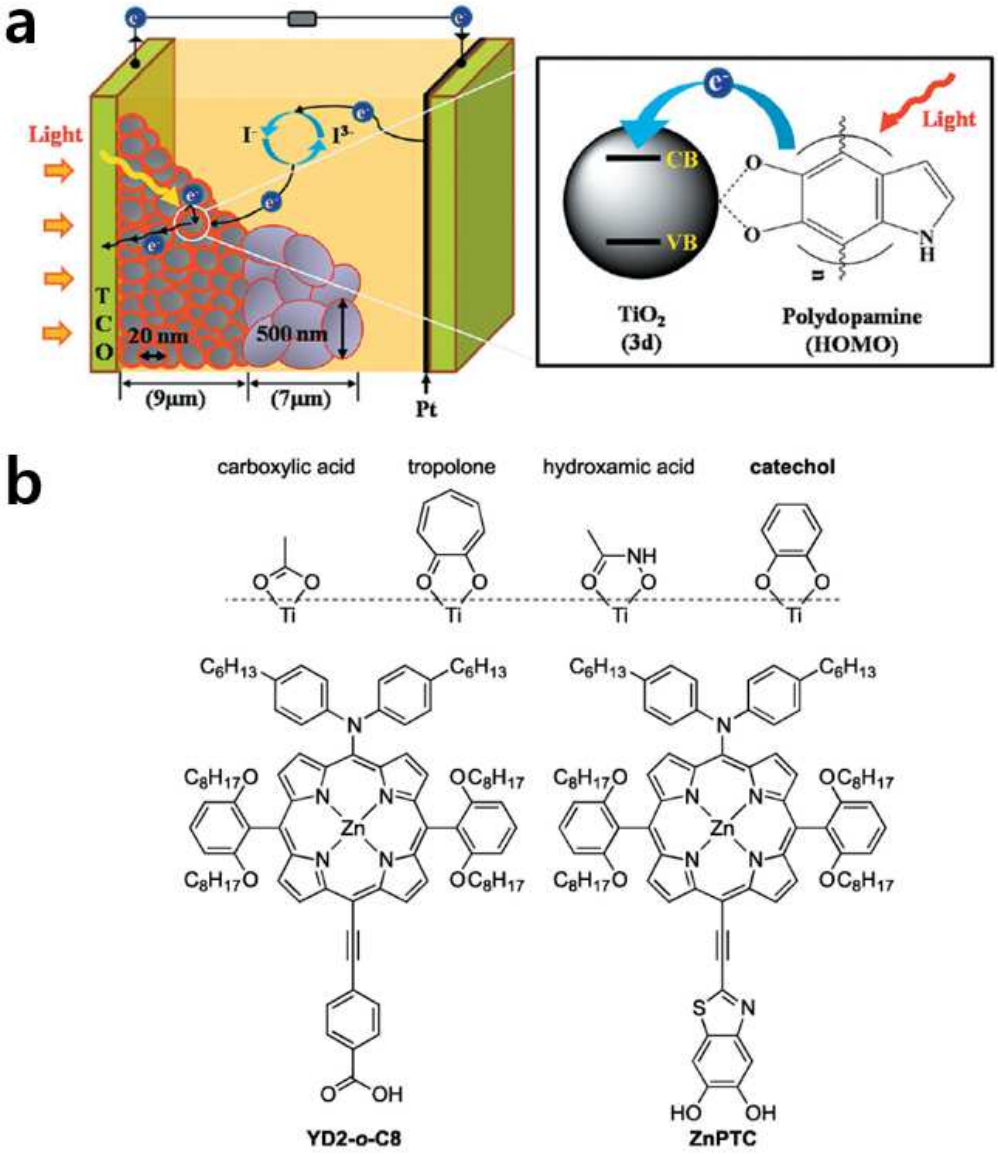

Figure 1.22. (a) Schematic illustration of PDA-sensitized solar cells showing the photoinduced charge transfer process. Reproduced with permission from ref. 66. Copyright © 2012, Wiley-VCH. (b) Possible binding modes for anchoring groups on TiO_2 and molecular structures of porphyrin sensitizers. Reproduced with permission from ref. 67. Copyright © 2019, Wiley-VCH.

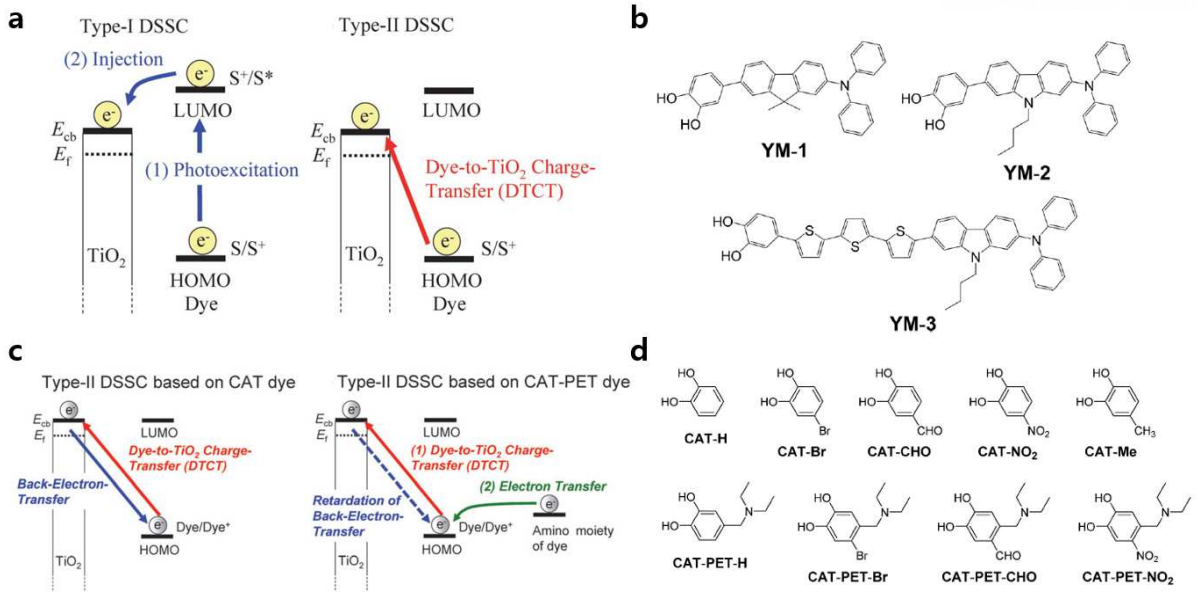

Figure 1.23. (a) Schematic representation of type-I DSSC and type-II DSSC, (b) Chemical structures of D–π–Cat dye sensitizers YM-1, YM-2 and YM-3. Reproduced with permission from ref. 68. Copyright © 2014, The Royal Society of Chemistry. (c) Electron-injection pathway from the dye to the CB of the TiO_2 electrode for a type-II DSSC based on CAT dye and a type-II DSSC based on CAT-PET dye. (d) Chemical structures of CAT and CAT-PET dyes with various substituents. Reproduced with permission from ref. 69. Copyright © 2017, The Royal Society of Chemistry.

They investigated the electron injection mechanism depending on the molecular structure of catechol-based dyes and compared the influence of dye-to-TiO_2 energy transfer on device performance. The expansion of the π -conjugation system by introducing terthiophene increased intramolecular charge transfer and decreased the dye-to-TiO_2 energy transfer, resulting in improved indirect electron injection in the device.

After three years, they expanded their work and proposed catechol-based sensitizers suitable for type II DSSCs. The authors compared device performance by adding a diethylamino group to catechol-based dyes with various electron-withdrawing substituents on the catechol unit (Figure 1.23d).[69] The diethylamino group, an electron donor moiety, improved device efficiency by retarding back-electron transfer in type II DSSCs structures. Except for CAT-PET-NO_2, it was found that the photovoltaic performances of the DSSCs based on CAT-PET dyes are superior to those of CAT dyes without PET features. Photo-induced electron transfer promotes the electron injection from the ground state of catechol to the conduction band of the TiO_2 electrode.

The catechol group has been used as an anchoring group and sensitizer in DSSCs and as an additive to hole transport layers (HTL) in other photovoltaic systems. For example, P. Huang *et al*. suggested 3,4-dihydroxyphenylalanine (DOPA), 4-dihydroxybenzhydrazide (DOBD), and norepinephrine (NE) as dopants for the HTL material, poly(3,4-ethylenedioxythiophene):polystyrene-sulfonate (PEDOT:PSS) (Figure 1.24).[70] PEDOT:PSS is frequently used as HTL in p-i-n perovskite solar cells owing to good hole mobility and solution processability. The catechol dopants enhanced the crystallinity and formed the smooth morphology of the perovskite films. These results were modulated by the interaction between NR_3^+ of the catechol group and PEDOT, and DOBD was more effective than DOPA and NE. In addition, the dopant induced the separation of the PEDOT and PSS phases, reducing charge accumulation and facilitating hole transport. The optimized p-i-n perovskite solar cell showed a power conversion efficiency (PCE) of 17.46%, which was higher than 13.53% in the absence of catechol-based dopants. This dopant also improved the stability of the device by weakening the acidity of PEDOT:PSS.

Q. Xue *et al*. conducted similar research on adding dopamine to PEDOT:PSS in perovskite solar cells (Figure 1.25).[71] The valence band maximum of $CH_3NH_3PbI_3$ perovskite film is -5.4 eV, which differs from the work function of PEDOT:PSS (-5.1 eV), resulting in a decrease in device performance. The authors confirmed that dopamine-doped PEDOT:PSS has high radical contents and is effective at charge extraction through several analyzes, including electron spin resonance spectroscopy, time-resolved photoluminescence, and transient photovoltage measurements. Dopamine in PEDOT:PSS not only increased the crystallinity of perovskite films but also passivated the surface defect of perovskite by using the amine and hydroxyl groups of dopamine. Furthermore, dopamine reduced the hole transport barrier by increasing the work function of PEDOT:PSS from -5.1 eV to -5.3 eV. As a result, the optimized device showed a PCE of 18.5%, which was the best performance in a perovskite-based inverted heterojunction solar cell at that time. This device exhibited high stability, losing only 20% of the efficiency after 250 h without encapsulation in the air.

The dopamine doping effect was also demonstrated in organic solar cells as well as perovskite solar cells (Figure 1.26).[72] Dopamine increased the work function and conductivity of HTL by reacting with the remaining sulfonic acid in PSS. The increased work function from -5.00 eV to -5.14 eV matched the HOMO energy level of poly[(2,6-(4,8-*bis*(5-(2-ethylhexyl)-4-fluorothiophen-2-yl)benzo[1,2-b:4,5-b′]dithio-phene))-*co*-(1,3-di(5-thiophene-2-yl)-5,7-*bis*(2-ethylhexyl)-benzo[1,2-c:4,5-c′]dithiophene-4,8-dione))] (PM6) compared to the existing PEDOT:PSS, improving the efficiency of the device. The PSS-dopamine complexes help stacking the PEDOT backbone and increase the conductivity of PEDOT:PSS. The fabricated device showed a PCE of 16.55%, which was the highest efficiency in organic solar cells at that time. Moreover, this strategy could be applicable regardless of the organic materials in the active layer.

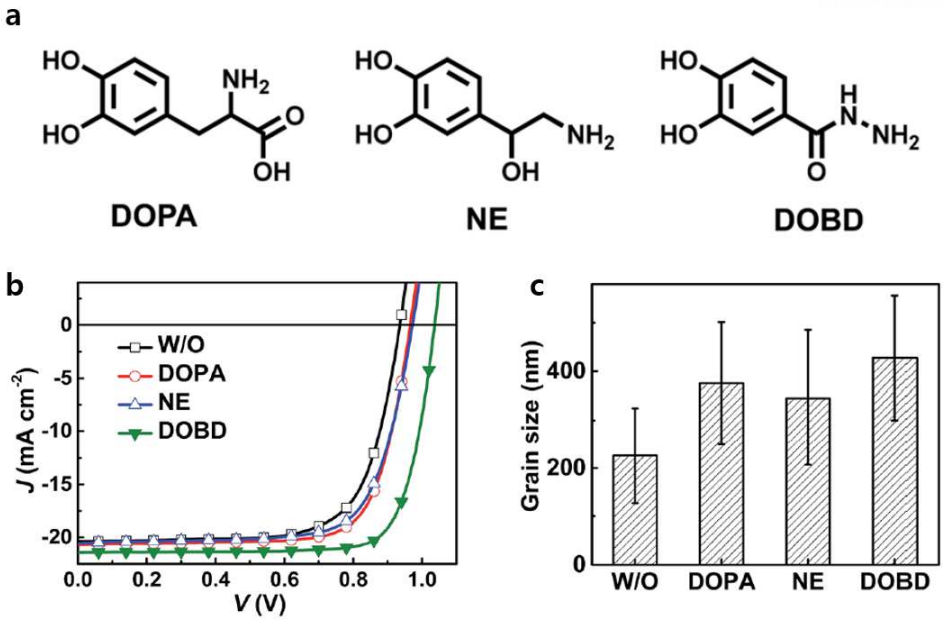

Figure 1.24. (a) Molecular structures of catechol derivatives. (b) Typical *J–V* curves of Pero-SCs with neat PEDOT:PSS (black, empty square), and DOPA- (red, empty circle), NE- (blue, triangle) and DOBD-PEDOT:PSS (green, solid triangle) as HTLs. (c) The size analysis of the crystal grains in the perovskite films on the neat/doped PEDOT:PSS. Reproduced with permission from ref. 70. Copyright © 2017, The Royal Society of Chemistry.

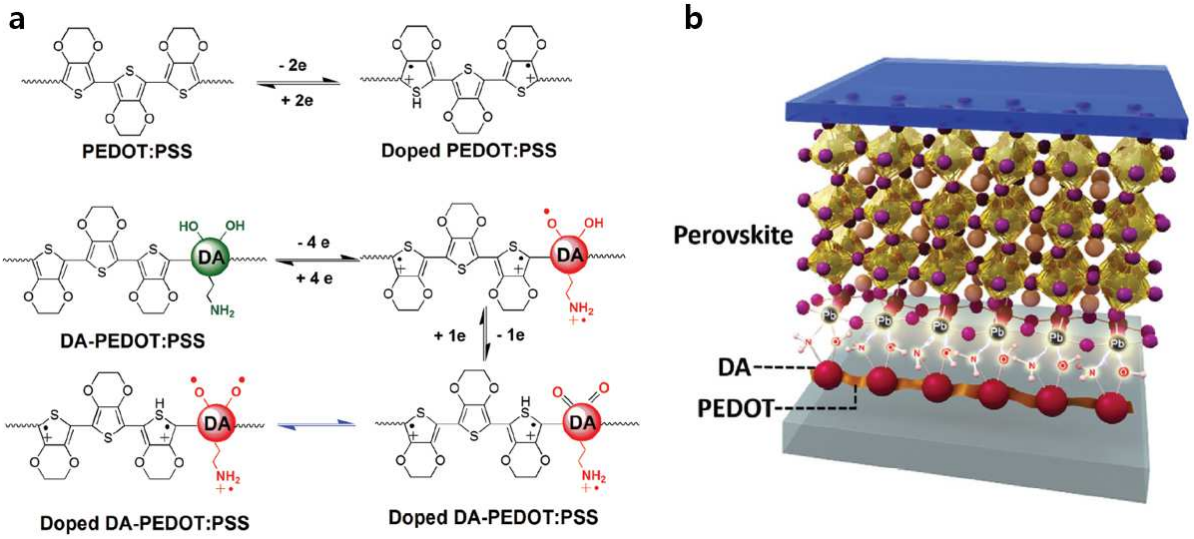

Figure 1.25. (a) Considerable differences in doping of PEDOT:PSS and DA-PEDOT:PSS: DA semiquinone radicals yield a greater electron donating effect for trap passivation. (b) Potential passivation effect: interactions between undercoordinated Pb atoms on the perovskite crystal and DA-PEDOT:PSS with amino and hydroxyl groups. Reproduced with permission from ref. 71. Copyright © 2018, Wiley-VCH.

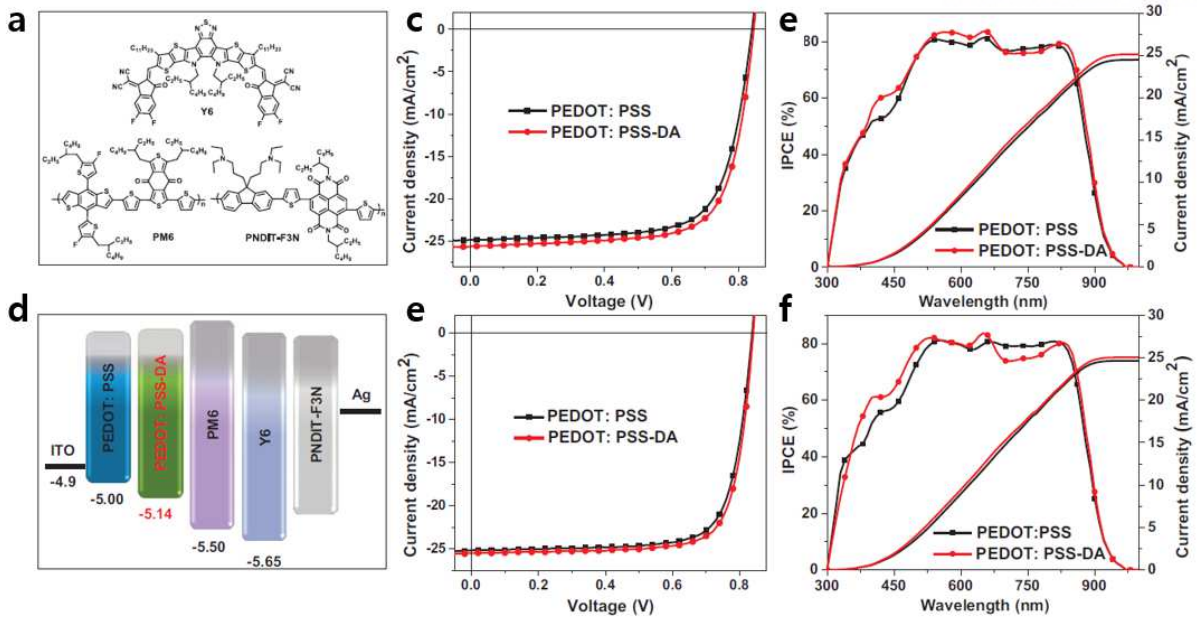

Figure 1.26. (a) The molecular structure of PM6, Y6, and PNDIT-F3N. (b) Schematic energy level diagrams of the materials and device structure of the OSCs. (c) *J–V* and (e) IPCE curves of the devices with the as-cast PM6:Y6 system. (d) *J–V* and (f) IPCE curves of the devices with optimized PM6:Y6 system. Reproduced with permission from ref. 72. Copyright © 2020, Wiley-VCH.

M. Hou *et al*. suggested a catechol-based interlayer between the electron transport layer (ETL) and the perovskite active layer (Figure 1.27).[73] The authors increased the efficiency of perovskite solar cells by forming a self-assembled dopamine monolayer on SnO_2. The catechol group of dopamine bind to the uncoordinated cation on the surface of SnO_2, and the amino group interact with perovskite by hydrogen bonding. This interlayer improved perovskite crystallinity and reduced interface defects. In addition, π- conjugated benzene structure aided electron transport. Consequently, solar cells introduced with a dopamine self-assembly monolayer exhibited a high PCE of 16.87%.

J. Zhang *et al*. enhanced the stability and efficiency of photovoltaics by applying catechol groups directly to the perovskite layer rather than the interlayer or charge transport layer.[74] Based on the Lewis acid-base interaction, the dopamine additive effectively reduced the uncoordinated Pb^{2+} defects and Pb^0, I^- defects. The catechol treatment induced the crystallographic orientation of perovskite stronger toward the (110) plane. Furthermore, dopamine upshifts the valence band of perovskite to match the HOMO energy level of HTL. They fabricated a device with an efficiency of 21.03% under an optimized structure, ITO/SnO_2/$Cs_{0.05}(FA_{0.83}MA_{0.17})_{0.95}Pb(I_{0.83}Br_{0.17})_3$:dopamine/spiro-MeTAD/$MoO_3$/Ag. This work describes an easy and efficient method for increasing the stability and performance of photovoltaics through dopamine treatment.

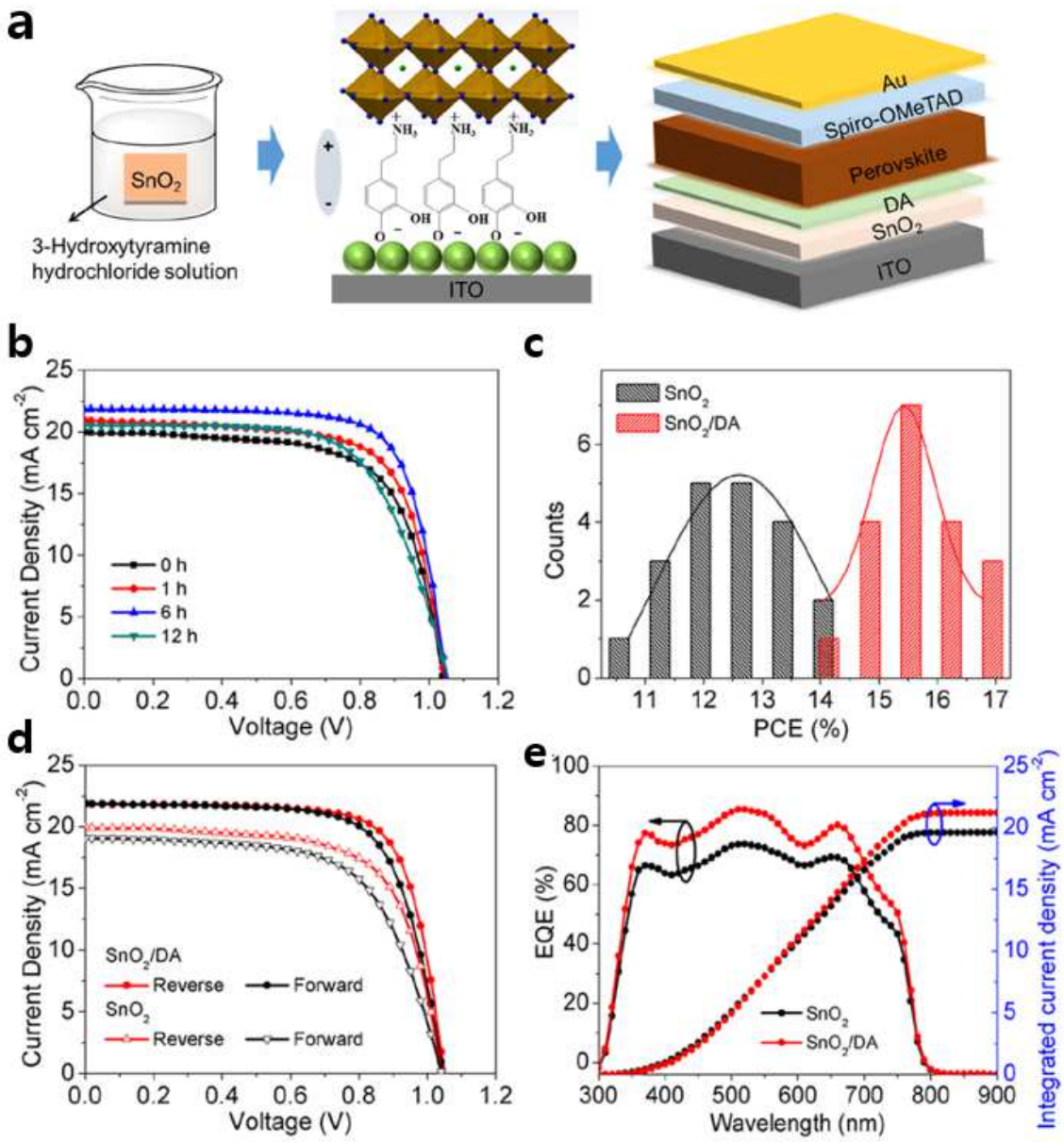

Figure 1.27. (a) Schematic diagram of the dopamine self-assembled monolayer between SnO_2 ETL and perovskite, (b) Best PCE of the devices with different DA treatment times and (c) histogram of efficiencies among 20 devices. (d) *J*–*V* curves measured under reverse and forward voltage scanning and (e) EQE of the devices deposited on SnO_2 ETL with or without a DA SAM modification. Reproduced with permission from ref. 73. Copyright © 2018, American Chemical Society.

Surface passivation of metal halide perovskite materials for LEDs

Perovskite is a material with a crystal structure as $CaTiO_3$ and was initially discovered in the Ural Mountains by Gustav Rose in 1839 and named by Lev Perovski, a Russian geologist. Among the various perovskite structures, metal halide perovskites (MHP) have a general chemical formula of ABX_3, where A-site has been used by Cs^+, $CH_3NH_3^+$(methylammonium, MA), and $CH(NH_2)_2^+$ (formamidinium, FA), B-site is Pb^{2+}, Sn^{2+}, and X-site is a halogen ion (Cl^-, Br^-, and I^-) (Figure 1.28a).[75] These materials have recently attracted attention as next-generation display materials based on their benefits, such as high photoluminescence quantum yield (PLQY), high color purity, solution processability, bandgap tunability, and an easy synthetic method (Figure 1.28b-e).[76-79] In addition, MHPs are mainly composed of ionic bonds, unlike conventional semiconductor QDs such as Si, CdSe, and InP QDs. The MHPs crystals are easily synthesized and can be mass products because of the relatively low lattice formation enthalpy. Moreover, MHPs have a defect tolerance characteristic because they have a unique energy band structure. As shown in Figure 1.28f, the 6s orbital of Pb and the p orbital of halogen generate an antibonding orbital bond, and the band gap of MHPs is formed between the antibonding orbitals.[80] Therefore, even if there are defects in MHPs, the deep trap states are suppressed between the band gaps, and shallow trap states are mainly formed. Defect-tolerant MHPs have a high PLQY of close to 100% and a narrow full width at half maximum (FHWM) of 10 to 40 nm with only the core itself without shell overcoating. Based on these characteristics, perovskite LEDs have developed rapidly since they were demonstrated in 2014 and currently show an EQE of 23.0%, 23.4%, and 12.3% in the red, green, and blue regions, respectively.[81-84] In this section, we summarize remarkable surface engineering methods to improve the efficiency of perovskite LEDs.

The researchers have tried to reduce the dimension of 3D perovskite film through surfactant treatment to increase the exciton binding energy. Z. Xiao *et al*. added large *n*-butylammonium (BA) halides to $MAPbI_3$ and $MAPbBr_3$ perovskite films to reduce the crystal size of perovskite and increase exciton confinement.[85] The 3D perovskite grain size of hundreds of nm was reduced to 10 nm, and the film surface became smooth with a roughness of less than 1 nm. As a result, the external quantum efficiency (EQE) of the LED fabricated with $MAPbI_3$ perovskite increased from 1.0% to 10.4% after BAI treatment. This strategy was similarly applied to another halide, and the efficiency of $MAPbBr_3$ LED also increased from 0.03% to 9.3%. The bulk organic ligands contributed to the stability of the LED by passivating the nanocrystalline surface and suppressing ion migration. BAX-treated LEDs showed little degradation in performance for more than eight months in a glove box.

An EQE of over 20% of perovskite LEDs was first reported by K. Lin *et al*., which far exceeded previous EQEs of less than 15% in the visible light region. They obtained a quasi-core/shell structure by mixing pre-synthesized $CsPbBr_3$ perovskite with MABr additives (Figure 1.29).[86] The compositionally graded structure was naturally formed via the difference in solubility and crystallinity of perovskite materials and MABr additives.

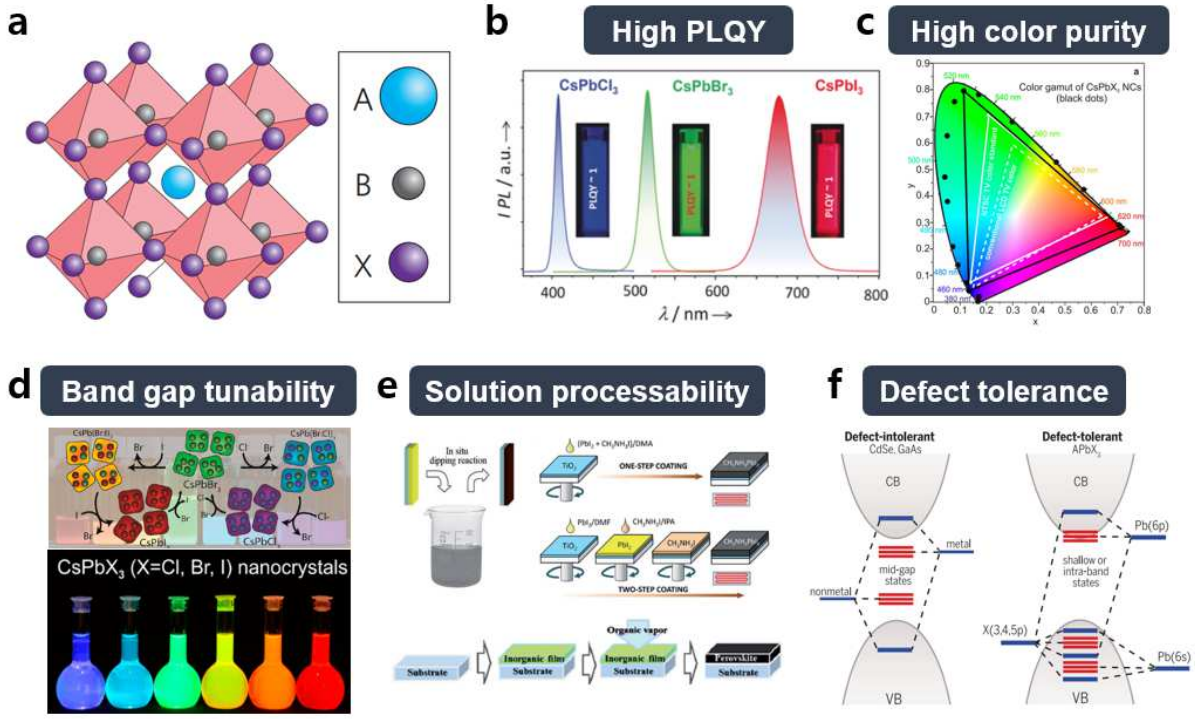

Figure 1.28. (a) Scheme of perovskite crystal structure. Reproduced with permission from ref. 75. Copyright © 2014, Springer Nature. (b) Near unity photoluminescence quantum yield of CsPbX3 (X=Cl, Br, and I) nanocrystals (NCs). Reproduced with permission from ref. 76. Copyright © 2019, Wiley-VCH. (c) Emission from CsPbX3 NCs (black data points) plotted on CEI chromaticity coordinates and compared to most common color standards. Reproduced with permission from ref. 77. Copyright © 2015, American Chemical Society. (d) Anion exchange reactions on CsPbX3 NCs. Reproduced with permission from ref. 78. Copyright © 2015, American Chemical Society. (e) Solution processes for preparing perovskite films. Reproduced with permission from ref. 79. Copyright © 2015, The Royal Society of Chemistry. (f) Schematics comparing electronic structures that are defect-intolerant and defect-tolerant. Reproduced with permission from ref. 80. Copyright © 2017, American Association for the Advancement of Science.

The MABr shell passivated the nonradiative defect of $CsPbBr_3$ and helped balance the charge injection. The obtained perovskite films showed an EQE of 17% for perovskite LEDs. The authors inserted a poly(methyl methacrylate) layer between the ETL and the perovskite layer to enhance the efficiency of LEDs. The optimized device displayed an EQE of 20.3% after adjusting the electron and hole balance by reducing the electron injection.

Perovskite nanocrystals (NCs) have excellent optical properties due to high exciton binding energy but have drawbacks such as low stability and low charge-carrier transport efficiency. Surface ligands are easily detached to form defects, and long alkyl chain ligands interfere with charge transport owing to their insulating properties. J. H. Park *et al*. increased the efficiency of LED by replacing the original oleylamine ligand of $CsPbBr_3$ NCs with various quaternary ammonium bromide (QAB) ligands (Figure 1.30).[87] The authors systematically monitored the stability and optical properties of $CsPbBr_3$ NCs by controlling the carbon chain length and bulkiness of QAB ligands. The coverage of the ligand on the NCs' surface is affected by the number of octyl groups in the QAB ligands. As the steric hindrance between the ligands increases, the coverage of the ligand on the NCs decreases, resulting in low colloidal stability. The authors revealed that the carbon chain length affected the charge-carrier transport, and QAB ligands with ten carbons had the optimal charge-carrier balance. Fabricated devices exhibited a maximum luminance of 2269 cd/m^2 and an EQE of 9.71%.

Although blue-emitting LEDs in MHPs can be easily achieved with a mixture of Br and Cl, there are problems with efficiency drop due to chlorine vacancy and phase segregation. These chlorine vacancies create deeper trap states within the band gap to capture charge carriers and suppress radiative recombination. Furthermore, ion migration originating from halide vacancy induces phase segregation during device operation. X. Zheng *et al*. reported the strategy for passivating Cl vacancy by adding pseudohalide *n*-dodecylammmonium thiocyanate (DAT).[88] The thiocyanate group filled the Cl vacancy and reduced the electron trap state, showing the near unit PLQY of $CsPb(Br_xCl_{1-x})_3$ QDs. The DAT ligands containing long carbon chains are convenient to apply to MHP QDs because of their high solubility in non-polar solvents. They achieved an EQE of 6.6% at 471 nm, close to pure blue. Efficiency was significantly improved compared to the previous blue perovskite LEDs, but operational stability was low.

In order to obtain blue-emitting LEDs in MHPs, there is another way to engineer the dimension of Br-based perovskite materials using the quantum confinement effect. Since the exciton Bohr radius of $CsPbBr_3$ is 7 nm, the bandgap gradually increases as the size of QDs decreases. The $CsPbBr_3$ QDs with a size of 4 nm have a blue emission wavelength of ~470 nm. However, small-sized perovskite QDs show poor optical properties and stability due to their high surface area. C. Bi *et al*. demonstrated stable blue LEDs based on $CsPbBr_3$ QDs using a novel acid etching-driven ligand exchange strategy (Figure 1.31).[61] They etched the imperfect $[PbBr_6]^{4-}$ octahedrons by adding hydrogen bromide immediately after Cs-oleate injection.

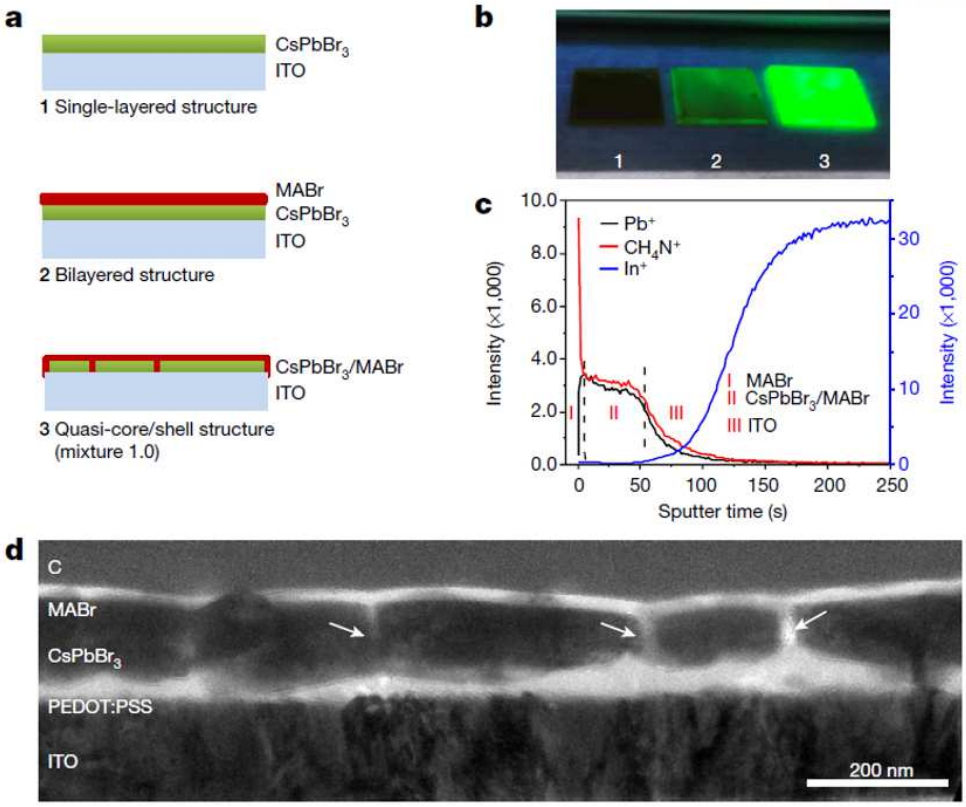

Figure 1.29. (a) Schematic illustrations of single-layered $CsPbBr_3$, bilayered $CsPbBr_3$/MABr, and quasi-core/shell $CsPbBr_3$/MABr structures, all fabricated on ITO substrates. (b) Photographs of the three as-prepared perovskite films under ultraviolet light. (c) SIMS depth analysis of the as-prepared quasi-core/shell $CsPbBr_3$/MABr structure on ITO glass. (d) Cross-sectional TEM image of the quasi-core/shell $CsPbBr_3$/MABr structure on PEDOT:PSS. White arrows indicate the MABr shell (the grain boundary). Reproduced with permission from ref. 86. Copyright © 2018, Springer Nature.

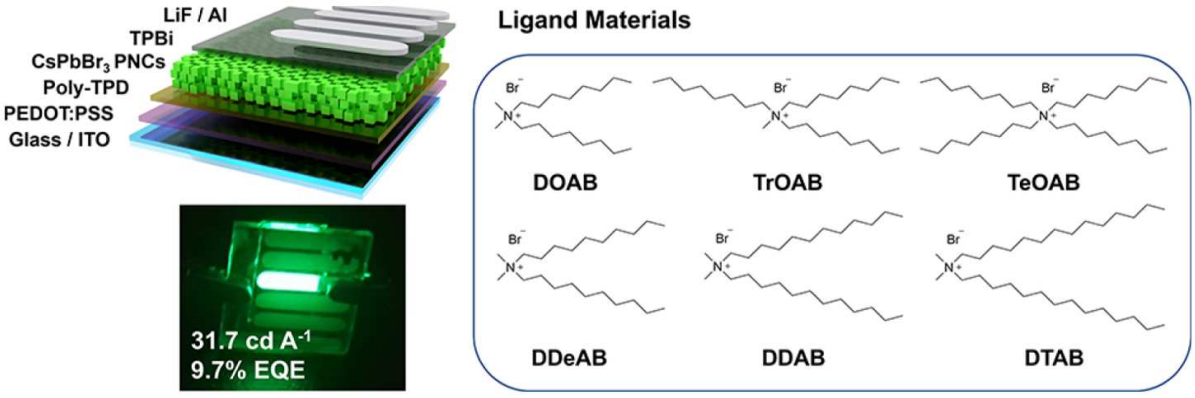

Figure 1.30. Schematic of LED structures and chemical structures of various ligand materials with different bulkiness and length. Reproduced with permission from ref. 87. Copyright © 2019, American Chemical Society.

The excess oleic acid ligands were also desorbed from the surface of the $CsPbBr_3$ QDs during the etching process. The authors successively introduced the didodecylamine and phenethylamine ligands to passivate the uncovered surface. The surface-treated $CsPbBr_3$ QDs showed a PLQY of 97% and FWHM of 23 nm at the emission wavelength of 458 nm. Then, they achieved an EQE of 4.7% and a maximum luminance of 3850 cd/m^2 in the pure blue region. Surprisingly, the device exhibited a long-term half-lifetime of 12 h at the luminance of 102 cd/m^2. They synthesized highly stable $CsPbBr_3$ QDs enough to use ZnO NCs dispersed in a polar solution as an ETL material on the perovskite layer.

In addition to having high PLQYs of QDs, highly efficient LEDs also require the formation of a compact and stable QD solid film. A bipolar-shell resurfacing strategy was presented to obtain high-quality QD solids by removing the long-chain organic ligand (Figure 1.32).[81] The bipolar shell consists of an inner anion shell and an outer cation shell of isopropylammonium and sodium cations. The compact bipolar QD solid has a ten times lower trap density and 100 times greater carrier mobility than conventional perovskite films. This approach applied to a wide variety of perovskites, regardless of size or morphology. They achieved an EQE of 12.3% for blue devices and 22% for green devices, opening the possibility for use in next-generation LEDs.

Y.-H. Kim *et al*. presented a novel defect suppression strategy by doping guanidinium into $FAPbBr_3$ NCs.[89] They employed zero-dipole guanidium cation to stabilize bulk entropy and improve the excitonic confinement. Then, they treated 1,3,5-tris(bromomethyl)-2,4,6-triethylbenzene to remove remaining halide vacancies and minimize nonradiative recombination. These synergistic strategies resulted in a current efficiency of 108 cd/A and an EQE of 23.4%.

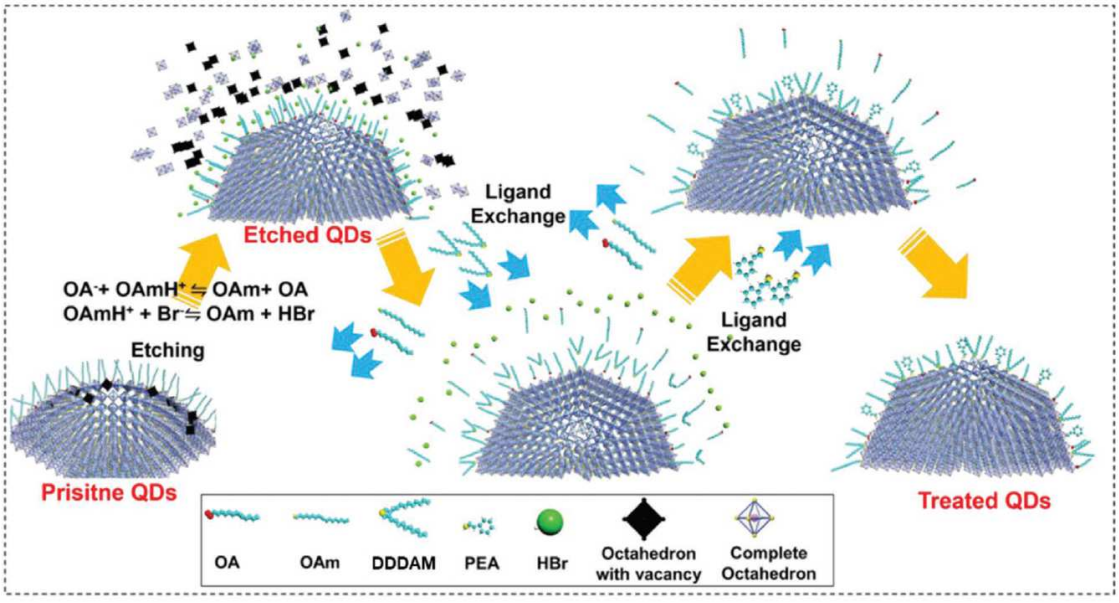

Figure 1.31. Schematic illustration of ligand exchange process driven by acid etching. Reproduced with permission from ref. 61. Copyright © 2021, Wiley-VCH.

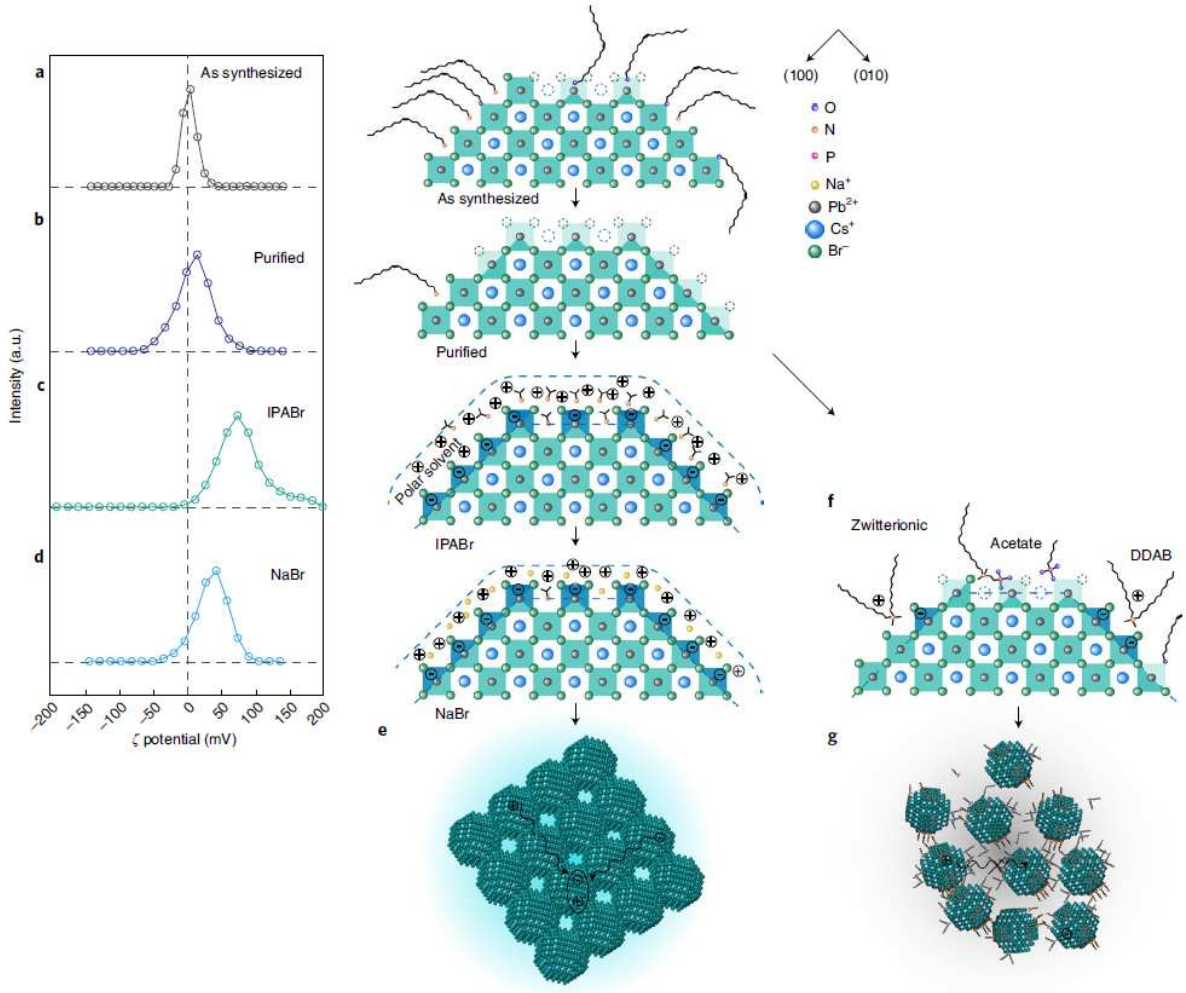

Figure 1.32. (a)–(d) ζ potentials (left) and schematics (right) of QD surfaces. (a) The surface of as-synthesized perovskite QDs showing near-zero ζ potential. (b) Purified QDs with surface defects and exhibiting slight positive charges. (c) QD resurfacing with isopropylammonium bromide. Surface vacancies were passivated and a bipolar solvent shell formed around the surface of the QDs. (d) QD surface following cation substitution using Na^+. (e) Solids formed with resurfaced perovskite QDs with high PLQYs. (f) QD surface passivated with traditional long-chain organic ligands. (g) Film cast from perovskite QDs with long-chain organic ligands. Reproduced with permission from ref. 81. Copyright © 2020, Springer Nature.

1.4 References

(1) Feynman, R. P. There's Plenty of Room at the Bottom. *Eng. Sci.* **1960**, *23*, 22–36.

(2) Poh, T. Y.; Ali, N. A. t. B. M.; Mac Aogáin, M.; Kathawala, M. H.; Setyawati, M. I.; Ng, K. W.; Chotirmall, S. H. Inhaled Nanomaterials and the Respiratory Microbiome: Clinical, Immunological and Toxicological Perspectives. *Particle and Fibre Toxicology* **2018**, *15*.

(3) Georgakilas, V.; Perman, J. A.; Tucek, J.; Zboril, R. Broad Family of Carbon Nanoallotropes: Classification, Chemistry, and Applications of Fullerenes, Carbon Dots, Nanotubes, Graphene, Nanodiamonds, and Combined Superstructures. *Chem. Rev. (Washington, DC, U. S.)* **2015**, *115*, 4744-4822.

(4) Kroto, H. W.; Heath, J. R.; O'Brien, S. C.; Curl, R. F.; Smalley, R. E. C60: Buckminsterfullerene. *Nature* **1985**, *318*, 162-163.

(5) Iijima, S. Helical Microtubules of Graphitic Carbon. *Nature* **1991**, *354*, 56-58.

(6) Bethune, D. S.; Kiang, C. H.; de Vries, M. S.; Gorman, G.; Savoy, R.; Vazquez, J.; Beyers, R. Cobalt-catalysed Growth of Carbon Nanotubes with Single-Atomic-Layer Walls. *Nature* **1993**, *363*, 605-607.

(7) Iijima, S.; Ichihashi, T. Single-shell Carbon Nanotubes of 1-nm Diameter. *Nature* **1993**, *363*, 603-605.

(8) Novoselov, K. S.; Geim, A. K.; Morozov, S. V.; Jiang, D.; Zhang, Y.; Dubonos, S. V.; Grigorieva, I. V.; Firsov, A. A. Electric Field Effect in Atomically Thin Carbon Films. *Science* **2004**, *306*, 666-669.

(9) Lin, L.; Bi, X.; Gu, Y.; Wang, F.; Ye, J. Surface-enhanced Raman Scattering Nanotags for Bioimaging. *J. Appl. Phys.* **2021**, *129*, 191101.

(10) Kuisma, M.; Sakko, A.; Rossi, T. P.; Larsen, A. H.; Enkovaara, J.; Lehtovaara, L.; Rantala, T. T. Localized Surface Plasmon Resonance in Silver Nanoparticles: Atomistic First-Principles Time-Dependent Density-Functional Theory Calculations. *Physical Review B* **2015**, *91*, 115431.

(11) Amendola, V.; Pilot, R.; Frasconi, M.; Maragò, O. M.; Iatì, M. A. Surface Plasmon Resonance in Gold Nanoparticles: a review. *J. Phys.: Condens. Matter* **2017**, *29*, 203002.

(12) Dreaden, E. C.; Alkilany, A. M.; Huang, X.; Murphy, C. J.; El-Sayed, M. A. The Golden Age: Gold Nanoparticles for Biomedicine. *Chem. Soc. Rev.* **2012**, *41*, 2740-2779.

(13) Fei Guo, C.; Sun, T.; Cao, F.; Liu, Q.; Ren, Z. Metallic Nanostructures for Light Trapping in Energy-Harvesting Devices. *Light: Science & Applications* **2014**, *3*, e161-e161.

(14) Chen, J.; Shi, S.; Su, R.; Qi, W.; Huang, R.; Wang, M.; Wang, L.; He, Z. Optimization and Application of Reflective LSPR Optical Fiber Biosensors Based on Silver Nanoparticles. *Sensors* **2015,** *15*, 12205-12217.

(15) Alivisatos, A. P. Perspectives on the Physical Chemistry of Semiconductor Nanocrystals. *The J.*

Phy. Chem. **1996**, *100*, 13226-13239.

(16) Rabouw, F. T.; de Mello Donega, C. Excited-State Dynamics in Colloidal Semiconductor Nanocrystals. *Top. Curr. Chem.* **2016**, *374*, 58.

(17) Efros, A. L.; Brus, L. E. Nanocrystal Quantum Dots: From Discovery to Modern Development. *ACS Nano* **2021**, *15*, 6192-6210.

(18) Zielińska, A.; Carreiró, F.; Oliveira, A. M.; Neves, A.; Pires, B.; Venkatesh, D. N.; Durazzo, A.; Lucarini, M.; Eder, P.; Silva, A. M.; *et al*. Polymeric Nanoparticles: Production, Characterization, Toxicology and Ecotoxicology. *Molecules* **2020**, 25, 3731-3750.

(19) Crucho, C. I. C.; Barros, M. T. Polymeric Nanoparticles: A Study on The Preparation Variables and Characterization Methods. *Mater. Sci.Eng. C* **2017**, *80*, 771-784.

(20) Guterres, S. S.; Alves, M. P.; Pohlmann, A. R. Polymeric Nanoparticles, Nanospheres and Nanocapsules, for Cutaneous Applications. *Drug Target Insights* **2007**, *2,* 47-57.

(21) Schaffazick, S. R.; Pohlmann, A. R.; Dalla-Costa, T.; Guterres, S. l. S. Freeze-Drying Polymeric Colloidal Suspensions: Nanocapsules, Nanospheres and Nanodispersion. A comparative study. *Eur. J. Pharm.Biopharm.* **2003**, *56*, 501-505.

(22) Gagliardi, A.; Giuliano, E.; Venkateswararao, E.; Fresta, M.; Bulotta, S.; Awasthi, V.; Cosco, D. Biodegradable Polymeric Nanoparticles for Drug Delivery to Solid Tumors. *Front. Pharmacol.* **2021**, *12*, 601626.

(23) Pouran, H. M. Engineered Nanomaterials in the Environment, their Potential Fate and Behaviour and Emerging Techniques to Measure Them. In *Handbook of Environmental Materials Management*, Hussain, C. M. Ed.; Springer International Publishing, **2018**; pp 1-15.

(24) Agrawal, A.; Johns, R. W.; Milliron, D. J. Control of Localized Surface Plasmon Resonances in Metal Oxide Nanocrystals. *Annu. Rev. Mater. Res.* **2017**, *47*, 1-31.

(25) Bera, D.; Qian, L.; Tseng, T.-K.; Holloway, P. H. Quantum Dots and Their Multimodal Applications: A Review. *Materials* **2010,** *3*, 2260-2345.

(26) Akbarzadeh, A.; Samiei, M.; Davaran, S. Magnetic Nanoparticles: Preparation, Physical Properties, and Applications in Biomedicine. *Nanoscale Res Lett* **2012**, *7*, 144.

(27) Mehrmohammadi, M.; Yoon, K. Y.; Qu, M.; Johnston, K. P.; Emelianov, S. Y. Enhanced Pulsed Magneto-Motive Ultrasound Imaging Using Superparamagnetic Nanoclusters. *Nanotechnology* **2011**, *22*, 045502.

(28) Buffat, P.; Borel, J. P. Size Effect on The Melting Temperature of Gold Particles. *Phys. Rev. A* **1976**, *13*, 2287-2298.

(29) Chen, Y.; Thakar, R.; Snee, P. T. Imparting Nanoparticle Function with Size-Controlled Amphiphilic Polymers. *J. Am. Chem. Soc.* **2008**, *130*, 3744-3745.

(30) Wang, W.; Kapur, A.; Ji, X.; Safi, M.; Palui, G.; Palomo, V.; Dawson, P. E.; Mattoussi, H. Photoligation of an Amphiphilic Polymer with Mixed Coordination Provides Compact and

Reactive Quantum Dots. *J. Am. Chem. Soc.* **2015**, *137*, 5438-5451.

(31) Taniguchi, S.; Sandiford, L.; Cooper, M.; Rosca, E. V.; Ahmad Khanbeigi, R.; Fairclough, S. M.; Thanou, M.; Dailey, L. A.; Wohlleben, W.; von Vacano, B. Hydrophobin-Encapsulated Quantum Dots. *ACS Appl. Mater. Interfaces* **2016**, *8*, 4887-4893.

(32) Chen, Z.-L.; Lin, Y.; Yu, X.-J.; Zhu, D.-L.; Guo, S.-W.; Zhang, J.-J.; Wang, J.-J.; Wang, B.-S.; Zhang, Z.-L.; Pang, D.-W. Preparation of Monodisperse Hydrophilic Quantum Dots with Amphiphilic Polymers. *ACS Appl. Mater. Interfaces* **2017**, *9*, 39901-39906.

(33) Pellegrino, T.; Manna, L.; Kudera, S.; Liedl, T.; Koktysh, D.; Rogach, A. L.; Keller, S.; Rädler, J.; Natile, G.; Parak, W. J. Hydrophobic Nanocrystals Coated with an Amphiphilic Polymer Shell: A General Route to Water Soluble Nanocrystals. *Nano Lett.* **2004**, *4*, 703-707.

(34) Koole, R.; van Schooneveld, M. M.; Hilhorst, J.; de Mello Donegá, C.; Hart, D. C. '.; van Blaaderen, A.; Vanmaekelbergh, D.; Meijerink, A. On the Incorporation Mechanism of Hydrophobic Quantum Dots in Silica Spheres by a Reverse Microemulsion Method. *Chem. Mater.* **2008**, *20*, 2503-2512.

(35) Ma, Y.; Li, Y.; Ma, S.; Zhong, X. Highly Bright Water-Soluble Silica Coated Quantum Dots with Excellent Stability. *J. Mater. Chem. B* **2014**, *2*, 5043-5051.

(36) Nann, T.; Mulvaney, P. Single Quantum Dots in Spherical Silica Particles. *Angew. Chem. Int. Ed.* **2004**, *43*, 5393-5396.

(37) Stöber, W.; Fink, A.; Bohn, E. Controlled Growth of Monodisperse Silica Spheres in the Micron Size Range. *J. Colloid Interface Sci.* **1968**, *26*, 62-69.

(38) Jung, H.-S.; Kim, Y.-J.; Cho, J.; Yoon, T.-J.; Lee, J.-K. Silica-Coated Gradient Alloy Quantum Dots with High Luminescence for Converter Materials in White Light-Emitting Diodes. *RSC Adv.* **2015**, *5*, 107585-107590.

(39) Wang, N.; Koh, S.; Jeong, B. G.; Lee, D.; Kim, W. D.; Park, K.; Nam, M. K.; Lee, K.; Kim, Y.; Lee, B.-H.; *et al*. Highly Luminescent Silica-Coated CdS/CdSe/CdS Nanoparticles with Strong Chemical Robustness and Excellent Thermal Stability. *Nanotechnology* **2017**, *28*, 185603.

(40) Aubert, T.; Soenen, S. J.; Wassmuth, D.; Cirillo, M.; Van Deun, R.; Braeckmans, K.; Hens, Z. Bright and Stable CdSe/CdS@SiO_2 Nanoparticles Suitable for Long-Term Cell Labeling. *ACS Appl. Mater. Interfaces* **2014**, *6*, 11714-11723.

(41) Green, M. L. H. A New Approach to the Formal Classification of Covalent Compounds of the Elements. *J. Organomet. Chem.* **1995**, *500*, 127-148.

(42) Anderson, N. C.; Hendricks, M. P.; Choi, J. J.; Owen, J. S. Ligand Exchange and the Stoichiometry of Metal Chalcogenide Nanocrystals: Spectroscopic Observation of Facile Metal-Carboxylate Displacement and Binding. *J. Am. Chem. Soc.* **2013**, *135*, 18536-18548.

(43) Green, M. L. H.; Parkin, G. Application of the Covalent Bond Classification Method for the Teaching of Inorganic Chemistry. *J. Chem. Educ.* **2014**, *91*, 807-816.

(44) Kovalenko, M. V.; Scheele, M.; Talapin, D. V. Colloidal Nanocrystals with Molecular Metal Chalcogenide Surface Ligands. *Science* **2009**, *324*, 1417-1420.

(45) Ma, L.; Tu, C.; Le, P.; Chitoor, S.; Lim, S. J.; Zahid, M. U.; Teng, K. W.; Ge, P.; Selvin, P. R.; Smith, A. M. Multidentate Polymer Coatings for Compact and Homogeneous Quantum Dots with Efficient Bioconjugation. *J. Am. Chem. Soc.* **2016**, *138*, 3382-3394.

(46) Boles, M. A.; Ling, D.; Hyeon, T.; Talapin, D. V. The Surface Science of Nanocrystals. *Nat. Mater.* **2016**, *15*, 141-153.

(47) Hwang, D. S.; Zeng, H.; Masic, A.; Harrington, M. J.; Israelachvili, J. N.; Waite, J. H. Protein- and Metal-dependent Interactions of a Prominent Protein in Mussel Adhesive Plaques*. *J. Biol. Chem.* **2010**, *285*, 25850-25858.

(48) Wei, Q.; Achazi, K.; Liebe, H.; Schulz, A.; Noeske, P.-L. M.; Grunwald, I.; Haag, R. Mussel-Inspired Dendritic Polymers as Universal Multifunctional Coatings. *Angew. Chem. Int. Ed.* **2014**, *53*, 11650-11655.

(49) Lee, H.; Dellatore, S. M.; Miller, W. M.; Messersmith, P. B. Mussel-Inspired Surface Chemistry for Multifunctional Coatings. *Science* **2007**, *318*, 426-430.

(50) Hong, S.; Yeom, J.; Song, I. T.; Kang, S. M.; Lee, H.; Lee, H. Pyrogallol 2-Aminoethane: A Plant Flavonoid-Inspired Molecule for Material-Independent Surface Chemistry. *Adv. Mater. Interfaces* **2014**, *1*, 1400113.

(51) Ejima, H.; Richardson, J. J.; Liang, K.; Best, J. P.; van Koeverden, M. P.; Such, G. K.; Cui, J.; Caruso, F. One-Step Assembly of Coordination Complexes for Versatile Film and Particle Engineering. *Science* **2013**, *341*, 154-157.

(52) Sileika, T. S.; Barrett, D. G.; Zhang, R.; Lau, K. H. A.; Messersmith, P. B. Colorless Multifunctional Coatings Inspired by Polyphenols Found in Tea, Chocolate, and Wine. *Angew. Chem. Inter. Ed.* **2013**, *52*, 10766-10770.

(53) Abate, A. Specialty Grand Challenges in Optoelectronics. *Front. in Electron.* **2020**, *1*, 579890.

(54) Lee, H.; Jiang, Z.; Yokota, T.; Fukuda, K.; Park, S.; Someya, T. Stretchable Organic Optoelectronic Devices: Design of Materials, Structures, and Applications. *Mater. Sci. Eng. R* **2021**, *146*, 100631.

(55) Moon, H.; Chae, H. Efficiency Enhancement of All-Solution-Processed Inverted-Structure Green Quantum Dot Light-Emitting Diodes Via Partial Ligand Exchange with Thiophenol Derivatives Having Negative Dipole Moment. *Adv. Optical Mater.* **2020**, *8*, 1901314.

(56) Brown, P. R.; Kim, D.; Lunt, R. R.; Zhao, N.; Bawendi, M. G.; Grossman, J. C.; Bulović, V. Energy Level Modification in Lead Sulfide Quantum Dot Thin Films through Ligand Exchange. *ACS Nano* **2014**, *8*, 5863-5872.

(57) Song, J. H.; Choi, H.; Pham, H. T.; Jeong, S. Energy Level Tuned Indium Arsenide Colloidal Quantum Dot Films for Efficient Photovoltaics. *Nat. Commun.* **2018**, *9*, 4267.

(58) Yoon, S.-Y.; Lee, Y.-J.; Yang, H.; Jo, D.-Y.; Kim, H.-M.; Kim, Y.; Park, S. M.; Park, S.; Yang, H. Performance Enhancement of InP Quantum Dot Light-Emitting Diodes via a Surface-Functionalized ZnMgO Electron Transport Layer. *ACS Energy Lett.* **2022**, *7*, 2247-2255.

(59) Chen, F.; Lv, P.; Li, X.; Deng, Z.; Teng, F.; Tang, A. Highly-Efficient and All-Solution-Processed Red-Emitting InP/ZnS-Based Quantum-Dot Light-Emitting Diodes Enabled by Compositional Engineering of Electron Transport Layers. *J. Mater. Chem. C* **2019**, *7*, 7636-7642.

(60) Park, D.; Azmi, R.; Cho, Y.; Kim, H. M.; Jang, S.-Y.; Yim, S. Improved Passivation of PbS Quantum Dots for Solar Cells Using Triethylamine Hydroiodide. *ACS Sustain. Chem. Eng.* **2019**, *7*, 10784-10791.

(61) Bi, C.; Yao, Z.; Sun, X.; Wei, X.; Wang, J.; Tian, J. Perovskite Quantum Dots with Ultralow Trap Density by Acid Etching-Driven Ligand Exchange for High Luminance and Stable Pure-Blue Light-Emitting Diodes. *Adv. Mater.* **2021**, *33*, 2006722.

(62) Won, Y.-H.; Cho, O.; Kim, T.; Chung, D.-Y.; Kim, T.; Chung, H.; Jang, H.; Lee, J.; Kim, D.; Jang, E. Highly Efficient and Stable InP/ZnSe/ZnS Quantum Dot Light-Emitting Diodes. *Nature* **2019**, *575*, 634-638.

(63) Sun, L.; Choi, J. J.; Stachnik, D.; Bartnik, A. C.; Hyun, B.-R.; Malliaras, G. G.; Hanrath, T.; Wise, F. W. Bright Infrared Quantum-Dot Light-Emitting Diodes Through Inter-Dot Spacing Control. *Nat. Nanotechnol.* **2012**, *7*, 369-373.

(64) Lu, K.; Meng, X.; Liu, Z.; Chen, J.; Wang, Y.; Zhang, Y.; Zhang, X.; Sarnello, E.; Shi, G.; Patil, R. P.; *et al*. Packing State Management to Realize Dense and Semiconducting Lead Sulfide Nanocrystals Film via a Single-Step Deposition. *Cell Rep. Phy. Sci.* **2020**, *1*, 100183.

(65) Patil, N.; Jérôme, C.; Detrembleur, C. Recent Advances in The Synthesis of Catechol-Derived (Bio)Polymers for Applications in Energy Storage and Environment. *Prog. Polym. Sci.* **2018**, *82*, 34.

(66) Nam, H. J.; Kim, B.; Ko, M. J.; Jin, M.; Kim, J. M.; Jung, D.-Y. A New Mussel-Inspired Polydopamine Sensitizer for Dye-Sensitized Solar Cells: Controlled Synthesis and Charge Transfer. *Chem. Eur. J.* **2012**, *18*, 14000.

(67) Higashino, T.; Iiyama, H.; Kurumisawa, Y.; Imahori, H. Thiazolocatechol: Electron-Withdrawing Catechol Anchoring Group for Dye-Sensitized Solar Cells. *ChemPhysChem* **2019**, *20*, 2689.

(68) Ooyama, Y.; Yamada, T.; Fujita, T.; Harima, Y.; Ohshita, J. Development of D–π–Cat Fluorescent Dyes with A Catechol Group for Dye-Sensitized Solar Cells Based On Dye-to-TiO_2 Charge Transfer. *J. Mater. Chem. A* **2014**, *2*, 8500.

(69) Ooyama, Y.; Yamaji, K.; Ohshita, J. Photovoltaic Performances of Type-II Dye-Sensitized Solar Cells Based On Catechol Dye Sensitizers: Retardation of Back-Electron Transfer by PET (Photo-Induced Electron Transfer). *Mater. Chem. Front.* **2017**, *1*, 2243.

(70) Huang, P.; Liu, Y.; Zhang, K.; Yuan, L.; Li, D.; Hou, G.; Dong, B.; Zhou, Y.; Song, B.; Li, Y.

Catechol Derivatives as Dopants in PEDOT:PSS to Improve The Performance of p–i–n Perovskite Solar Cells. *J. Mater. Chem. A* **2017**, *5*, 24275.

(71) Xue, Q.; Liu, M.; Li, Z.; Yan, L.; Hu, Z.; Zhou, J.; Li, W.; Jiang, X.-F.; Xu, B.; Huang, F.; *et al*. Efficient and Stable Perovskite Solar Cells via Dual Functionalization of Dopamine Semiquinone Radical with Improved Trap Passivation Capabilities. *Adv. Funct. Mater.* **2018**, *28*, 1707444.

(72) Zeng, M.; Wang, X.; Ma, R.; Zhu, W.; Li, Y.; Chen, Z.; Zhou, J.; Li, W.; Liu, T.; He, Z.; *et al*. Dopamine Semiquinone Radical Doped PEDOT:PSS: Enhanced Conductivity, Work Function and Performance in Organic Solar Cells. *Adv. Energy Mater.* **2020**, *10*, 2000743.

(73) Hou, M.; Zhang, H.; Wang, Z.; Xia, Y.; Chen, Y.; Huang, W. Enhancing Efficiency and Stability of Perovskite Solar Cells via a Self-Assembled Dopamine Interfacial Layer. *ACS Appl. Mater. Interfaces* **2018**, *10*, 30607.

(74) Zhang, J.; Yu, H. Multifunctional Dopamine-Assisted Preparation of Efficient and Stable Perovskite Solar Cells. *J. Energy Chem.* **2021**, *54*, 291.

(75) Green, M. A.; Ho-Baillie, A.; Snaith, H. J. The Emergence of Perovskite Solar Cells. *Nat. Photonics* **2014**, *8*, 506.

(76) Dutta, A.; Behera, R. K.; Pal, P.; Baitalik, S.; Pradhan, N. Near-Unity Photoluminescence Quantum Efficiency for All $CsPbX_3$ (X=Cl, Br, and I) Perovskite Nanocrystals: A Generic Synthesis Approach. *Angew. Chem. Int. Ed.* **2019**, *58*, 5552.

(77) Protesescu, L.; Yakunin, S.; Bodnarchuk, M. I.; Krieg, F.; Caputo, R.; Hendon, C. H.; Yang, R. X.; Walsh, A.; Kovalenko, M. V. Nanocrystals of Cesium Lead Halide Perovskites ($CsPbX_3$, X = Cl, Br, and I): Novel Optoelectronic Materials Showing Bright Emission with Wide Color Gamut. *Nano Lett.* **2015**, *15*, 3692.

(78) Akkerman, Q. A.; D'Innocenzo, V.; Accornero, S.; Scarpellini, A.; Petrozza, A.; Prato, M.; Manna, L. Tuning the Optical Properties of Cesium Lead Halide Perovskite Nanocrystals by Anion Exchange Reactions. *J. Am. Chem. Soc.* **2015**, *137*, 10276.

(79) Song, T.-B.; Chen, Q.; Zhou, H.; Jiang, C.; Wang, H.-H.; Yang, Y.; Liu, Y.; You, J.; Yang, Y. Perovskite Solar Cells: Film Formation and Properties. *J. Mater. Chem. A* **2015**, *3*, 9032.

(80) Kovalenko, M. V.; Protesescu, L.; Bodnarchuk, M. I. Properties and Potential Optoelectronic Applications of Lead Halide Perovskite Nanocrystals. *Science* **2017**, *358*, 745.

(81) Dong, Y.; Wang, Y.-K.; Yuan, F.; Johnston, A.; Liu, Y.; Ma, D.; Choi, M.-J.; Chen, B.; Chekini, M.; Baek, S.-W.; *et al*. Bipolar-Shell Resurfacing for Blue LEDs Based on Strongly Confined Perovskite Quantum Dots. *Nat. Nanotechnol.* **2020**, *15*, 668.

(82) He, Z.; Zhong, C.; Su, S.; Xu, M.; Wu, H.; Cao, Y. Enhanced Power-Conversion Efficiency in Polymer Solar Cells Using an Inverted Device Structure. *Nat. Photonics* **2012**, *6*, 591.

(83) Wang, Y.-K.; Yuan, F.; Dong, Y.; Li, J.-Y.; Johnston, A.; Chen, B.; Saidaminov, M. I.; Zhou, C.; Zheng, X.; Hou, Y.; *et al*. All-Inorganic Quantum-Dot LEDs Based on a Phase-Stabilized α-

$CsPbI_3$ Perovskite. *Angew. Chem. Int. Ed.* **2021**, *60*, 16164.

(84) Tan, Z.-K.; Moghaddam, R. S.; Lai, M. L.; Docampo, P.; Higler, R.; Deschler, F.; Price, M.; Sadhanala, A.; Pazos, L. M.; Credgington, D.; *et al*. Bright Light-Emitting Diodes Based on Organometal Halide Perovskite. *Nat. Nanotechnol.* **2014**, *9*, 687.

(85) Xiao, Z.; Kerner, R. A.; Zhao, L.; Tran, N. L.; Lee, K. M.; Koh, T.-W.; Scholes, G. D.; Rand, B. P. Efficient Perovskite Light-Emitting Diodes Featuring Nanometre-Sized Crystallites. *Nat. Photonics* **2017**, *11*, 108.

(86) Lin, K.; Xing, J.; Quan, L. N.; de Arquer, F. P. G.; Gong, X.; Lu, J.; Xie, L.; Zhao, W.; Zhang, D.; Yan, C.; *et al*. Perovskite Light-Emitting Diodes with External Quantum Efficiency Exceeding 20 per cent. *Nature* **2018**, *562*, 245.

(87) Park, J. H.; Lee, A.-y.; Yu, J. C.; Nam, Y. S.; Choi, Y.; Park, J.; Song, M. H. Surface Ligand Engineering for Efficient Perovskite Nanocrystal-Based Light-Emitting Diodes. *ACS Appl. Mater. Interfaces* **2019**, *11*, 8428.

(88) Zheng, X.; Yuan, S.; Liu, J.; Yin, J.; Yuan, F.; Shen, W.-S.; Yao, K.; Wei, M.; Zhou, C.; Song, K.; *et al*. Chlorine Vacancy Passivation in Mixed Halide Perovskite Quantum Dots by Organic Pseudohalides Enables Efficient Rec. 2020 Blue Light-Emitting Diodes. *ACS Energy Lett.* **2020**, *5*, 793.

(89) Kim, Y.-H.; Kim, S.; Kakekhani, A.; Park, J.; Park, J.; Lee, Y.-H.; Xu, H.; Nagane, S.; Wexler, R. B.; Kim, D.-H.; *et al*. Comprehensive Defect Suppression in Perovskite Nanocrystals for High-Efficiency Light-Emitting Diodes. *Nat. Photonics* **2021**, *15*, 148.

Chapter 2.

Bio-Inspired Catecholamine-Derived Surface Modifier for Graphene-Based Organic Solar Cells

Chapter 2 is reprinted with permission from "*S. Jung†, H. Kim†, J. Lee†, G. Jeong, H. Kim, J. Park*, and H. Park*, ACS Appl. Energy Mater.* ***2018****, 1, 6463.*" Copyright 2018 American Chemical Society.

2.1 Introduction

Organic solar cells (OSCs) have recently drawn great attention as next-generation energy-harvesting devices, offering several advantageous features such as cost-effectiveness, light weight, flexibility, and compatibility for large-scale fabrication.[1–11] Indium tin oxide (ITO) has been widely used as a transparent conducting electrode (TCE) for OSCs owing to its high electrical conductivity and good optical transparency.[12] However, ITO is brittle and chemically unstable and the indium required is scarce, thus limiting the widespread use of ITO in next-generation devices.[13]

Graphene is a highly promising alternative material for TCEs owing to its outstanding electrical and optical properties, and capability for large-scale production.[14] Recent advancements with OSCs based on graphene electrodes have improved the device performance, reaching a power conversion efficiency (PCE) of over 8%.[15–19] The major barrier to the widespread implementation of graphene electrodes for this application is the non-uniform wetting of charge transporting materials on the graphene surface owing to the inherent hydrophobicity of graphene because of the inert nature of its sp^2 hybridized carbon structure.[18,20] Several strategies to resolve this issue have been proposed, including modifying the charge transporting materials with organic surfactants or polar solvents, chemically doping the graphene, or adding a metal oxide layer to the graphene.[21–24]

Dopamine is a small-molecule catecholamine that acts as a neurotransmitter in the synapses of the human neural system. Polymerized dopamine (pDA) has been utilized as an adhesive surface modifier to control the surface properties of various organic or inorganic materials, including polymers, semiconductors, and noble metals.[25] However, aggregation often occurs during the polymerization process, making the pDA surface rough with an uncontrollable morphology.[26]

Norepinephrine is another derivative of catecholamine that functions as a neurotransmitter and as a hormone associated with stress or danger. It is composed of a hydrophobic benzene ring and hydrophilic functional groups (Figure 2.1a). Unlike dopamine, polymerization of norepinephrine (pNE) can yield a relatively smooth thin film with a uniform surface morphology because its 3,4-

dihydroxybenzaldehyde unit suppresses the aggregation of pNE particles during the polymerization process.[26]

In this study, we fabricated graphene electrode-based OSCs by modifying the graphene surface through thin film coating of pNE as the surface modifier. Incubation time-dependent controllable pNE coating effectively modified the hydrophobic surface of graphene to make them hydrophilic without causing significant damage to the graphene. An annealing treatment on pNE-coated graphene improved the overall film quality and induced effective doping of graphene with negligible change in the chemical composition and optical transmittance of the resulting film. We then test the ability to apply a uniform poly(3,4-ethylenedioxythiophene)-poly(styrenesulfonate) (PEDOT:PSS) coating to this pNE-coated graphene surface as a hole transporting layer without any pinhole formation. By optimizing the incubation time for the pNE coating and the annealing condition, which was corroborated with various analyses on optical, electrical, and morphological properties, efficient graphene-based OSCs were demonstrated with PCE of 7.93%, achieving comparable performance to that of the ITO reference device (PCE=8.73%).

2.2 Results and discussion

The pNE film was formed on graphene via a catechol oxidative polymerization reaction using a pH-triggered dip-coating method as described previously.[25–28] Graphene was first synthesized by chemical vapor deposition (CVD) process and transferred to the target substrate.[29] The graphene was then immersed in a pH 8.5 Tris buffer (10 mM) containing norepinephrine and 2-(2-aminoethoxy)ethanol (AEE) (Figure 2.1b), which is a hydrophilic primary amine. It is worthwhile to point out that the addition of AEE is quite critical to achieve the high quality of pNE nanofilm on the graphene layer. AEE reagent plays two important roles in pNE coating as primary amine. One is a suppression of cohesion which is intermolecular crosslinking of catechol derivatives. It is well known that oxidized catechol reacts with primary amine by forming catechol-amine adducts via Schiff base formation or Michael addition reaction (Figure 2.1c). This process suppresses the uncontrollable polymerization of the catecholamine molecules, resulting in the formation of an ultra-smooth and conformal thin film of pNE. We compared the morphology of pNE-coated graphene with or without AEE and confirmed that the root-mean square (RMS) value decreased by 0.5 nm from 1.54 nm to 1.01 nm (Figure 2.2).

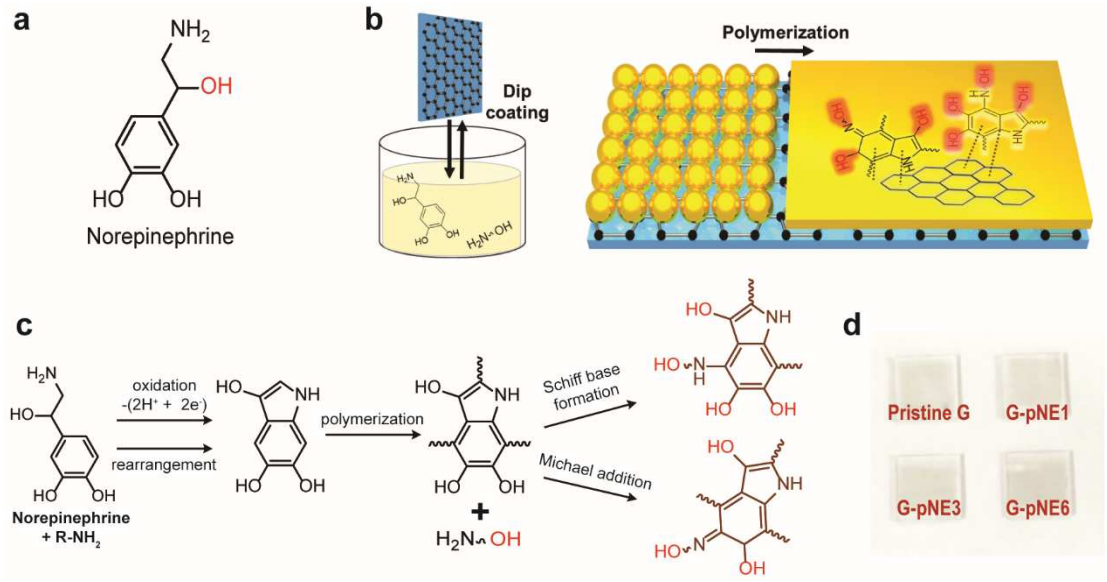

Figure 2.1. Formation of the pNE film on graphene. (a) Molecular structure of norepinephrine. (b) Schematic of the process of coating and polymerization of norepinephrine on graphene. (c) Scheme for the polymerization pathway of norepinephrine. (d) Digital image of pristine and pNE-coated graphene on glass substrates.

The other role of AEE is to provide more hydrophilicity to target surfaces. Because of the hydroxyl group in AEE molecule, catechol-adducts give an extra hydroxyl group to pNE coating layer. We

confirmed that the water contact angle decreased when AEE is added (Figure 2.3). The pNE coating via norepinephrine polymerization on graphene (G-pNE*x*, *x* = 1, 3, and 6 hr) did not significantly affect the optical transmittance, as observed in the digital images in Figure 2.1d. The transmittance of the pNE film that was formed with a 6 hr incubation time (G-pNE6) was over 96.0% at a wavelength of 550 nm, which was not significantly different from that of the pristine graphene sample (Figure 2.4).

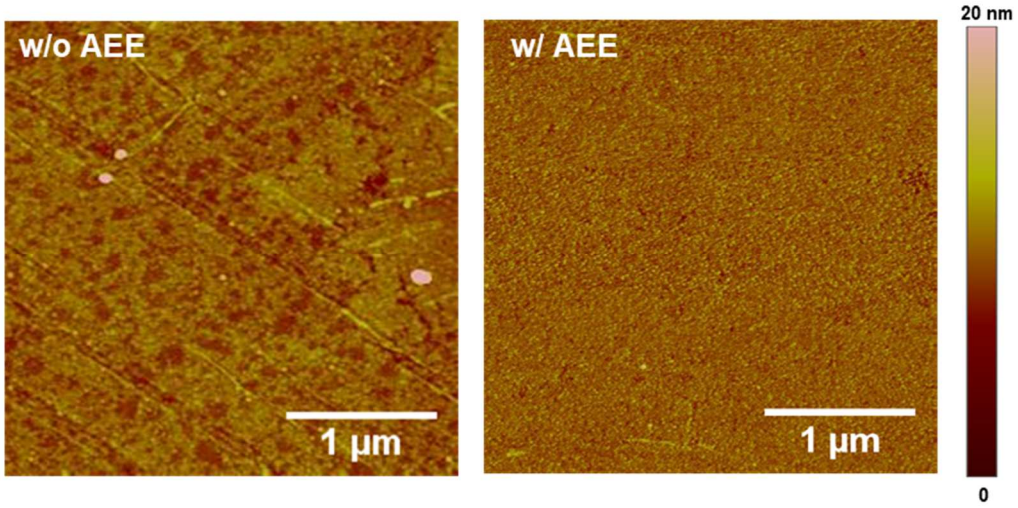

Figure 2.2. AFM images of pNE-coated graphene samples incubated for 6 h with and without AEE.

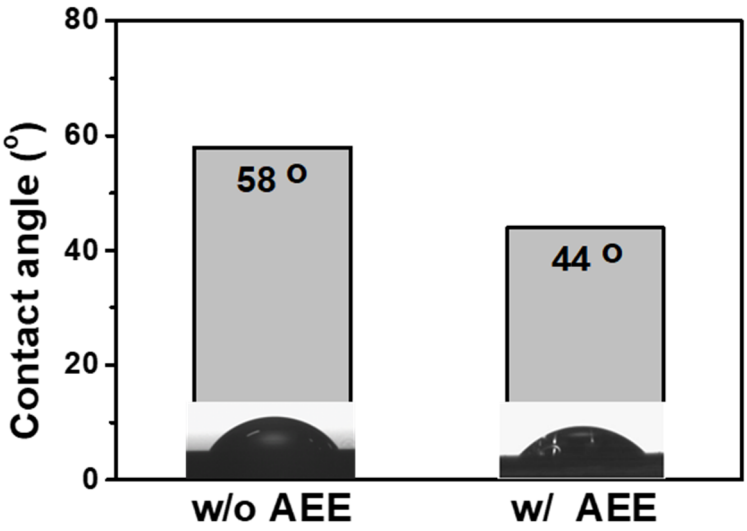

Figure 2.3. Water contact angles on pNE-coated graphene samples incubated for 6 h with and without AEE.

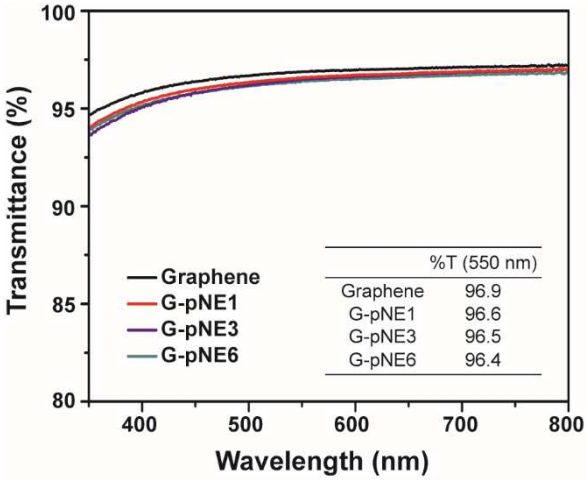

Figure 2.4. Optical transmittance of pNE-coated graphene films before annealing.

The surface morphologies of pNE films formed on graphene with various incubation times were analyzed by atomic force microscopy (AFM) as shown in Figure 2.5. The results show that the surface roughness of the pNE-coated graphene gradually increased as the polymerization of norepinephrine proceeds with increasing incubation time; the RMS roughness of pristine graphene was 0.4 nm while that of G-pNE6 was 1.0 nm (Figure 2.5a,b). The nanometer-scale thickness of the pNE film also increased proportionately with the incubation time as shown in Figure 2.5c. Compared with the pDA coating, the relatively slow polymerization rate of pNE promoted the formation of a smoother surface while minimizing the particle aggregation as evidenced by the scanning electron microscopy (SEM) images shown in Figure 2.6. This result further confirms that the proposed pNE-coating method enables the formation of a thin film with a low surface roughness with precise control over the film thickness.

To minimize the insulating effect of the pNE film,[30] a film thickness of less than 10 nm was used in this study. In addition, an annealing treatment was performed on the as-synthesized pNE film to improve the overall film quality. The treatment was found to enhance the electrical conductivity of the pNE-coated graphene without significantly affecting its chemical composition or optical properties. Figure 2.7 shows an AFM image of the annealed pNE film, showing the decreased surface roughness, thickness and the absence of aggregation. The reduction of the film roughness and thickness indicates that the number of vacant spaces between pNE particles was decreased during annealing process.

Next, X-ray photoelectron spectroscopy (XPS) was carried out to characterize the effects of the thermal treatment on the chemical composition of the pNE film. Figure 2.8 shows the XPS spectra of the C 1s and N 1s peaks in pNE-coated graphene, indicating that the annealing process resulted in negligible changes.[30] Figure 2.9 shows the sheet resistance of the pNE-coated graphene film, which indicates that the electrical conductivity decreased as the pNE incubation time increased owing to the pNE-induced insulation effect and the interfacial contact resistance between pNE and graphene. The annealing treatment improved the overall conductivity of the film by reducing the vacant spaces and

improving the contact between the graphene and pNE. Moreover, the optical transmittance analysis showed that the annealing process did not cause a significant change in the pNE film as shown in Figure 2.10.

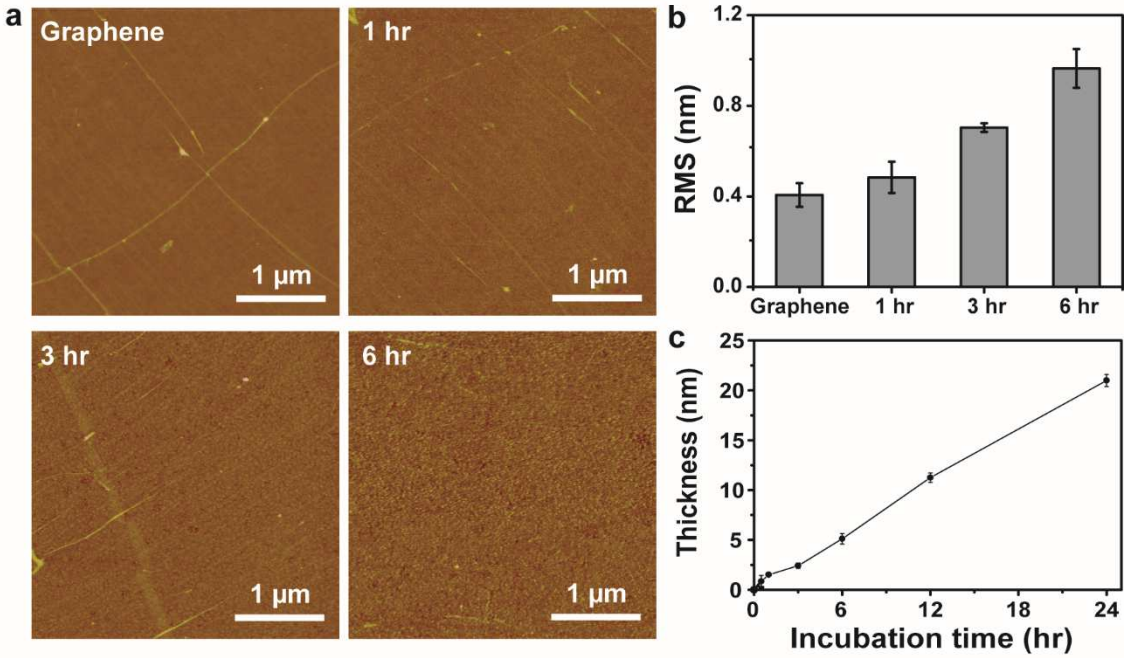

Figure 2.5. Surface morphology analysis of pristine and pNE-coated graphene without annealing. (a) Topography images of pristine graphene and pNE-coated graphene formed with various incubation times. (b) RMS values representing the roughness of graphene and pNE-coated graphene. (c) Thickness of the pNE film as a function of the incubation time.

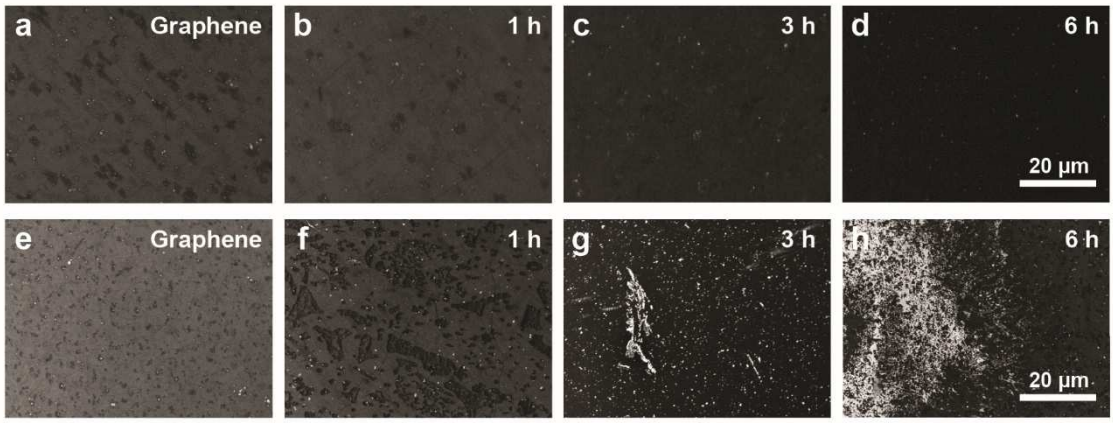

Figure 2.6. SEM images of (a–d) pNE-coated graphene and (e–h) pDA-coated graphene according to incubation time.

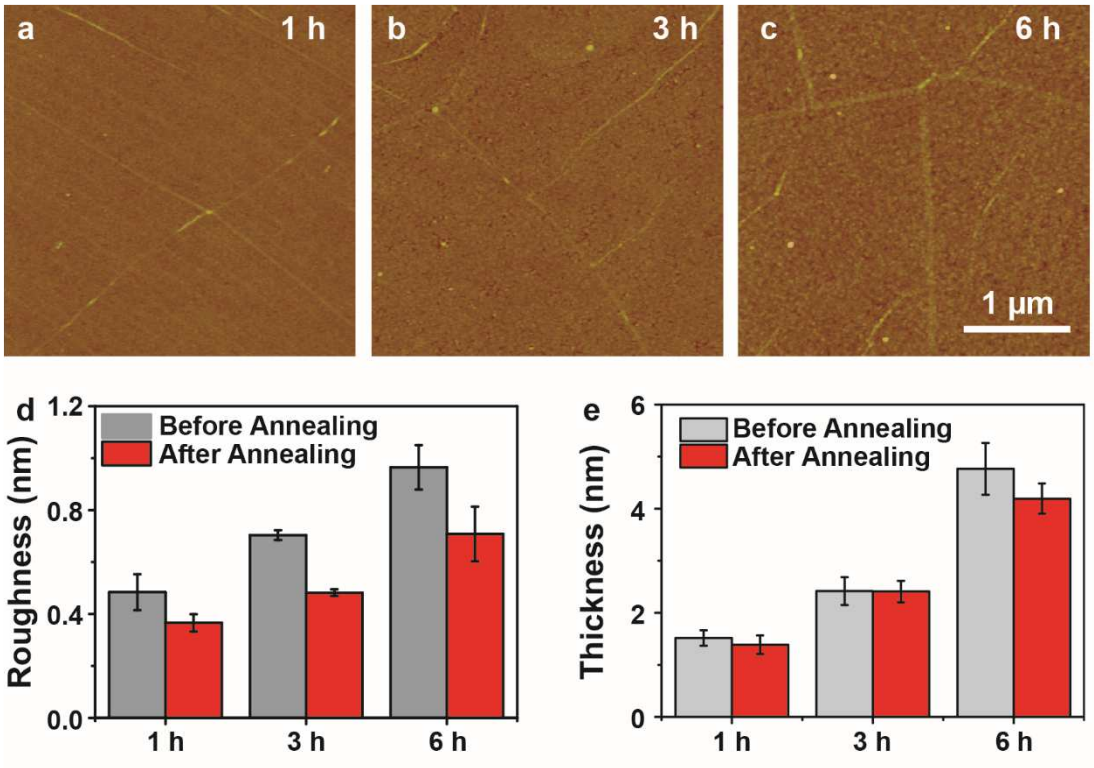

Figure 2.7. (a–c) AFM images of pNE-coated graphene after annealing with different incubation time. Comparison of (d) root mean square values and (e) thicknesses of pNE-coated graphene before and after annealing.

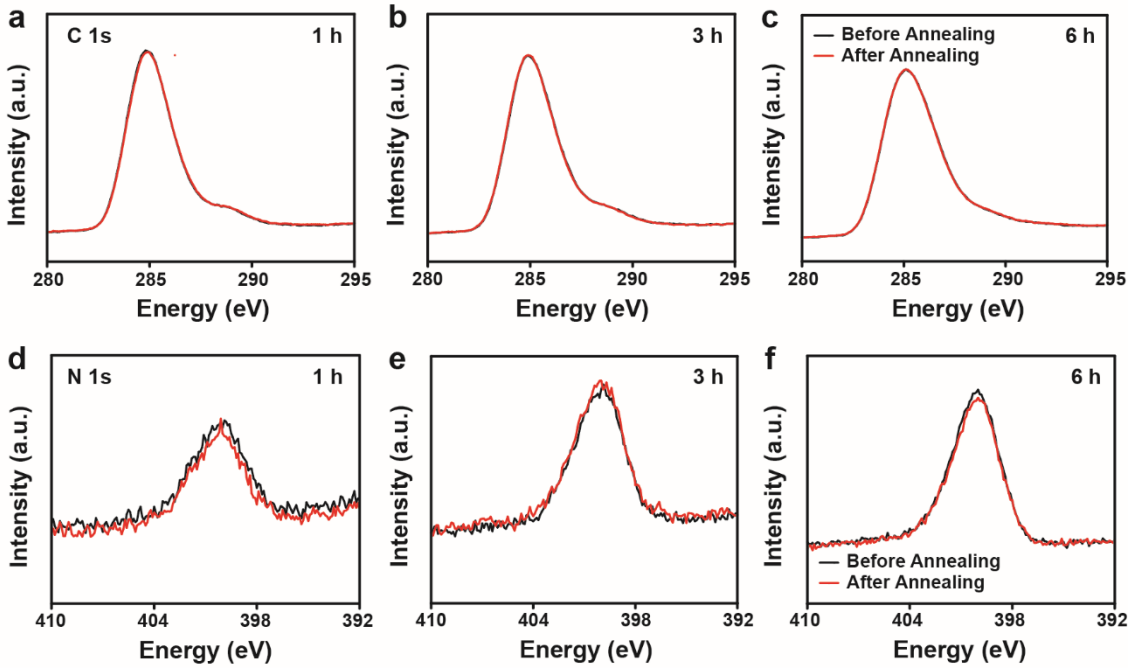

Figure 2.8. XPS spectra of (a–c) C 1s and (d–f) N 1s peaks of pNE-coated graphene before and after annealing.

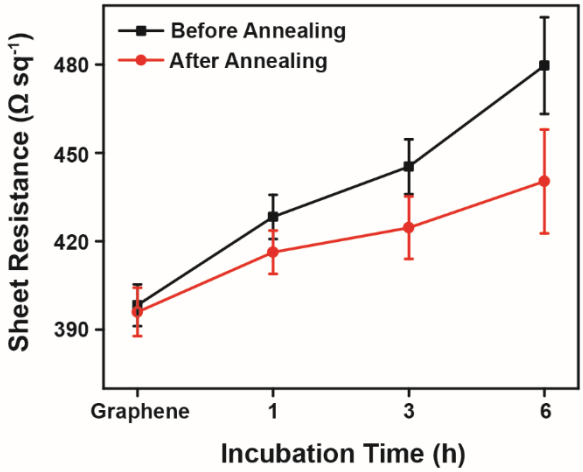

Figure 2.9. Sheet resistance of pNE-coated graphene films before and after annealing according to incubation time.

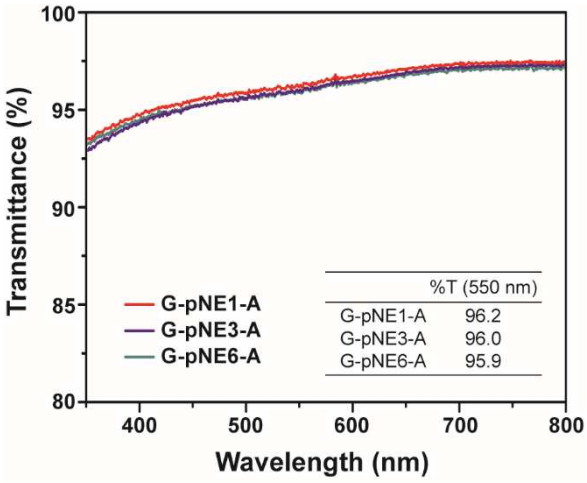

Figure 2.10. Optical transmittance of pNE-coated graphene films after annealing.

The effect of the pNE coating on graphene was further characterized via several spectroscopic analyses. Raman spectroscopy was carried out to identify any structural damage to the sp^2 carbon framework of graphene as a result of the pNE polymerization process. A disorder-induced D peak (1350 cm^{-1}), which originates from the back-scattered phonon by the defect structures in graphene, indicates any disruption of graphene lattice symmetry, including sp^3 carbon defects, vacancy sites, and grain boundaries.[31] The shaded region in the spectra in Figure 2.11a represents the defect spectra of graphene. Negligible defect peak in the pristine graphene indicates that high-quality graphene was synthesized and transferred to the substrate. No noticeable changes in the D peaks were observed after the 1, 3, and 6 hr-incubated pNE coating on graphene, indicating that the pNE coating does not cause any significant damage to the graphene lattice structure. Furthermore, the change in the intensity ratio of G (1560 cm^{-1})

to 2D peaks (2680 cm^{-1}), as well as the peak shift, suggests that graphene is p-doped through the pNE coating,[32,33] which becomes more pronounced with increasing pNE thickness (Table 2.1).

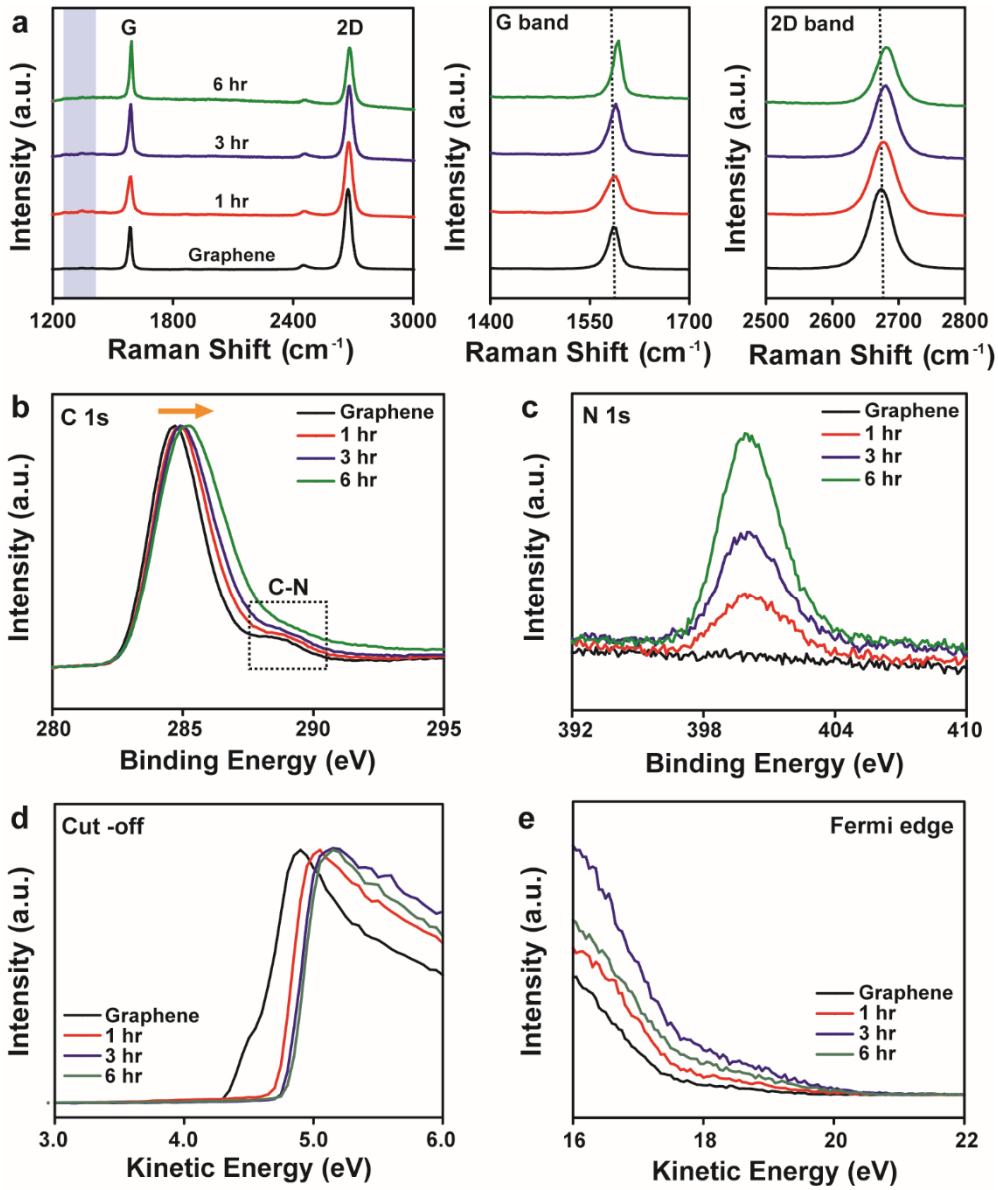

Figure 2.11. Spectroscopic analyses of graphene and pNE-coated graphene without annealing. (a) Raman spectra of graphene and pNE-coated graphene (the purple shaded region indicates the defect-related peak). Zoom-in regions of the Raman spectra at right confirm the presence of p-doped graphene. XPS spectra of the (b) C 1s and (c) N 1s peaks showing the peak shift due to the pNE coating on the graphene surface. UPS spectra of the (d) cut-off and (e) Fermi edge regions for graphene and pNE-coated graphene.

Table 2.1. The intensity ratio of G/2D peak in Figure 2.11a.

	Graphene	G-pNE1	G-pNE3	G-pNE6
G/2D	0.63	0.78	0.99	1.02

XPS analysis was performed to characterize the chemical composition of the pNE-coated graphene. As shown in Figure 2.11b, the XPS spectra of C 1s peak broadened as the incubation time with pNE increased; this was due to the increase in the intensity of the sp^3 carbon peak at 286 eV, which is associated with the carbon backbone of pNE.[34] The observed C 1s peak shift to higher binding energies corresponds to the p-doping of graphene.[35,36] The region delineated by the dotted line represents the C−N bond (289 eV),[35] and the increase in the associated peak intensity indicates the thickening of the pNE film as the incubation time increased. Similarly, the intensity of the N 1s peak at a binding energy of 400 eV increased as the pNE incubation time increased as shown in Figure 2.11c.

Then, ultraviolet photoelectron spectroscopy (UPS) was performed to confirm the change of graphene work function due to the doping effect.[36] As seen in the cut-off region in Figure 2.11d, the graphene coated with pNE exhibited higher work function values (4.8 eV in the G-pNE6) than pristine graphene (4.4 eV). This finding is consistent with the Raman and XPS results. The pNE coating did not cause any significant differences in the Fermi edge of the UPS spectrum, as shown in Figure 2.11e.

The wettability of the PEDOT:PSS on pristine graphene and pNE-coated graphene was evaluated by contact angle measurement and SEM analysis. As shown in Figure 2.12a, the water contact angle on pristine graphene was 86º, confirming the hydrophobic nature of pristine graphene surface.[18] After the pNE coating on graphene with a 1 hr incubation time, the contact angle was reduced to 60º, indicating that the surface of graphene was modified to become more hydrophilic. The contact angle was further reduced with thicker pNE layer, which eventually was saturated after 3 hr of incubation time. PEDOT:PSS was coated onto the hydrophilic-modified graphene and the surface morphology of the associated film was analyzed through SEM shown in Figure 2.12b−e. In contrast to the incomplete PEDOT:PSS coating on pristine hydrophobic graphene, uniform coverage was achieved on the surface-modified graphene without any pinholes regardless of the pNE thickness, confirming that the pNE coating promotes uniform PEDOT:PSS formation on graphene surface.

pNE-coated graphene electrode-based OSCs were fabricated with the conventional structure using poly[4,8-bis(5-(2-ethylhexyl)thiophen-2-yl)benzo[1,2-*b*;4,5-*b'*]dithiophene-2,6-diyl-*alt*-(4-(2-ethylhexyl)-(3-fluorothieno[3,4-*b*]thiophene-)-2-carboxylate-2,6-diyl)] (PTB7-Th) and [6,6]-phenyl-C_{71}-butyric acid methyl ester ($PC_{71}BM$) as the donor and acceptor materials, respectively, for the bulk heterojunction photoactive layer. A schematic of the device structure and the corresponding flat-band energy-level diagram are provided in Figure 2.13a. Three layer of stacked CVD-grown graphene with an average sheet resistance of 318.6 ± 8 Ω sq^{-1} and transmittance of 92.6% at 550 nm, was used as the

TCE to optimize the device performance. The fabrication details are provided in Methods. The current density versus voltage (J−V) characteristics of OSCs were measured under simulated AM 1.5G illumination at 100 mW cm^{-2} irradiance. As shown in Figure 2.13b, the overall device performance was slightly better for the annealed pNE-graphene OSCs (G-pNEx-A, x = 1, 3, and 6 hr) compared to the non-annealed pNE-graphene devices. Figure 2.13c is the summary of device performance statistics for 1 hr pNE-coated graphene-based OSCs, which exhibits higher device yield in overall for the annealed case. The corresponding photovoltaic parameters are summarized in Table 2.2. As shown in Figure 2.13d, the optimized pNE-coated graphene-based PTB7-Th:$PC_{71}BM$ champion device exhibited a PCE of 7.93% with a short-circuit current density (J_{sc}) of 15.89 mA cm^{-2}, an open-circuit voltage (V_{oc}) of 0.80 V, and a fill factor (FF) of 62%, reaching close to the performance of ITO reference device (PCE=8.73%). The slightly lower J_{sc} and FF values of the graphene-based devices were mainly attributed to the high sheet resistance of graphene compared to ITO. External quantum efficiency (EQE) measurements also confirmed the lower J_{sc} vales of the graphene-based OSCs compared to the ITO-based devices as shown in Figure 2.13e. These results demonstrate that hydrophilic surface modification of graphene by well-controlled pNE coating with negligible loss in optical and electrical properties could be successfully integrated in optoelectronic devices.

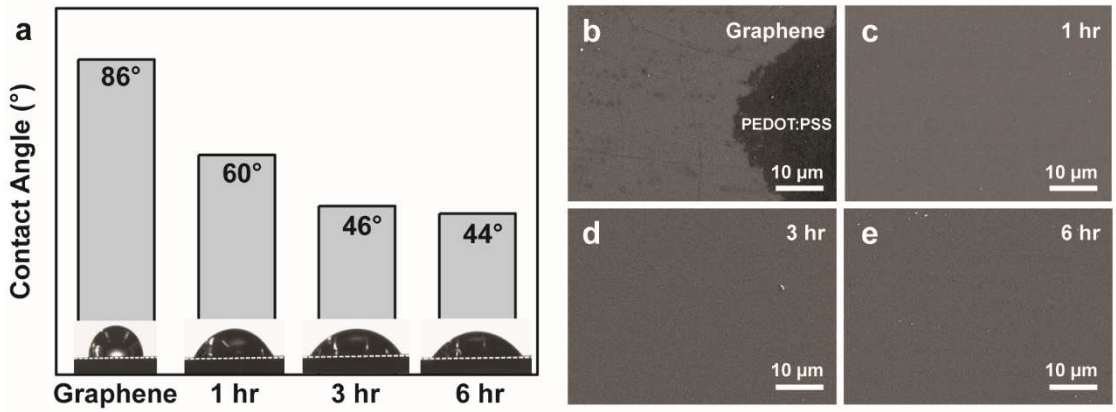

Figure 2.12. Surface modification of graphene by the pNE coating without annealing. (a) Water contact angles on pristine graphene and pNE-coated graphene samples incubated for 1, 3, and 6 hr. SEM images of the PEDOT:PSS coatings on (b) a pristine graphene surface and (c−e) pNE-coated graphene with various incubation times.

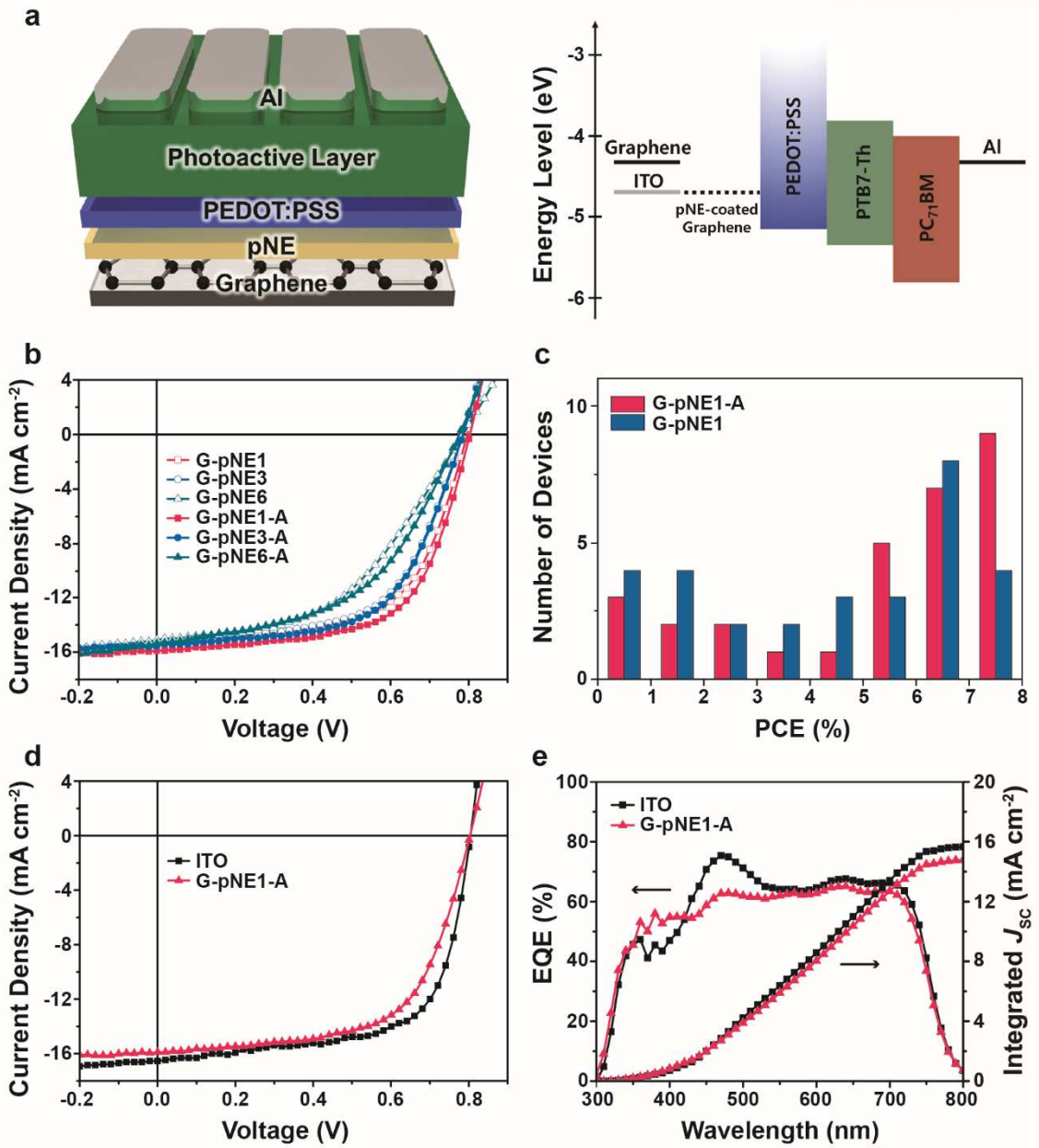

Figure 2.13. Device performance of the pNE-coated graphene-based OSCs. (a) Schematic of the conventional device and the corresponding flat-band energy-level diagram. (b) *J*–*V* characteristics of the pNE-coated graphene-based OSCs with and without the annealing treatment. (c) Performance statistics for the OSCs with G-pNE1 with and without annealing. (d) *J*–*V* characteristics and (e) EQE measurements with corresponding integrated J_{sc} of the device with the best performance (G-pNE1-A) compared with those of the ITO reference.

Table 2.2. Device performance parameters of ITO- and graphene-based PTB7-Th:PC71BM OSCs[a]

Anode	J_{sc} [mA cm^{-2}]	V_{oc} [V]	FF [%]	PCE [%]	R_s [Ω cm^2]	R_{sh} [Ω cm^2]
ITO	16.54 (16.33 ± 0.21)	0.80 (0.79 ± 0.01)	65.7 (65.2 ± 0.5)	8.73 (8.41 ± 0.32)	20	1854
G-pNE1	15.46 (15.01 ± 0.45)	0.80 (0.78 ± 0.02)	60.0 (57.6 ± 2.4)	7.39 (6.74 ± 0.65)	202	12200
G-pNE3	15.36 (14.87 ± 0.49)	0.78 (0.74 ± 0.04)	58.8 (54.3 ± 4.5)	7.08 (5.98 ± 1.10)	251	8820
G-pNE6	15.11 (14.46 ± 0.65)	0.79 (0.74 ± 0.05)	48.1 (39.7 ± 8.4)	5.69 (4.25 ± 1.44)	496	16621
G-pNE1-A	15.89 (15.64 ± 0.25)	0.80 (0.79 ± 0.01)	62.1 (61.0 ± 1.1)	7.93 (7.54 ± 0.39)	188	16715
G-pNE3-A	15.56 (15.19 ± 0.37)	0.79 (0.77 ± 0.02)	59.6 (57.8 ± 1.8)	7.26 (6.76 ± 0.50)	261	16223
G-pNE6-A	15.34 (14.72 ± 0.62)	0.78 (0.73 ± 0.05)	50.2 (47.8 ± 2.4)	5.97 (5.12 ± 0.85)	384	10100

[a] The average values were calculated from 30 devices.

2.3 Conclusion

In this study, norepinephrine, a bio-inspired catecholamine derivative with adhesive properties, was utilized as the surface modifier of graphene electrodes for applications in OSCs. The formation of a uniform pNE thin film via the polymerization of norepinephrine modified the intrinsically hydrophobic graphene surface more hydrophilic. This surface modification enabled uniform coverage of a conventional hole transporting material without any pinhole formation. As a result, highly efficient graphene-based OSCs were successfully demonstrated with comparable performance to the ITO reference device. The morphology and thickness controllable pNE coating without significant deterioration of the chemical or electrical properties of the electrode make it promising for applications in various graphene-based optoelectronic devices based on solution-processing or printing technologies.

2.4 Experimental section

Graphene synthesis and pNE coating. Graphene was synthesized by CVD method using Cu substrate (Alfa Aesar, 13382) at low pressure condition. CVD furnace was ramped to 1000 °C under hydrogen flow. After annealing at 1000 °C, the graphene was grown by introducing the methane gas. The as-synthesized graphene was transferred to target substrate through polymer-assisted wet transfer method using poly(methyl methacrylate). The pNE film was formed by simple dip coating method. The coating solution contains 9.73 mM of DL-norepinephrine hydrochloride (Sigma-Aldrich, A7256) and 9.73 mM of 2-(2-aminoethoxy)ethanol (Sigma-Aldrich, A54059) in Tris buffer (10 mM, pH 8.5). The transferred graphene was immersed in the coating solution and incubated for various time durations. The coated substrate was taken out carefully with argon blowing. Non-coated materials were washed out by stream of distilled water, followed by gentle blow-drying with Ar.

Device Fabrication. ITO-coated glass substrates were cleaned by sonication in soap water, deionized water, acetone, and isopropanol followed by oxygen plasma treatment. PEDOT:PSS was spin-coated on ITO or pNE-coated graphene electrodes at 4000 rpm for 1 min. In case of annealing samples (G-pNEx-A, x=1, 3, 6 hr), pNE films were treated at 100 ºC for 1 hour with 300 sccm of Ar before PEDOT:PSS coating. PTB7-Th and $PC_{71}BM$ were dissolved in a mixture of chlorobenzene:1,8-diiodooctane (97:3 vol%) solvents at concentrations of 12 and 40 mg mL^{-1}, respectively. The blended solution of PTB7-Th:$PC_{71}BM$ was spin-coated at 900 rpm for 2 min under nitrogen environment. Al was thermally evaporated under high vacuum conditions at base pressure of 8×10^{-7} Torr.

Measurements and Characterization. *J*−*V* characteristics of solar cells were measured using a Xenon arc lamp (300 W) solar simulator and Keithley 2635A source measurement unit in a nitrogen-filled glove box. A custom-made shadow mask was used during the measurement to prevent any potential overestimation over the actual device area. EQE measurements were performed using the QE system (QEX7, PV measurements) under ambient conditions. The analysis on the surface morphology was performed using dimension AFM (DI-3100, Veeco) operating in tapping mode, SEM (S-4800, Hitach), and OM (Eclipse LV150, Nikon). XPS and UPS measurements were conducted using monochromated Al−Kα radiation source and He I (21.2 eV) discharge lamp (ESCALAB 250Xi, Thermo Fisher Scientific), respectively, under ultra-high vacuum condition (<10^{-10} Torr). XRD patterns were registered using a Cu X-ray source (MAX2500V, Rigaku). Raman spectra were recorded by confocal Raman microscope (Alpha300R, WITec). Absorption and transmittance spectra were measured by UV−Vis−NIR spectrophotometer (Cary 5000, Agilent). Sheet resistance was measured by 4-point probe (CMT-SR2000N, Advanced Instrument Technology).

2.5 References

(1) Scharber, M. C.; Mühlbacher, D.; Koppe, M.; Denk, P.; Waldauf, C.; Heeger, A. J.; Brabec, C. J. Design Rules for Donors in Bulk-Heterojunction Solar Cells—Towards 10 % Energy-Conversion Efficiency. *Adv. Mater.* **2006**, *18*, 789−794.

(2) Kaltenbrunner, M.; White, M. S.; Głowacki, E. D.; Sekitani, T.; Someya, T.; Sariciftci, N. S.; Bauer, S. Ultrathin and Lightweight Organic Solar Cells with High Flexibility. *Nat. Commun.* **2011**, *3*, 770.

(3) He, Z.; Zhong, C.; Su, S.; Xu, M.; Wu, H.; Cao, Y. Enhanced Power-Conversion Efficiency in Polymer Solar Cells Using an Inverted Device Structure. *Nat. Photonics* **2012**, *6*, 591−595.

(4) Chen, K.-S.; Salinas, J.-F.; Yip, H.-L.; Huo, L.; Hou, J.; Jen, A. K.-Y. Semi-Transparent Polymer Solar Cells with 6% PCE, 25% Average Visible Transmittance and a Color Rendering Index Close to 100 for Power Generating Window Applications. *Energy Environ. Sci.* **2012**, *5*, 9551−9557.

(5) Che, C.-C.; Dou, L.; Zhu, R.; Chung, C.-H.; Song, T.-B.; Zheng, Y. B.; Hawks, S.; Li, G.; Weiss, P. S.; Yang, Y. Visibly Transparent Polymer Solar Cells Produced by Solution Processing. *ACS Nano* **2012**, *6*, 7185−7190.

(6) Lin, Y.; Wang, J.; Zhang, Z.-G.; Bai, H.; Li, Y.; Zhu, D.; Zhan, X. An Electron Acceptor Challenging Fullerenes for Efficient Polymer Solar Cells. *Adv. Mater.* **2015**, *27*, 1170−1174.

(7) Zhao, J.; Li, Y.; Yang, G.; Jiang, K.; Lin, H.; Ade, H.; Ma, W.; Yan, H. Efficient Organic Solar Cells Processed from Hydrocarbon Solvents. *Nat. Energy* **2016**, *1*, 15027.

(8) Chen, S.; Lee, S. M.; Xu, J.; Lee, J.; Lee, K. C.; Hou, T.; Yang, Y.; Jeong, M.; Lee, B.; Cho, Y.; Jung, S.; Oh, J.; Zhang, Z.-G.; Zhang, C.; Xiao, M.; Li, Y.; Yang, C. Ultrafast Channel II process induced by a 3-D texture with enhanced acceptor order ranges for high-performance non-fullerene polymer solar cells. *Energy Environ. Sci.* **2018**, *11*, 2569−2580.

(9) Lee, S. M.; Park, K. H.; Jung, S.; Park, H.; Yang, C. Stepwise heating in Stille polycondensation toward no batch-to-batch variations in polymer solar cell performance. *Nat. Commun.* **2018**, *9*, 1867.

(10) Kumari, T.; Lee, S. M.; Yang, C. Cubic-Like Bimolecular Crystal Evolution and over 12% Efficiency in Halogen-Free Ternary Solar Cells. *Adv. Funct. Mater.* **2018**, *28*, 1707278.

(11) Kang, S.-H.; Kumari, T.; Lee, S. M.; Jeong, M.; Yang, C. Densely Packed Random Quarterpolymers Containing Two Donor and Two Acceptor Units: Controlling Absorption Ability and Molecular Interaction to Enable Enhanced Polymer Photovoltaic Devices. *Adv. Energy Mater.* **2017**, *7*, 1700349.

(12) Schmidt, H.; Flügge, H.; Winkler, T.; Bülow, T.; Riedl, T.; Kowalsky, W. Efficient Semitransparent Inverted Organic Solar Cells with Indium Tin Oxide Top Electrode. *Appl. Phys. Lett.* **2009**, *94*, 243302.

(13) Ramuz, M. P; Vosgueritchian, M.; Wei, P.; Wang, C.; Gao, Y.; Wu, Y.; Chen, Y.; Bao, Z. Evaluation of Solution-Processable Carbon-Based Electrodes for All-Carbon Solar Cells. *ACS Nano* **2011**, *6*, 10384−10395.

(14) Bae, S.; Kim, H.; Lee, Y.; Xu, X.; Park, J.; Zheng, Y.; Balakrishnan, J.; Lei, T.; Kim, H. R.; Song, Y. I.; Kim, Y.; Kim, K. S.; Özyilmaz, B.; Ahn, J.; Hong B. H.; Iijima, S. Roll-to-Roll Production of 30-inch Graphene Films for Transparent Electrodes. *Nat. Nanotechnol.* **2010**, *5*, 574−578.

(15) Park, H.; Chang, S.; Zhou, X.; Kong, J.; Palacios, T.; Gradečak, S. Flexible Graphene Electrode-Based Organic Photovoltaics with Record-High Efficiency. *Nano Lett.* **2014**, *14*, 5148−5154.

(16) Liu, Z.; Yan, F.; Liu, S.; Yan, F. Neutral-Color Semitransparent Organic Solar Cells with All-Graphene Electrodes. *ACS Nano* **2015**, *9*, 12026−12034.

(17) Kim, H.; Byun, J.; Bae, S.-H.; Ahmed, T.; Zhu, J.-X.; Kwon, S.-J.; Lee, Y.; Min, S.-Y.; Wolf, C.; Seo, H.-K.; Ahn, J.-H.; Lee, T.-W. On-Fabrication Solid-State N-Doping of Graphene by an Electron-Transporting Metal Oxide Layer for Efficient Inverted Organic Solar Cells. *Adv. Energy Mater.* **2016**, *6*, 1600172.

(18) Jung, S.; Lee, J.; Choi, Y.; Lee, S. M.; Yang, C.; Park, H. Improved Interface Control for High-Performance Graphene-Based Organic Solar Cells. *2D Mater.* **2017**, *4*, 045004.

(19) Jung, S.; Lee, J.; Seo, J.; Kim, U. Choi, Y.; Park, H. Development of Annealing-Free, Solution-Processable Inverted Organic Solar Cells with N-Doped Graphene Electrodes using Zinc Oxide Nanoparticles. *Nano Lett.* **2018**, *18*, 1337−1343.

(20) Li, Z.; Wang, Y.; Kozbial, A.; Shenoy, G.; Zhou, F.; McGinley, R.; Ireland, P.; Morganstein, B.; Kunkel, A.; Surwade, S. P.; Li, L.; Liu H. Effect of Airborne Contaminants on the Wettability of Supported Graphene and Graphite. *Nat. Mater.* **2013**, *12*, 925−931

(21) Wang, Y.; Chen, X.; Zhong, Y.; Zhu, F.; Loh, K. P. Large Area, Continuous, Few-Layered Graphene as Anodes in Organic Photovoltaic Devices. *Appl. Phys. Lett.* **2009**, *95*, 063302.

(22) Park, H.; Shi, Y.; Kong, J.; Application of Solvent Modified PEDOT:PSS to Graphene Electrodes in Organic Solar Cells. *Nanoscale* **2013**, *5*, 8934−8939.

(23) Kim, K.; Bae, S.; Toh, C. T.; Kim, H.; Cho, J. H.; Whang, D.; Lee T.; Özyilmaz, B.; Ahn J. Ultrathin Organic Solar Cells with Graphene Doped by Ferroelectric Polarization. *ACS Appl. Mater. Interfaces* **2014**, *6*, 3299−3304.

(24) Kim, H.; Bae, S.; Han, T.; Lim, K.; Ahn, J.; Lee, T. Organic Solar Cells Using CVD-Grown Graphene Electrodes. *Nanotechnology* **2014**, *25*, 014012.

(25) Lee, H.; Dellatore, S. M.; Miller, W. M.; Messersmith, P. B. Mussel-Inspired Surface Chemistry for Multifunctional Coatings. *Science* **2007**, *318*, 426−430.

(26) Hong, S.; Kim, J.; Na, Y. S.; Park, J.; Kim S.; Singha, K.; Im, G.-I.; Han, D.-K.; Kim, W. J.; Lee, H. Poly(norepinephrine): Ultrasmooth Material-Independent Surface Chemistry and Nanodepot for Nitric Oxide. *Angew. Chem. Int. Ed.* **2013**, *52*, 9187−9191.

(27) Hong, S.; Yeom, J.; Song, I. T.; Kang, S. M.; Lee, H.; Lee, H. Pyrogallol 2-Aminoethane: A Plant Flavonoid-Inspired Molecule for Material-Independent Surface Chemistry. *Adv. Mater. Interfaces* **2014**, *1*, 1400113.

(28) Wu, J.; Zhang, L.; Wang, Y.; Long, Y.; Gao, H.; Zhang, X.; Zhao, N.; Cai, Y.; Xu, J. Mussel-Inspired Chemistry for Robust and Surface-Modifiable Multilayer Films. *Langmuir* **2011**, *27*, 13684−13691.

(29) Park, H.; Brown, P. R.; Bulović, V.; Kong, J. Graphene As Transparent Conducting Electrodes in Organic Photovoltaics: Studies in Graphene Morphology, Hole Transporting Layers, and Counter Electrodes. *Nano Lett.* **2012**, *1*, 133−140.

(30) Ryu, S.; Chou, J. B.; Lee, K.; Lee, D.; Hong, S. H.; Zhao, R.; Lee, H.; Kim, S. Direct Insulation-to-Conduction Transformation of Adhesive Catecholamine for Simultaneous Increases of Electrical Conductivity and Mechanical Strength of CNT Fibers. *Adv. Mater.* **2015**, *27*, 3250−3255.

(31) Beams, R.; Cançado, L. G.; Novotny, L. Raman Characterization of Defects and Dopants in Graphene. *J. Phys.: Condens. Matter* **2015**, *27*, 083002.

(32) Choi, Y.; Lee, J.; Seo, J.; Jung, S.; Kim, U.; Park, H. The Effect of the Graphene Integration Process on the Performance of Graphene-Based Schottky Junction Solar Cells. *J. Mater. Chem. A* **2017**, *5*, 18716−18724.

(33) Ferrari, A.C. Raman Spectroscopy of Graphene and Graphite: Disorder, Electron–Phonon Coupling, Doping and Nonadiabatic Effects. *Solid State Commun.* **2007**, *143*, 47−57.

(34) Dwivedi, N.; Yeo, R. J.; Satyanarayana, N.; Kundu, S.; Tripathy, S.; Bhatia, C. S. Understanding the Role of Nitrogen in Plasma-Assisted Surface Modification of Magnetic Recording Media with and without Ultrathin Carbon Overcoats. *Sci. Rep.* **2014**, *5*, 7772.

(35) Sun, Z.; Yan, Z.; Yao, J.; Beitler, E.; Zhu, Y.; Tour, J. M. Growth of Graphene from Solid Carbon Sources. *Nature* **2010**, *468*, 549−552.

(36) Kwon, K. C.; Choi, K. S.; Kim, S. Y. Increased Work Function in Few-Layer Graphene Sheets via Metal Chloride Doping. *Adv. Funct. Mater.* **2012**, *22*, 4724−4731.

Chapter 3.

Thiol-Based Surface Modification of InP Quantum Dots for Color Filter

3.1 Introduction

Semiconductor quantum dots (QDs) have been recognized as promising candidates for next-generation color displays because of their high photoluminescence quantum yields (PLQYs), narrow full widths at half maximum (FWHM), color tunability, and solution processability.[1-10] Cd-based QDs have excellent optical properties, such as unity PLQY and FWHM below 30 nm; however, commercialization is strictly regulated by the toxicity of Cd.[11,12] As representative eco-friendly III-V group QDs, InP QDs have been in the spotlight as an alternative to Cd-based QDs and are used in currently produced QD displays.[13-15]

The QD displays are largely classified into photo-enhanced, electro-emissive, and photo-emissive systems.[16,17] Photo-enhanced QD display refers to a structure in which QDs are integrated into a light-emitting diode (LED) backlight in a liquid crystal display (LCD). A representative example of this structure is the Samsung QLED television using Nanosys' quantum dot enhancement film (QDEF), in which red- and green-emitting InP QDs are embedded in the film to realize a wide color gamut. Electro-emissive systems utilize red, green, and blue-emitting QDs as electroluminescence materials, like the organic emitters of organic LEDs, and are anticipated to dominate the display industry in the future. A photo-emissive system called quantum dot color filter (QDCF) or quantum dot photoresist is formed by embedding QDs in a color filter and has the advantages of high color purity, efficient luminescence, wide-angle viewing, and improved contrast.[18,19]

Compatibility between QDs and photoresists is crucial for fabricating an effective QDCF. This compatibility affects the long-term stability of the QDCF by controlling the distance of QDs within the color filter and suppressing aggregation.[20-22] Furthermore, acrylic acid-based photoresist resin is mainly dissolved in propylene glycol monomethyl ether acetate (PGMEA) solvent in the display industry. This PGMEA solvent has the advantage of viscosity, is less volatile than alcohol solvent, and is easy to control film thickness. However, highly emissive InP QDs have a hydrophobic surface, making them difficult to dissolve in the PGMEA solvent and more likely to aggregate.

In this study, we introduced phenylethyl mercaptan (PEM) ligand to InP@ZnSeS QDs for dissolving the QDs in PGMEA. By injecting ligands into QDs crude solution at high temperatures, we achieved a PLQY retention of over 75% without a peak shift in the emission spectra during the ligand exchange process. Our strategy is applicable regardless of the size and emission wavelength of QDs. In

addition, surface-engineered QDs showed high colloidal stability in PGMEA for more than one month with little change in optical properties.

3.2 Results and discussion

We synthesized oleic acid-capped InP@ZnSeS QDs (OA-capped QDs) by hot-injection method (details provided in the Experimental section). In a typical synthesis, Zn-oleate, $InCl_3$, and 1-octadecene (ODE) were added to a three-necked round-bottom flask and degassed under vacuum. The prepared tri(methylsilyl)phosphine-tri-*n*-octylphosphine (TMSP-TOP) complex was injected into this solution to form an InP core. Then, eco-friendly QDs were synthesized by overcoating the ZnSeS shell at high temperatures with TOP-Se and TOP-S. The emission wavelength of QDs was 524 nm, and a high PLQY of above 80% was achieved.

As shown in Figure 3.1, the as-prepared QDs are passivated with hydrophobic OA ligands and are not dispersed in the PGMEA solvent. We engineered the surface of OA-capped QDs with thiol ligands that have a stronger bonding affinity than the carboxylic acid of OA.[23,24] To suppress the reduction of photoluminescence efficiency and aggregation during the ligand exchange process, we used a crude QDs solution without further purification.[25] The formation of a defect state on the surface of QDs during the washing procedure results in a loss of optical characteristics during the ligand exchange procedure. The crude solution was loaded in a three-necked round-bottom flask, converted to an inert atmosphere, and thiol ligands were injected at high temperatures. Thiol ligands of PEM, 2-mercaptoethanol, and 3-mercaptopropionic acid with high polarity are utilized to compare compatibility with PGMEA solvent (Figure 3.2). The PEM-treated InP QDs showed good solubility in the PGMEA solvent, and we conducted further optimization experiments.

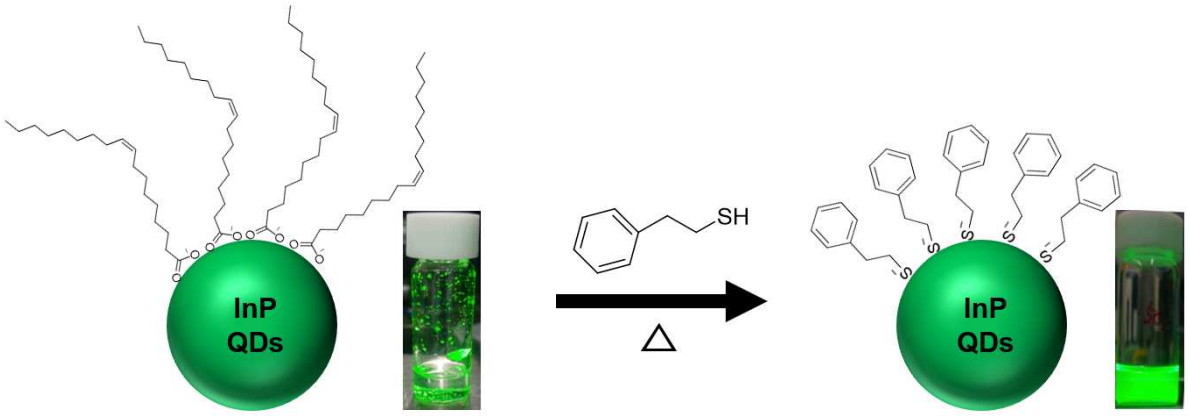

Figure 3.1. Surface engineering of InP@ZnSeS QDs. The schematic depicts the ligand exchange of oleic acid-capped InP@ZnSeS QDs with thiol ligand to modulate the compatibility. The InP@ZnSeS QDs capped with phenylethyl mercaptan (PEM) are dispersible in propylene glycol monomethyl ether acetate (PGMEA) solvent. The photographs in the inset show the InP@ZnSeS QDs in PGEMA.

We investigated changes depending on the concentration of PEM ligands, reaction temperature, and reaction time to optimize the ligand exchange procedure. First, we treated ligands while increasing the amount of PEM from 0.5 mmol to 20 mmol based on 4 mL of crude solution (Figure 3.3a). Only some OA ligands were exchanged when the ligand was less than 5 mmol, resulting in a low yield of PGMEA-dispersed QDs. In contrast, QDs were well dispersed in PGMEA when the amount of ligand was greater than 5 mmol, but PLQY tended to decrease as the amount of ligand increased. The PLQY retention shows the highest value of 74.9% at 5 mmol of PEM (Table 3.1). The reaction temperature is involved in ligand exchange dynamics and greatly influences PLQY and the chemical yield of PGMEA-dispersed QDs. The PEM ligands were not introduced sufficiently to OA-capped QDs because of a slow exchange reaction below 200 ºC. The maximum substitution efficiency was observed at 200 ºC, slightly lower than the boiling point of PEM at 217 ºC (Figure 3.3b and Table 3.2). The PEM vaporized, and the ligand was desorbed at a temperature higher than the boiling point of PEM, which reduced the optical properties of QDs. Reaction time also plays an important role in this ligand exchange method. The ligand exchange was completed in 2 hours at a reaction temperature of 200 ºC (Figure 3.3c and Table 3.3). When the high temperature is maintained for a long time, the concentration of PEM ligand in the solution decreases due to vaporization, and the passivation ratio of OA ligand increases again.

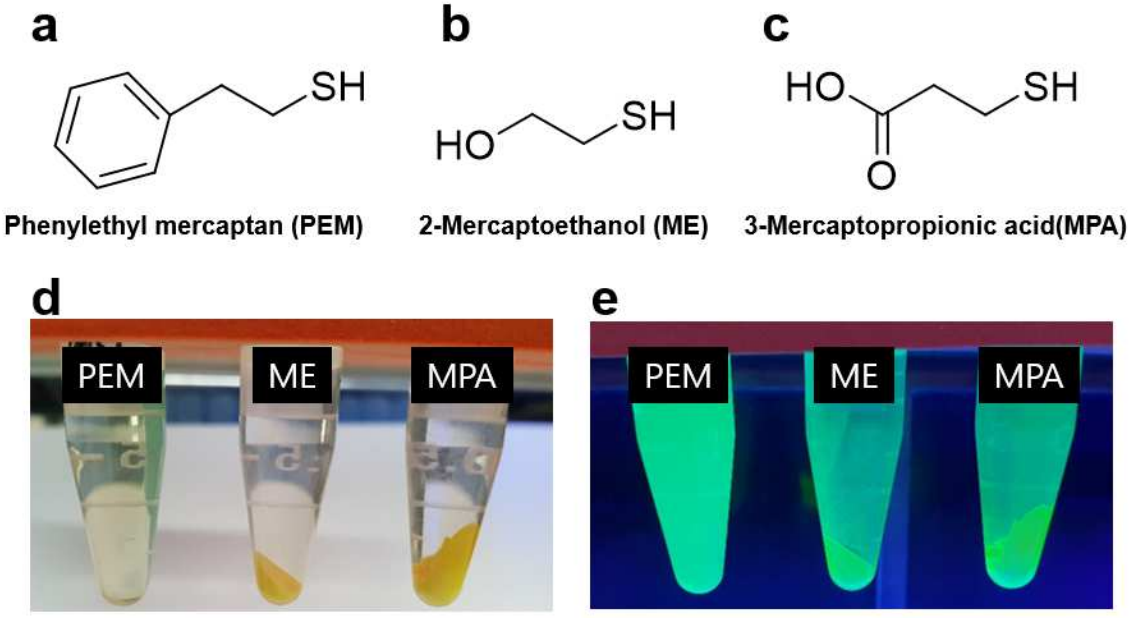

Figure 3.2. Molecular structures of (a) PEM, (b) 2-mercaptoethanol, and (c) 3-mercaptopropionic acid. Photographs under (d) room light and (e) 365 nm UV light of the surface-engineered InP@ZnSeS QDs in PGMEA depending on the types of thiol ligands.

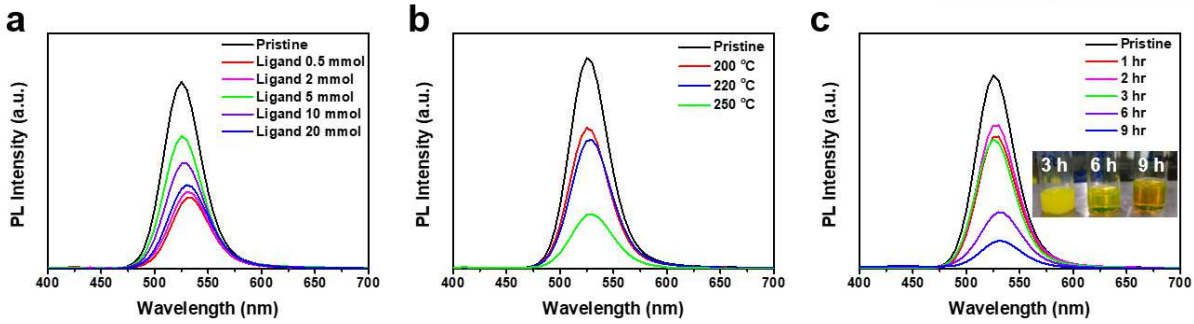

Figure 3.3. Photoluminescence spectra of surface-engineered QDs depending on the various reaction conditions such as (a) concentration of PEM ligands, (b) reaction temperature, and (c) reaction time.

Table 3.1. The optical properties of surface-engineered QDs depending on the concentration of PEM ligands.

Reaction Temp.	Number of ligands	Solvent	Emission (nm)	FWHM (nm)	PLQY (%)	QY retention
Pristine		Hexane	524.96	40.95	80.43	
200 °C	0.5 mmol	PGMEA	533.07	41.90	35.23	43.80%
	2 mmol		532.22	43.05	39.49	49.10%
	5 mmol		525.68	41.99	60.23	74.89%
	10 mmol		527.57	43.56	52.77	65.61%
	20 mmol		530.89	44.67	44.01	54.72%

Table 3.2. The optical properties of surface-engineered QDs depending on the reaction temperature.

Reaction time	Reaction Temp.	Solvent	Emission (nm)	FWHM (nm)	PLQY (%)	QY retention
Pristine		Hexane	526.21	41.71	82.26	
3 hr	200 °C	PGMEA	528.80	42.52	54.03	65.68%
	220 °C		528.72	44.13	50.00	60.78%
	250 °C		529.53	45.56	28.77	34.97%

Table 3.3. The optical properties of surface-engineered QDs depending on the reaction time.

Reaction Temp.	Reaction time	Solvent	Emission (nm)	FWHM (nm)	PLQY (%)	QY retention
Pristine	-	Hexane	526.21	41.71	82.26	-
200 ºC	1 hr	PGMEA	527.92	42.26	53.76	65.35%
	2 hr		527.63	42.66	60.89	74.02%
	3 hr		528.80	42.52	54.03	65.68%
	6 hr		532.11	45.30	24.77	30.11%
	9 hr		531.29	45.24	10.99	13.36%

The size and size distribution of OA-capped QDs and PEM-capped QDs were measured through dynamic light scattering (Figure 3.4). The solvodynamic diameter of OA-capped QDs decreased from 11.3 nm to 9.3 nm after ligand exchange, and there was no significant aggregation between QDs (Table 3.4). A relatively shorter length of PEM than OA successfully passivates the surface of InP@ZnSeS QDs. The surface environments of the QDs are analyzed by Fourier transform-infrared spectroscopy (Figure 3.5). The absorption peaks near 3008, 2926, 2850, and 1560 cm^{-1} appear in OA-capped QDs and represent the =C-H stretching vibrations, CH_2 stretching vibrations, CH_3 stretching vibrations, and COO^- asymmetric stretching vibrations, respectively. In particular, the C=O stretching peak at 1711 cm^{-1} of OA is shifted to 1560 cm^{-1} after chelating with metal at the surface of QDs. The OA, PEM-capped QDs show peaks at 3032, 1946, and 1494 cm^{-1}, which are not seen in the OA-capped QDs. These peaks indicate C-H stretching (aromatic), overtone, and C-C stretching (aromatic) vibration originating from the phenyl group in PEM ligand. It is worth noting that some OA ligands are not completely substituted by PEM and remain after PEM ligand treatment. In addition, we performed ^1H nuclear magnetic resonance analysis to calculate the ratio of OA and PEM ligands on the surface of QDs (Figure 3.6). The proton adjacent to the unsaturated double bond of OA shows a resonance peak at 5.3 ppm, and the proton in the aromatic ring of PEM shows multiple peaks at around 7.3 ppm. Integration of these peaks confirms that the ligand ratios of OA and PEM on OA, PEM-capped QDs are 28.3% and 71.7%, respectively. It is consistent with the FT-IR results that some OA ligands are bound to the surface of the QDs.

Table 3.4. Average particle size and size distribution of OA-capped QDs and OA, PEM-capped QDs by dynamic light scattering.

Sample	Size (nm)	Z-average (nm)	Polydispersity index
OA-capped QDs	11.10	18.97	0.37
PEM-capped QDs	9.31	12.36	0.13

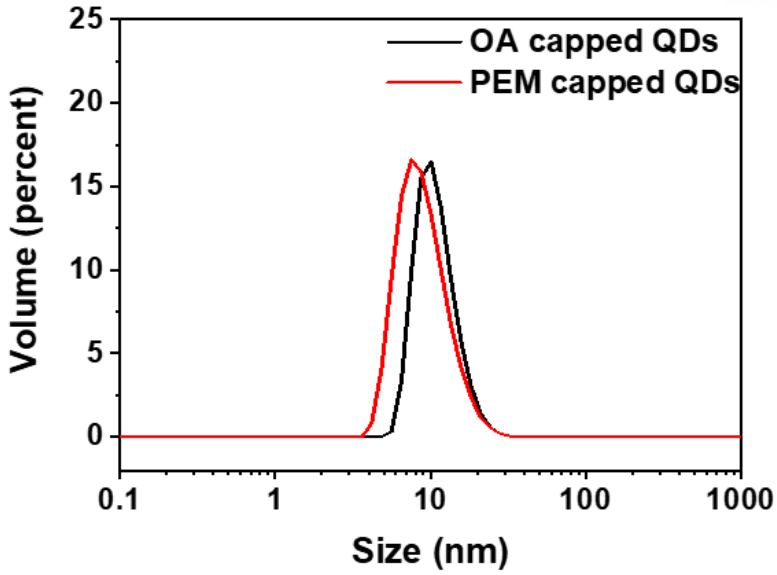

Figure 3.4. Dynamic light scattering data of OA-capped QDs and PEM-capped QDs.

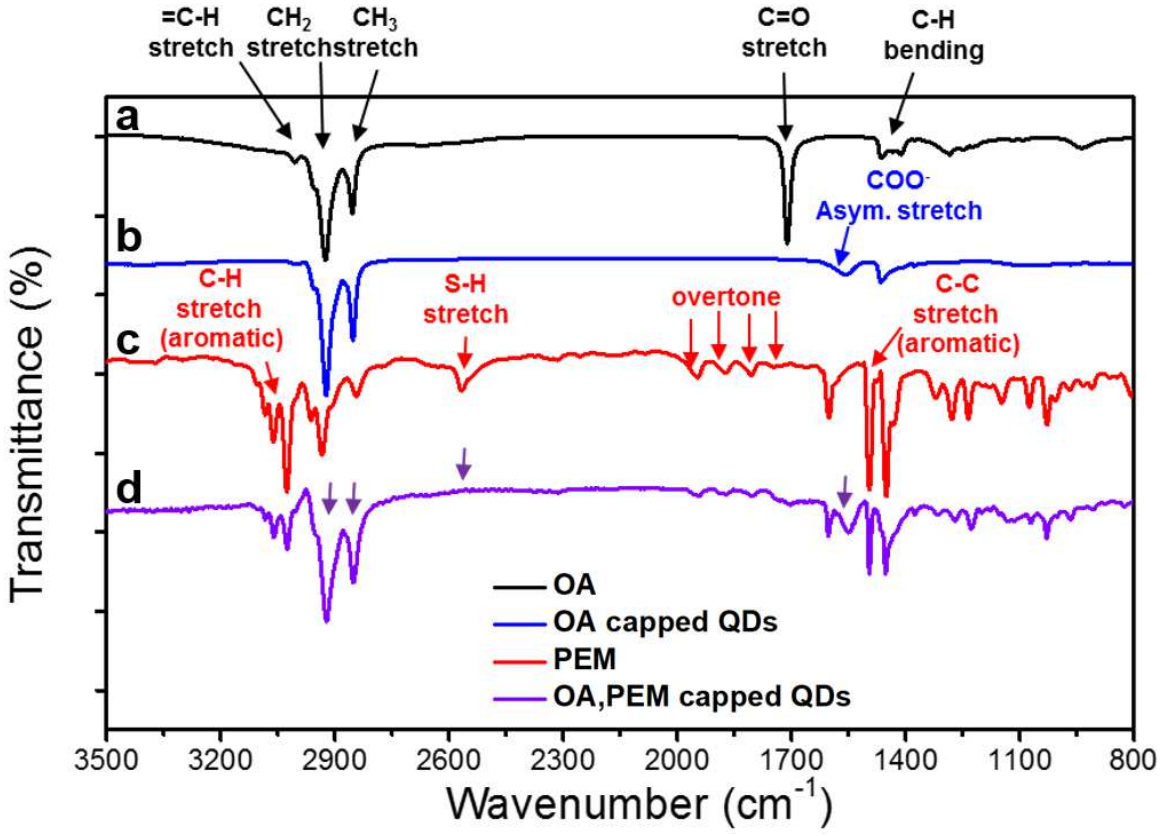

Figure 3.5. Fourier transform-infrared spectroscopy spectra of (a) OA, (b) OA-capped QDs, (c) PEM, and (d) OA, PEM-capped QDs.

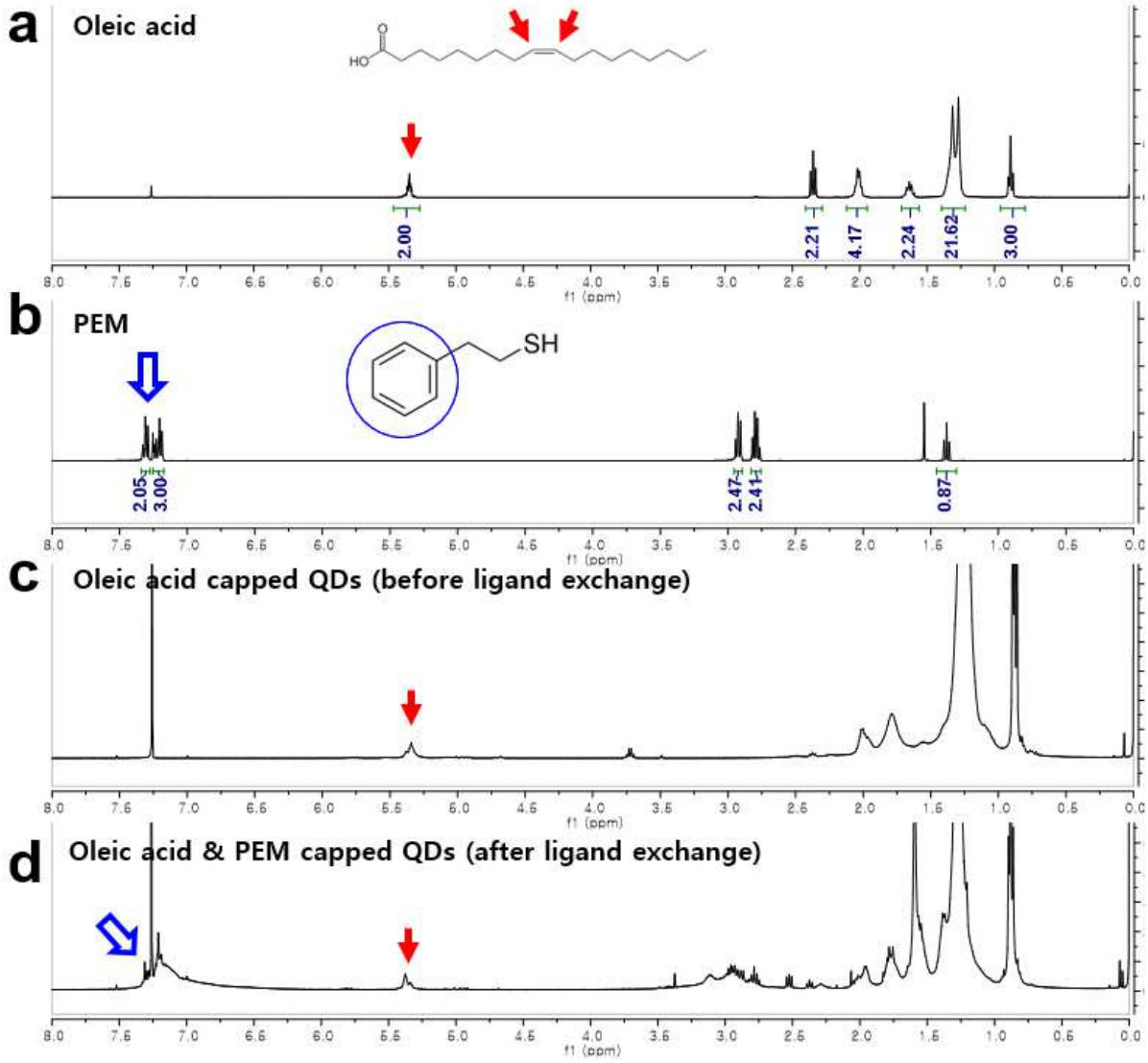

Figure 3.6. ^{1}H nuclear magnetic resonance (proton NMR) spectra of (a) OA, (b) PEM, (c) OA-capped QDs, and (d) OA, PEM-capped QDs dissolved in $CDCl_3$.

We investigated the applicability of the PEM ligand system to various QDs with different sizes and emission wavelengths. Since most commercially available display devices have used blue backlight, it is crucial to utilize QDs for color conversion in the red and green emitting range. Three types of InP@ZnSeS QDs with emission wavelengths of 534, 593, and 615 nm were prepared by adjusting the size of the InP core. After ligand exchange at 200 °C for 2 h, these three QDs were successfully dispersed in PGMEA, retaining their PLQYs of over 76% (Figure 3.7 and Table 3.5). Our ligand exchange is a highly versatile method, regardless of the emission wavelength of InP@ZnSeS QDs. Furthermore, we monitored the colloidal stability of OA, PEM-capped QDs with various emission wavelengths. Upon examining the colloidal stability of QDs that had been stored under an environment with a relative humidity of 60% and room temperature of 25 °C, little change in emission peak and FWHM was observed over 30 days, and over 99% of the initial PLQY was retained (Figure 3.8).

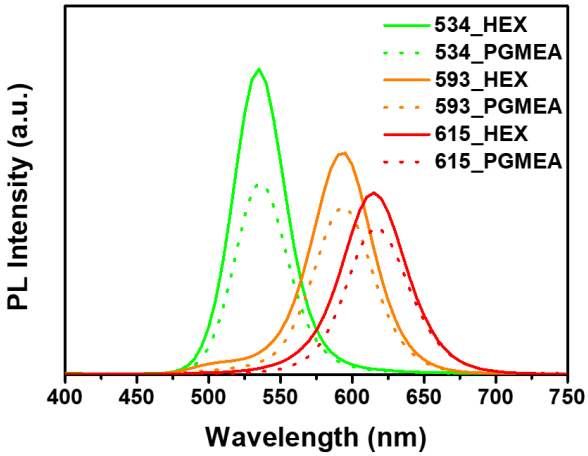

Figure 3.7. Photoluminescence spectra of surface-engineered QDs with emission wavelengths of 534 nm, 593 nm, and 615 nm.

Table 3.5. The optical properties of surface-engineered QDs with emission wavelengths of 534 nm, 593 nm, and 615 nm.

Sample	Emission wavelength	Solvent	Emission (nm)	FWHM (nm)	PLQY (%)	QY retention
Pristine	534 nm	Hexane	534.83	41.99	84.61	-
PEM		PGMEA	536.22	42.93	49.85	58.92%
Pristine	593 nm	Hexane	593.44	49.62	77.69	-
PEM		PGMEA	594.45	49.19	60.30	77.62%
Pristine	615 nm	Hexane	615.01	52.19	70.99	-
PEM		PGMEA	616.50	51.39	54.05	76.14%

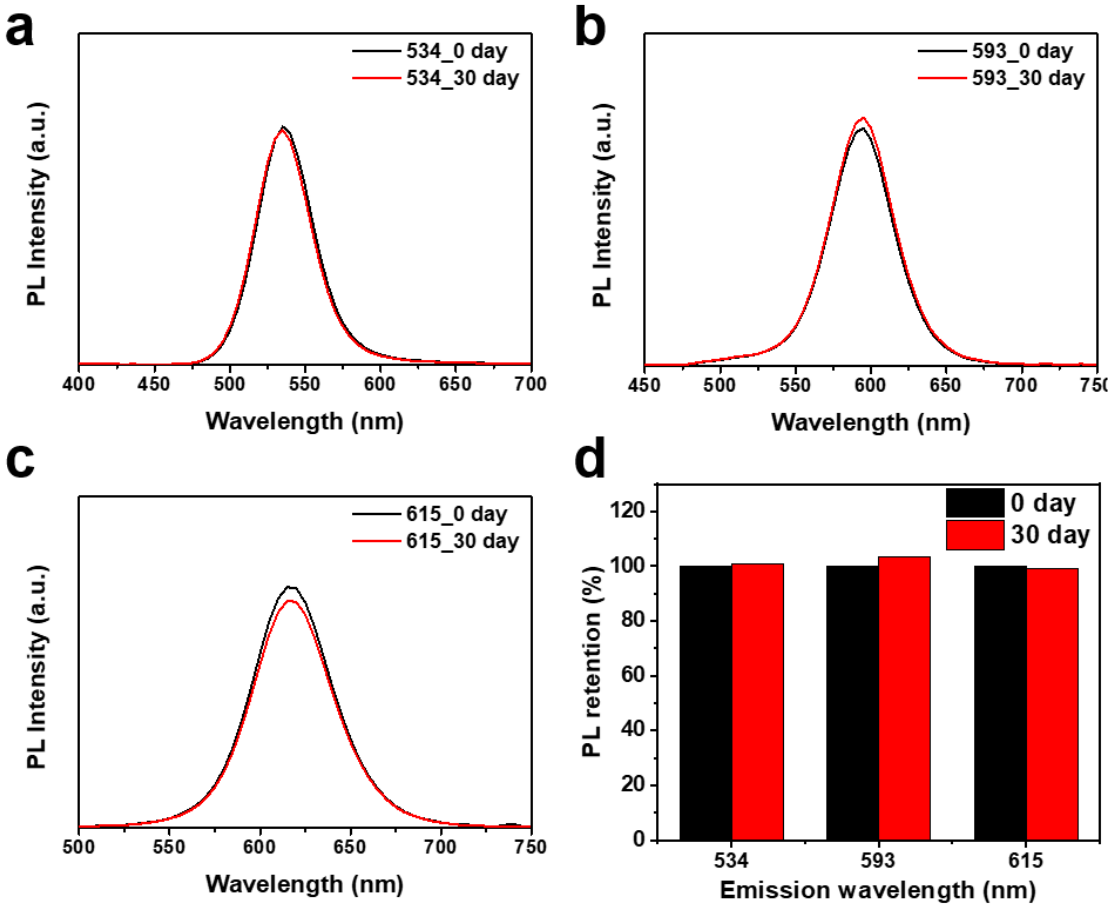

Figure 3.8. The colloidal stability of surface-engineered QDs. Changes in photoluminescence spectra of QDs with emission wavelengths of (a) 534 nm, (b) 593 nm, and (c) 615 nm. (d) Photoluminescence retention of QDs after one-month storage in ambient conditions.

3.3 Conclusion

In summary, we have developed a novel thiol-based ligand exchange method for PGMEA soluble InP@ZnSeS QDs. PEM ligands are used as surface modifiers, substituting the original OA ligands. The defect formation on the QDs' surface was minimized, and PLQY was preserved by more than 75% during ligand exchange by optimizing ligand concentration, reaction temperature, and reaction time. It was effective to react for a short time at a temperature slightly lower than the boiling point in the crude solution, and the surface of the PEM-capped QDs was confirmed through FT-IR and proton NMR. This PEM-based ligand system was also effective for InP QDs with various emission wavelengths. In addition, the PEM-capped QDs exhibited high colloidal stability without degradation of PLQY for one month in PGMEA. Our strategy could expand the QD color conversion layer development for highly emissive QD displays.

3.4 Experimental section

Materials. Oleylamine (OLAM, 98%), ODE (90%), OA (90%), zinc acetate (99.99%), indium (III) chloride (99.999%), gallium chloride (99.99%), indium(III) acetylacetonate ($In(acac)_3$, 99.99%), zinc(II) acetylacetonate ($Zn(acac)_2$), selenium (Se, 99.99%), TOP (97%), sulfur (S, 99%), 1-dodecanethiol (DDT, 98%), toluene (anhydrous, 99.8%), tetrahydrofuran (THF, 99.9%), PEM (99%), PGMEA (99.5%), *n*-hexane (anhydrous; 95%), and acetone (99.5%) were purchased from Sigma-Aldrich. TMSP (99%) was obtained from SK Chemicals. All chemicals were used without further purification.

Preparation of precursors. Zn-oleate was prepared by loading zinc acetate (5.5 g, 30 mmol), OA (19 mL, 60 mmol), and ODE (41 mL) into a three-necked round-bottom flask. The mixture was degassed under a vacuum at 120 ºC for 2 h. After degassing, the solution was heated up to 300 ºC and maintained for 10 min under Ar atmosphere. TOP-Se (0.5 M) was obtained by dissolving the Se powder (15.8 mg, 0.2 mmol) in 0.4 mL of TOP in an Ar-filled glovebox. TOP-S (1.0 M) was prepared by dissolving the S powder (9.6 mg, 0.3 mmol) in 0.3 mL of TOP in an Ar-filled glovebox. We prepared TMSP-TOP solution by mixing 0.3 mL of TMSP and 0.5 mL of TOP. In-Zn-P complex was synthesized by referring to the previous report.[26] $In(acac)_3$ (0.41 g, 1 mmol), $Zn(acac)_2$ (0.13 g, 0.5 mmol), OA (1.3 mL, 4 mmol), and ODE (10 mL) were loaded into 50 mL three-necked round-bottom flask and degassed under vacuum at 120 ºC for 1 h. After cooling the mixture to room temperature, 0.19 mL of TMSP and 1 mL of TOP were added to the mixture.

Synthesis of green-emitting InP@ZnSeS QDs. The 4 mL of Zn-oleate, 6 mL of ODE, 0.2 mL of THF, and 0.1 mmol of $InCl_3$ powder were loaded in a 50 mL of a three-necked round-bottom flask and degassed under vacuum at 160 ºC for 1 h. The mixture was cooled down to 100 ºC and heated to 280 ºC for 10 min. Then, 0.5 mL of TMSP-TOP solution was injected into the mixture at 280 ºC and maintained the reaction for 1 h. After InP core growth, ZnSeS shells were overcoated at 150 ºC by adding 0.6 mL of TOP-Se and 0.3 mL of TOP-S. The mixture was heated to 300 ºC for 10 min and reacted for 2 h. The crude solution was washed by adding excess acetone and redispersed in hexane. For the ligand exchange, we used the crude solution without an anti-solvent washing step.

Synthesis of red-emitting InP@ZnSeS QDs. The 2 mL of Zn-oleate, 0.1 mL of THF, and 0.05 mmol of $InCl_3$ powder were loaded into 50 mL of a three-necked round-bottom flask and degassed under vacuum at 70 ºC for 30 min. The mixture was reacted at 140 ºC for 1h and heated up to 280 ºC for 10 min. Then, 0.1 mL of TMSP-ODE, 0.12 mL of TOP, and 0.06 mmol of $GaCl_3$ solution were injected into the mixture at 280 ºC and maintained the reaction for 1 h. The size of InP core was

increased via continuous injection of In-Zn-P complex. We injected In-Zn-P complex for 3 h in a rate of 1 mL/h. After InP core growth, ZnSeS shells were overcoated at 150 ºC by adding 0.3 mL of TOP-Se, 0.15 mL of TOP-S, and 0.3 mL of ODE. The mixture was heated to 300 ºC for 10 min and reacted for 1 h. Finally, 0.14 mL of DDT ligands were introduced to the reaction batch at 120 ºC and reacted for 30 min. The crude solution was washed by adding excess acetone and redispersed in hexane. We used the crude solution without an anti-solvent washing step for the ligand exchange.

Surface engineering of QDs. The standard ligand exchange method is described as follows. The crude QDs solution (4 mL) was loaded in 50 mL of a three-necked round-bottom flask and degassed under vacuum at room temperature for 1 h. After Ar backfill, the solution was heated up to 200 ºC for 15 min. The PEM ligands of 5 mmol were injected into the solution at reaction temperature and reacted for 2 h. Surface-engineered QDs were washed via centrifugation at 13000 rpm for 10 min. After discarding the supernatant, the precipitates were dispersed in PGMEA solvent and centrifuged at 13000 rpm for 5 min to eliminate aggregated QDs.

Characterization. Absorption spectra were measured by a Shimadzu UV-1800 UV–vis spectrometer. Photoluminescence (PL) spectroscopy and quantum yields were obtained for the QDs via a quantum efficiency measurement system (Otsuka QE-2000). DLS measurements were performed on a Malvern Instruments Zetasizer Nano-ZS90 at 25 °C. The surface of the QDs was analyzed by Fourier transform-infrared spectroscopy (Shimadzu, Kyoto, Japan, IRTracer-100). ^{1}H nuclear magnetic resonance spectra were acquired using a Bruker AVANCE III HD (400 MHz) spectrometer.

3.5 References

(1) Chen, S.; Cao, W.; Liu, T.; Tsang, S.-W.; Yang, Y.; Yan, X.; Qian, L. On the Degradation Mechanisms of Quantum-Dot Light-Emitting Diodes. *Nat. Commun.* **2019**, *10*, 765.

(2) Kamat, P. V. Quantum Dot Solar Cells. Semiconductor Nanocrystals as Light Harvesters. *J. Phys. Chem. C* **2008**, *112*, 18737.

(3) Song, J.; Wang, O.; Shen, H.; Lin, Q.; Li, Z.; Wang, L.; Zhang, X.; Li, L. S. Over 30% External Quantum Efficiency Light-Emitting Diodes by Engineering Quantum Dot-Assisted Energy Level Match for Hole Transport Layer. *Adv. Funct. Mater.* **2019**, *29*, 1808377.

(4) Ding, K.; Fang, Y.; Dong, S.; Chen, H.; Luo, B.; Jiang, K.; Gu, H.; Fan, L.; Liu, S.; Hu, B.; *et al*. 24.1% External Quantum Efficiency of Flexible Quantum Dot Light-Emitting Diodes by Light Extraction of Silver Nanowire Transparent Electrodes. *Adv. Optical Mater.* **2018**, *6*, 1800347.

(5) Zhang, H.; Chen, S.; Sun, X. W. Efficient Red/Green/Blue Tandem Quantum-Dot Light-Emitting Diodes with External Quantum Efficiency Exceeding 21%. *ACS Nano* **2018**, *12*, 697.

(6) Kwak, J.; Bae, W. K.; Lee, D.; Park, I.; Lim, J.; Park, M.; Cho, H.; Woo, H.; Yoon, D. Y.; Char, K.; *et al*. Bright and Efficient Full-Color Colloidal Quantum Dot Light-Emitting Diodes Using an Inverted Device Structure. *Nano Lett.* **2012**, *12*, 2362.

(7) Qian, L.; Zheng, Y.; Xue, J.; Holloway, P. H. Stable and Efficient Quantum-Dot Light-Emitting Diodes Based on Solution-Processed Multilayer Structures. *Nat. Photonics* **2011**, *5*, 543.

(8) Coe, S.; Woo, W.-K.; Bawendi, M.; Bulović, V. Electroluminescence from Single Monolayers of Nanocrystals in Molecular Organic Devices. *Nature* **2002**, *420*, 800.

(9) Colvin, V. L.; Schlamp, M. C.; Alivisatos, A. P. Light-Emitting Diodes Made from Cadmium Selenide Nanocrystals and A Semiconducting Polymer. *Nature* **1994**, *370*, 354.

(10) Ju, S.; Zhu, Y.; Hu, H.; Liu, Y.; Xu, Z.; Zheng, J.; Mao, C.; Yu, Y.; Yang, K.; Lin, L.; *et al*. Dual-function Perovskite Light-Emitting/Sensing Devices for Optical Interactive Display. *Light Sci. Appl.* **2022**, *11*, 331.

(11) Yu, P.; Cao, S.; Shan, Y.; Bi, Y.; Hu, Y.; Zeng, R.; Zou, B.; Wang, Y.; Zhao, J. Highly Efficient Green InP-Based Quantum Dot Light-Emitting Diodes Regulated by Inner Alloyed Shell Component. *Light Sci. Appl.* **2022**, *11*, 162.

(12) Hanifi, D. A.; Bronstein, N. D.; Koscher, B. A.; Nett, Z.; Swabeck, J. K.; Takano, K.; Schwartzberg, A. M.; Maserati, L.; Vandewal, K.; van de Burgt, Y.; *et al*. Redefining Near-Unity Luminescence in Quantum Dots with Photothermal Threshold Quantum Yield. *Science* **2019**, *363*, 1199.

(13) Du, W.; Cheng, C.; Tian, J. Efficient Solution-Processed InP Quantum-Dots Light-Emitting Diodes Enabled by Suppressing Hole Injection Loss. *Nano Res.* **2022**. 1

(14) Jang, E.; Kim, Y.; Won, Y.-H.; Jang, H.; Choi, S.-M. Environmentally Friendly InP-Based

Quantum Dots for Efficient Wide Color Gamut Displays. *ACS Energy Lett.* **2020**, *5*, 1316.

(15) Chao, W.-C.; Chiang, T.-H.; Liu, Y.-C.; Huang, Z.-X.; Liao, C.-C.; Chu, C.-H.; Wang, C.-H.; Tseng, H.-W.; Hung, W.-Y.; Chou, P.-T. High Efficiency Green InP Quantum Dot Light-Emitting Diodes by Balancing Electron and Hole Mobility. *Commun. Mater.* **2021**, *2*, 96.

(16) Zhao, B.; Zhang, X.; Bai, X.; Yang, H.; Li, S.; Hao, J.; Liu, H.; Lu, R.; Xu, B.; Wang, L.; *et al*. Surface Modification Toward Luminescent and Stable Silica-Coated Quantum Dots Color Filter. *Sci. China Mater.* **2019**, *62*, 1463.

(17) Ko, Y.-H.; Prabhakaran, P.; Choi, S.; Kim, G.-J.; Lee, C.; Lee, K.-S. Environmentally Friendly Quantum-Dot Color Filters for Ultra-High-Definition Liquid Crystal Displays. *Sci. Rep.* **2020**, *10*, 15817.

(18) Lien, J.-Y.; Chen, C.-J.; Chiang, R.-K.; Wang, S.-L. High Color-Rendering Warm-White Lamps Using Quantum-Dot Color Conversion Films. *Opt. Express* **2016**, *24*, A1021.

(19) Zhao, B.; Wang, Q.; Li, D.; Yang, H.; Bai, X.; Li, S.; Liu, P.; Sun, X. Red and Green Quantum Dot Color Filter for Full-Color Micro-LED Arrays. *Micromachines*, **2022**, *13*, 595.

(20) Nasri, S.; Bardajee, G. R.; Bayat, M. Synthesis, Characterization and Energy Transfer Studies of Fluorescent Dye-Labeled Metal-Chelating Polymers Anchoring Pendant Thiol Groups for Surface Modification of Quantum Dots and Investigation on Their Application for pH-Responsive Controlled Release of Doxorubicin. *Colloids and Surf. B: Biointerfaces* **2018**, *171*, 544.

(21) Zillner, E.; Fengler, S.; Niyamakom, P.; Rauscher, F.; Köhler, K.; Dittrich, T. Role of Ligand Exchange at CdSe Quantum Dot Layers for Charge Separation. *J. Phys. Chem. C* **2012**, *116*, 16747.

(22) Sun, D.; Sue, H.-J.; Miyatake, N. Optical Properties of ZnO Quantum Dots in Epoxy with Controlled Dispersion. *J. Phys. Chem. C* **2008**, *112*, 16002.

(23) Devatha, G.; Roy, S.; Rao, A.; Mallick, A.; Basu, S.; Pillai, P. P. Electrostatically Driven Resonance Energy Transfer in “Cationic” Biocompatible Indium Phosphide Quantum Dots. *Chem. Sci.* **2017**, *8*, 3879.

(24) Kim, J.; Kim, Y.; Park, K.; Boeffel, C.; Choi, H.-S.; Taubert, A.; Wedel, A. Ligand Effect in 1-Octanethiol Passivation of InP/ZnSe/ZnS Quantum Dots—Evidence of Incomplete Surface Passivation during Synthesis. *Small* **2022**, *18*, 2203093.

(25) Chen, Y.; Cordero, J. M.; Wang, H.; Franke, D.; Achorn, O. B.; Freyria, F. S.; Coropceanu, I.; Wei, H.; Chen, O.; Mooney, D. J.; *et al*. A Ligand System for the Flexible Functionalization of Quantum Dots via Click Chemistry. *Angew. Chem. Int. Ed.* **2018**, *57*, 4652.

(26) Ramasamy, P.; Ko, K.-J.; Kang, J.-W.; Lee, J.-S. Two-Step “Seed-Mediated” Synthetic Approach to Colloidal Indium Phosphide Quantum Dots with High-Purity Photo- and Electroluminescence. *Chem. Mater.* **2018**, *30*, 3643.

Chapter 4.

Highly Emissive Blue Quantum Dots with Superior Thermal Stability via *In Situ* Surface Reconstruction of Mixed $CsPbBr_3$–Cs_4PbBr_6 Nanocrystals

Chapter 4 is reprinted with permission from "*H. Kim†, J. H. Park†, K. Kim, D. Lee, M. H. Song*, and J. Park*", Adv. Sci.* ***2022****, 9, 2104660.*" Copyright 2022, Wiley-VCH.

4.1 Introduction

Metal halide perovskite materials have been recognized as promising candidates for next-generation color displays because their high photoluminescence quantum yields (PLQYs), narrow full widths at half maximum (FWHM), ease of band-gap tuning, and solution processability fulfil the ITU-R Recommendation BT.2020 (Rec. 2020) of the International Telecommunication Union (ITU).[1-3] Recently, significant progress has been achieved in the development of near-infrared, red, and green perovskite light-emitting diodes (LEDs), with external quantum efficiencies (EQE) reaching over 20%.[4–8] However, the efficiency of blue perovskite materials has lagged far behind, with EQEs of 12.3% in the sky blue region of the spectrum (475–490 nm) and 8.8% in the blue region (460–475 nm) having been reported.[9,10] Furthermore, joule heating during LED operation is inevitable; thus, the development of perovskite materials with superior thermal stability, in which thermal quenching is minimized, is an important issue for the practical application of perovskite LEDs.

Several strategies for obtaining blue-emitting perovskites nanocrystals (NCs) are available. One method involves mixed halides that include both Br and Cl anions.[11,12–17] Although this is a convenient method for bandgap engineering, easy formation of Cl^- vacancies poses a limitation as it results in a deep trap state within the bandgap.[18–20] These defect sites cause perovskite layer degradation and ion migration, resulting in phase segregation in response to the application of an electric field during device operation.[21,22] A second method is to use Br-based two-dimensional perovskite nanoplatelets and take advantage of the exciton quantum confinement effect.[23–27] In inorganic cesium lead bromide ($CsPbBr_3$) nanoplatelets, the emission can be controlled according to the number of $[PbBr_6]^{4-}$ layers; however, strong exciton–phonon coupling and a randomly oriented distribution of nanoplatelets result in low-performance LEDs.[28] A third strategy for achieving blue-emitting perovskites nanocrystals (NCs) is to reduce the crystal size of a perovskite material such that it is within the quantum confinement regime.[9,29–32] $CsPbBr_3$ NCs with sizes in the quantum confinement regime (denoted by quantum dots, QDs) usually suffer from low PLQYs and stability because they are strongly affected by surface defects when the surface-to-volume ratio is high.[33] In particular, small-sized QDs are easily degraded and undergo aggregation because of their high surface energy, leading to broad emission spectra and poor spectral stability such that the emission color is susceptible to changing to green at high temperature.

To overcome these problems, various approaches have been attempted, including amorphous $CsPbBr_x$ shelling,[31] the addition of excess Br using $ZnBr_2$ as the source,[29] Sb^{3+} doping,[32] and acid etching-driven ligand exchange.[34] However, few studies have been conducted on the application of blue LEDs incorporating highly stable $CsPbBr_3$ QDs.[9,34] A quite different approach involves $CsPbBr_3$ NCs being embedded in a Cs_4PbBr_6 matrix with a crystal size of several hundred nanometers or more, resulting in improved PLQY and stability.[35–38] However, the literature reports in this area have been focused only on green emission, and $Cs_4PbBr_6/CsPbBr_3$ embedded structures are not suitable for electroluminescent devices because a zero-dimensional Cs_4PbBr_6 phase has a wide bandgap of 3.95 eV and is insulating.[39,40]

In this article, we report a unique method to enhance the PLQY and stability of blue-emitting $CsPbBr_3$ QDs via simultaneous generation of mixed $CsPbBr_3$ QDs and Cs_4PbBr_6 NCs. By controlling the reactivity of the precursors, the size of the $CsPbBr_3$ QDs was controlled. As a result, an emission wavelength of 470 nm with a high PLQY of >90% was achieved. We investigated the effects of the Cs_4PbBr_6 NCs on the photophysical properties and thermal stability of the $CsPbBr_3$ QDs by observing changes in their morphology and optoelectronic properties. Octahedron defect sites on the surface of $CsPbBr_3$ QDs were etched by the Cs_4PbBr_6 NCs, resulting in defect removal. This $CsPbBr_3$ QD surface reconstruction decreases the defect density and eliminates nonradiative recombination pathways, leading to high efficiency and stability for the $CsPbBr_3$ QDs. The mixed NC solution retained 90% of its initial PLQY value over 120 days of storage under ambient conditions, with little change in the emission peak position and FWHM. Thermally induced aggregation and fusion were suppressed during 60 min of heating at 120 °C. Spectrally stable and efficient blue LEDs, having an EQE of 4.65% at 480 nm, based on the mixed NCs were achieved.

4.2 Results and discussion

Preparation of in situ generated blue-emitting NCs

We synthesized a mixed solution of $CsPbBr_3$ and Cs_4PbBr_6 NCs by modifying a previously reported synthetic method (details provided in the Experimental section).[41] In a typical synthesis, Cs_2CO_3, PbO, oleic acid (OA), and 1-octadecene (ODE) were added to a three-necked round-bottom flask, and metal oleate complexes were formed by heating at 120 °C. Oleylammonium bromide (OLAM-Br) was prepared separately by reacting oleylamine and HBr, and then this was injected at low-temperature under Ar into the metal oleate complexes. In this step, the reaction temperature and the Cs to Pb precursor ratio, as important factors for obtaining high-quality NCs with blue emission in the range of 460 nm to 480 nm, were carefully controlled. The $CsPbBr_3$ to Cs_4PbBr_6 NC formation ratio was modulated by varying the Cs to Pb precursor feed ratio, as described in a previous report.[42] When the amount of Pb precursor exceeded the amount of Cs precursor, the formation of $CsPbBr_3$ NCs in the orthorhombic phase was favored (Figure 4.1). When the Cs and Pb precursor ratio was fixed at 1:1 and the reaction temperature was reduced, the growth of NCs was suppressed, and small $CsPbBr_3$ NCs and Cs_4PbBr_6 NCs were simultaneously co-synthesized. The emission wavelength of the QDs was 470 nm, and a high photoluminescence quantum yield (PLQY) of above 90% was achieved. This phenomenon occurred because the depletion of the Pb precursor was slower than that of the Cs-precursor.[42,43] At low temperature, the difference between the reactivities of the metal precursors was maximized, hence formation of Cs_4PbBr_6 NCs was promoted and the size of the $CsPbBr_3$ NCs was reduced (Figure 4.2).

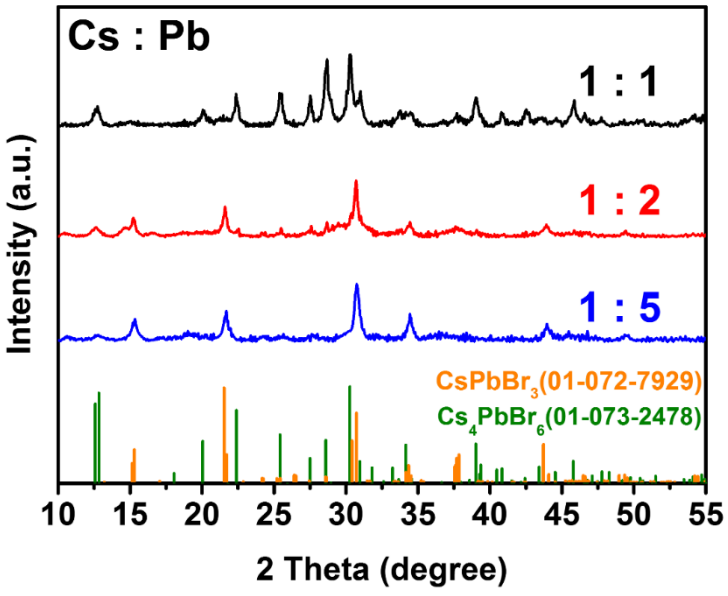

Figure 4.1. X-ray powder diffraction (XRD) patterns according to the feeding molar ratio of Cs and Pb precursor.

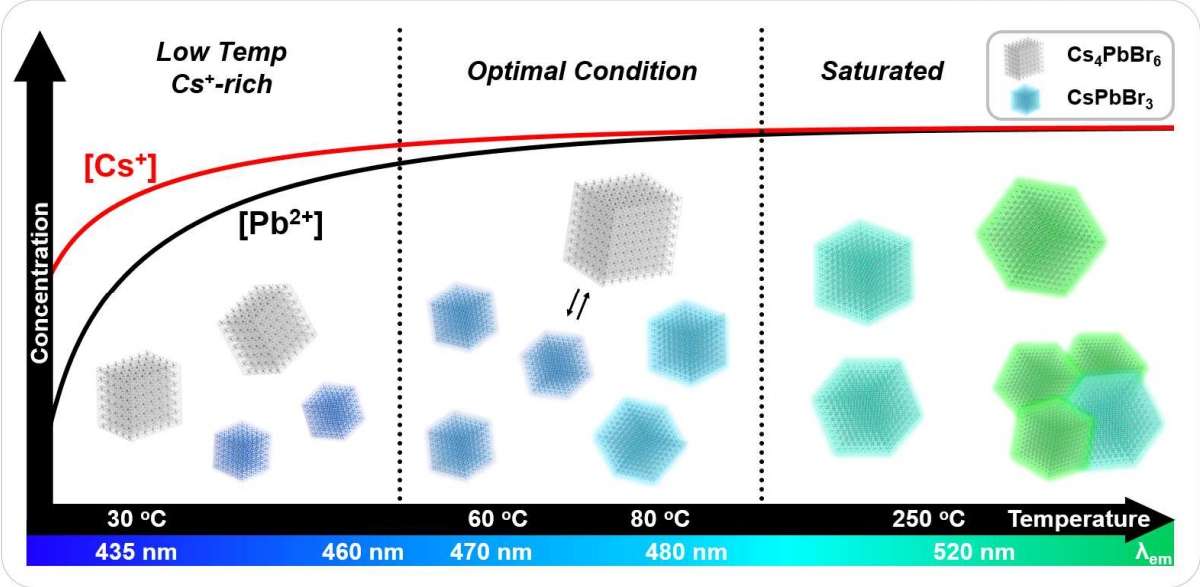

Figure 4.2. Schematic representation of temperature-dependent growth trend of perovskite nanoparticles. The schematic depicts the active metal precursor ion concentrations and products ($CsPbBr_3$ and Cs_4PbBr_6 nanocrystals) as functions of increasing reaction temperature. The colored *x*-axis that gradually changes from blue to green indicates the $CsPbBr_3$ NC emission wavelength.

We investigated the dependence of the photophysical properties of the as-synthesized NCs on the reaction temperature in the range of 60 °C to 160 °C. These NCs exhibited two peaks in the UV–vis absorption spectra: the first excitonic peak, between 450 nm and 500 nm, and a sharp peak centered at 313 nm (Figure 4.3a). The absorption peak at 313 nm originated from optical transitions between localized states of the isolated $[PbBr_6]^{4-}$ octahedron of Cs_4PbBr_6 NCs.[44–46] X-ray powder diffraction (XRD) patterns of the NCs allowed us to confirm that the first exciton peak is related to the bandgap of the luminescent $CsPbBr_3$ NCs. As shown in Figure 4.3b, the sample of synthesized NCs included both orthorhombic $CsPbBr_3$ NCs and rhombohedral Cs_4PbBr_6 NCs, and the Cs_4PbBr_6-to-$CsPbBr_3$ ratio increased as the reaction temperature decreased. This result is consistent with the increase in the intensity of the absorption peaks at 313 nm in the UV–vis spectra. As the reaction temperature decreased from 160 °C to 60 °C, the first exciton peak was blue-shifted, and the emission peak center shifted from the green (504 nm) to the blue (470 nm) wavelength region (Figure 4.3c). Transmission electron microscopy (TEM) analysis also indicated that $CsPbBr_3$ and Cs_4PbBr_6 NCs coexisted in the samples, and lowering the temperature reduced the overall size of the NCs (Figure 4.3d–g and 4.4). In addition, when the particle sizes (diameters) were measured by focusing on the luminescent $CsPbBr_3$ NCs, the average size and relative standard deviations decreased from 9.3 nm to 3.5 nm and from 38.1% to 9.0%, respectively, as the reaction temperature decreased from 160 °C to 60 °C, because of the slow crystal growth rate at low temperature (Figure 4.3h). Because the size of the $CsPbBr_3$ NCs synthesized at a temperature below 160 °C was smaller than the excitonic Bohr radius (~7 nm),[47] the blue shift in the

emission peaks resulted from a quantum confinement effect, and the reduction in FWHM was due to the size distribution and defect density decrease. It should be noted that as the reaction temperature decreases, the PLQY increases from 57.7% to 90.1%, contrary to previously reported general trends of increasing crystallinity and PLQY with temperature (Figure 4.3i).[41]

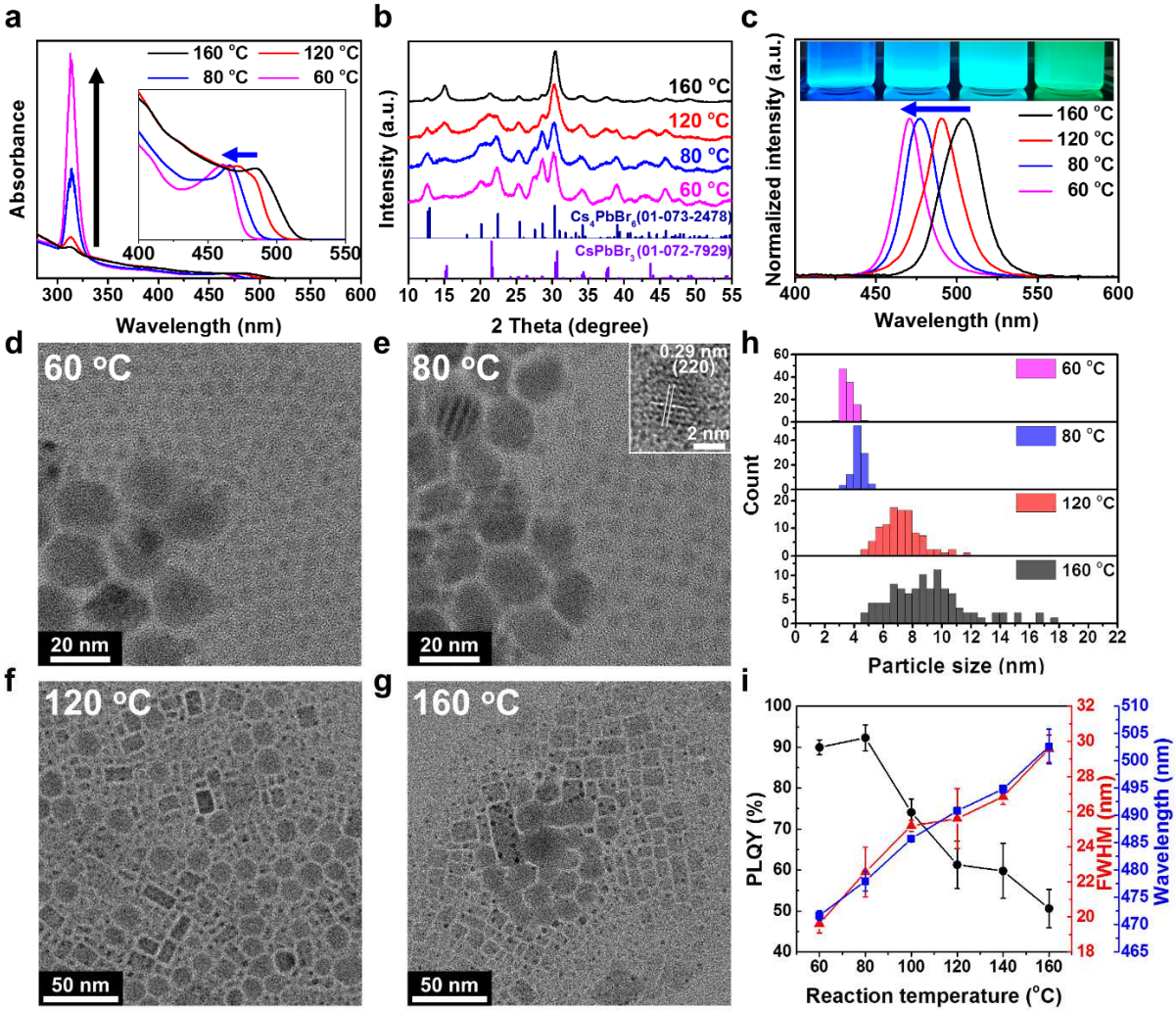

Figure 4.3. Characterization of perovskite NCs depending on the reaction temperature. (a) UV–vis absorption spectra, (b) XRD patterns, and (c) PL spectra of samples synthesized at 60 °C, 80 °C, 120 °C, and 160 °C, respectively. The insets are photographs of perovskite NCs in non-polar solvents acquired under 365 nm UV light illumination. TEM images of the samples synthesized at (d) 60 °C, (e) 80 °C, (f) 120 °C, and (g) 160 °C; the inset of (e) shows a high-resolution TEM image the of $CsPbBr_3$ NCs prepared at 80 °C. (h) Histograms illustrating the distributions of $CsPbBr_3$ NCs sizes for the samples prepared at different reaction temperatures. (i) Variations in emission wavelength, PLQY, and FWHM of the as-synthesized products with reaction temperature.

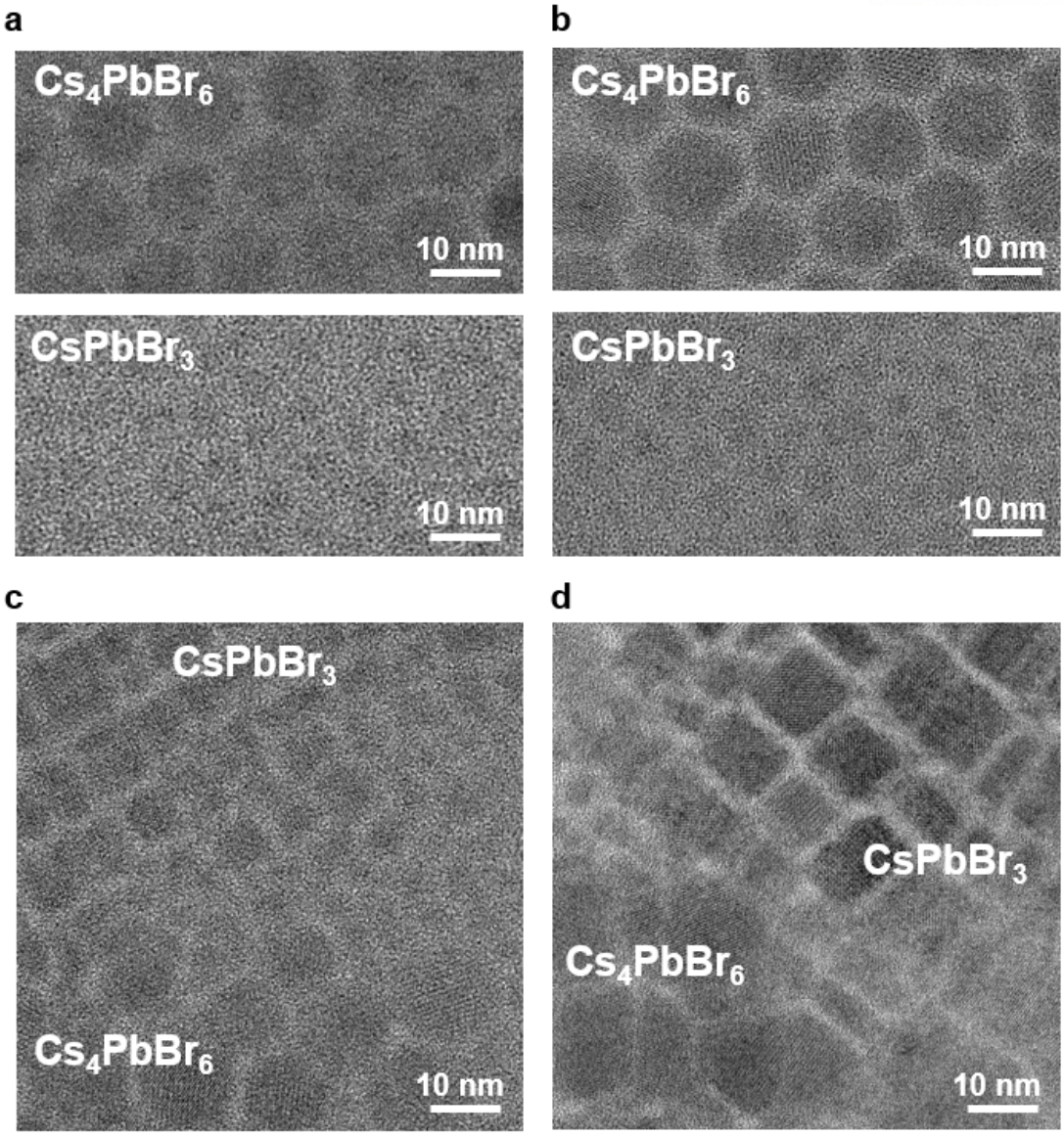

Figure 4.4. High magnification transmission electron microscopy (TEM) images of the in situ generated $CsPbBr_3$-Cs_4PbBr_6 nanocrystals (ISNCs) synthesized at (a) 60 ºC, (b) 80 ºC, (c) 120 ºC, and (d) 160 ºC.

Stability of in situ generated perovskite NCs

In order to analyze the stability of the in situ generated $CsPbBr_3$-Cs_4PbBr_6 NCs (denoted by ISNCs), we synthesized small $CsPbBr_3$ QDs (denoted by C-QD_{113}) as a control group using a conventional method based on hot injection of Cs-oleate at 90 °C with control of the OA and OLAM ligands (details provided in the Figure 4.5 and the Experimental section).[48] Conventional $CsPbBr_3$ QDs (denoted by C-QD_{113}) were obtained by hot injection of Cs-oleate at 90 °C with control of the OA and OLAM ligands. In general, small $CsPbBr_3$ QDs have high surface energies and a large number of defects, and hence they can be ripened easily, resulting in a PL redshift. Upon examining the colloidal stability of ISNCs that had been stored under an environment with relative humidity of 65% and room temperature of

25 °C, little change in emission peak and FWHM was observed over 120 days, and 90% of the initial PLQY was retained (Figure 4.6a). By contrast, the emission wavelength of the C-QD_{113} without Cs_4PbBr_6 rapidly redshifted, moving from 458 nm to 475 nm within 30 days, even at room temperature (Figure 4.6d). To compare in detail the thermal stability of the prepared QDs, they were dispersed in toluene and incubated for a period of time at 120 °C. The C-QD_{113} were easily ripened and fused together at high temperatures, and the emission gradually shifted to longer wavelengths, with a green emission at 500 nm observed after 60 min of incubation (Figure 4.6e). The XRD data showed that a nonluminescent $CsPb_2Br_5$ tetragonal phase was formed simultaneously (Figure 4.6f). In the case of the ISNCs, the intensity of the emission centered at approximately 510 nm increased slightly with time during the annealing process, but there was no shift in the position of the emission peak maximum and the blue emission was maintained with a slight decrease in PL intensity (Figure 4.6b). Furthermore, other crystal structures such as $CsPb_2Br_5$ were not generated, and the diffraction patterns indicated that the crystallinity of the ISNCs was improved (Figure 4.6c). These results clearly demonstrated that the Cs_4PbBr_6 effectively suppressed heat-induced aggregation and decomposition of small $CsPbBr_3$ QDs. These significant changes could be attributed to a reduction in surface energy via surface passivation. When comparing the water contact angles of ISNC and C-QD_{113} films, the contact angle of the ISNC film was 107.2°, i.e., greater than that of the C-QD_{113} film, which was 65.4° (Figure 4.7). The increased contact angle indicates a reduction in surface energy due to effective passivation of unsaturated atoms by hydrophobic ligands.[32,34]

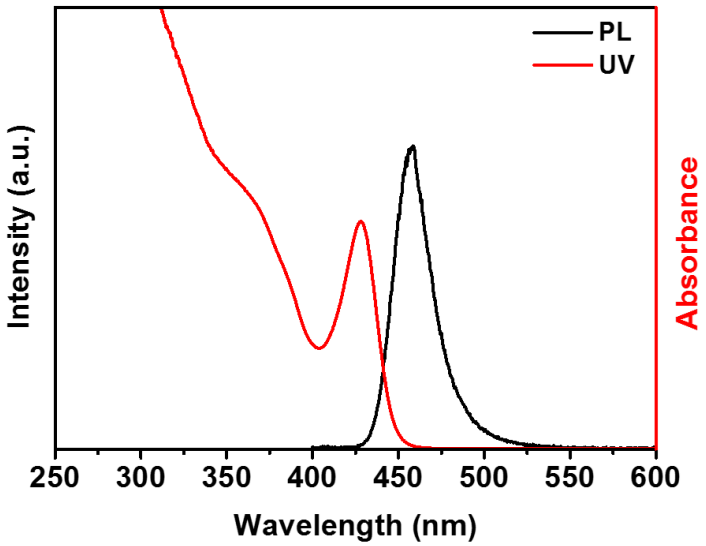

Figure 4.5. UV-vis absorption and PL spectra of conventional $CsPbBr_3$ quantum dots (C-QD_{113}).

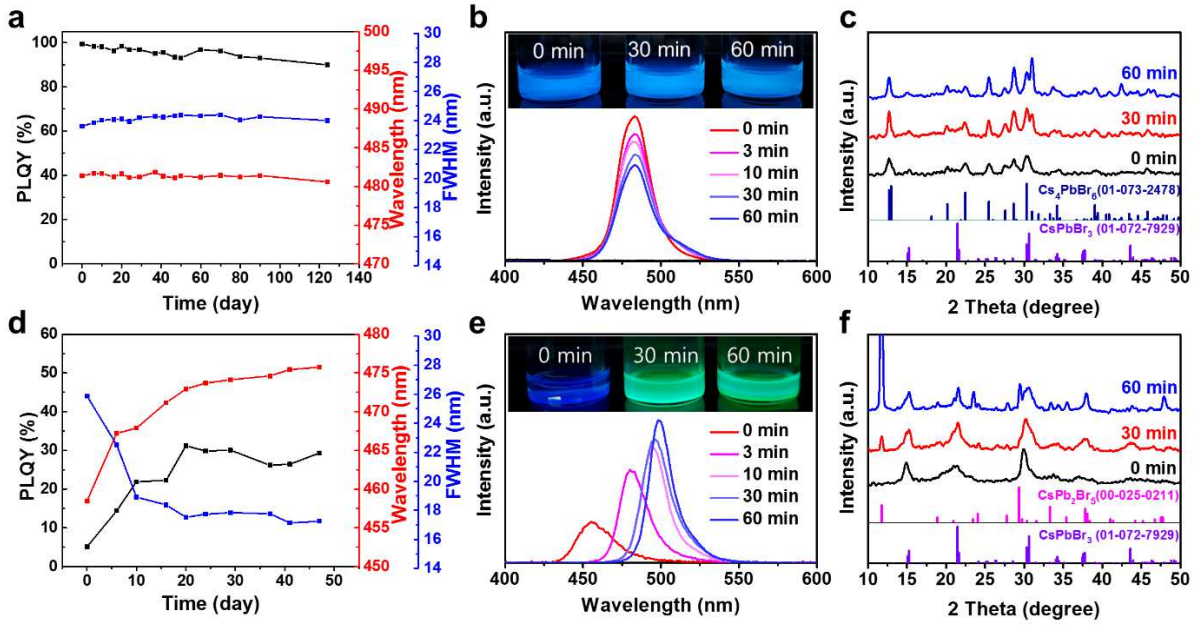

Figure 4.6. Stability of in situ generated perovskite NCs. Variations in emission wavelength, PLQY, and FWHM of (a) in situ generated $CsPbBr_3$-Cs_4PbBr_6 NCs (ISNCs) and (d) conventional $CsPbBr_3$ QDs (C-QD_{113}) with incubation time under ambient conditions (relative humidity: 65%, temperature: 25 °C). Emission stability of (b) ISNCs and (e) C-QD_{113} in toluene at 120 °C; the insets show photographs of the respective NCs acquired under UV light illumination. XRD patterns of (c) ISNCs and (f) C-QD_{113} after annealing in toluene at 120 °C over various periods of time.

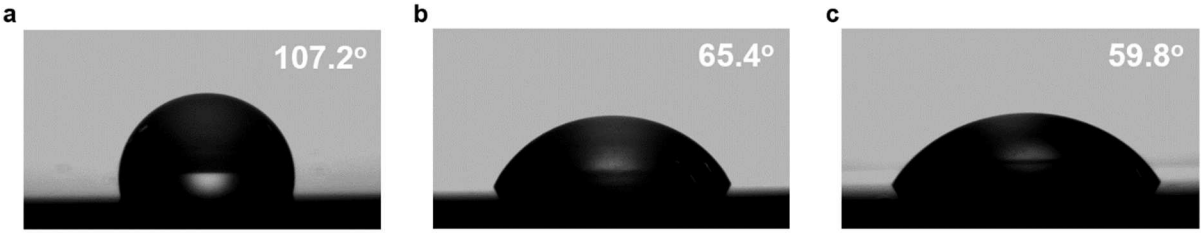

Figure 4.7. Water contact angles of (a) ISNCs, (b) C-QD_{113}, and (c) separated $CsPbBr_3$ QDs (S-QD_{113}) on SiO_2 wafer.

Effects of Cs_4PbBr_6 NCs on $CsPbBr_3$ QD quality

We hypothesized that the cause of the high PLQY and good thermal stability of the ISNCs was related to the presence of the Cs_4PbBr_6 NCs generated with the $CsPbBr_3$ QDs. To investigate the role of the Cs_4PbBr_6 NCs, we conducted a systematic study to monitor the differences in the optical properties, defect levels, and morphology of $CsPbBr_3$ QDs with different amounts of added Cs_4PbBr_6 NCs. For this purpose, non-luminescent pure Cs_4PbBr_6 NCs (denoted by NC_{416}) with diameters of 13.6 nm were prepared separately via a previously reported method (Figure 4.8).[49] $CsPbBr_3$ QDs were separated from a crude solution and then mixed with Cs_4PbBr_6 NCs in different weight ratios from 0 to 5 in a non-polar solvent. The separation of the $CsPbBr_3$ QDs from the crude solution involved extraction via a size selection process using methyl acetate as an anti-solvent; a clear emission spectrum peaking at 477 nm was observed for the separated $CsPbBr_3$ QDs. Because Cs_4PbBr_6 NCs and relatively large $CsPbBr_3$ QDs were removed during the separation process, the absorption peak at 313 nm disappeared, and the PL peak was slightly blue shifted. The XRD and TEM results for the $CsPbBr_3$ QD sample verified that the rhombohedral Cs_4PbBr_6 phase was not present and that the sample consisted entirely of $CsPbBr_3$ QDs of 4.3 nm in size (Figure 4.9).

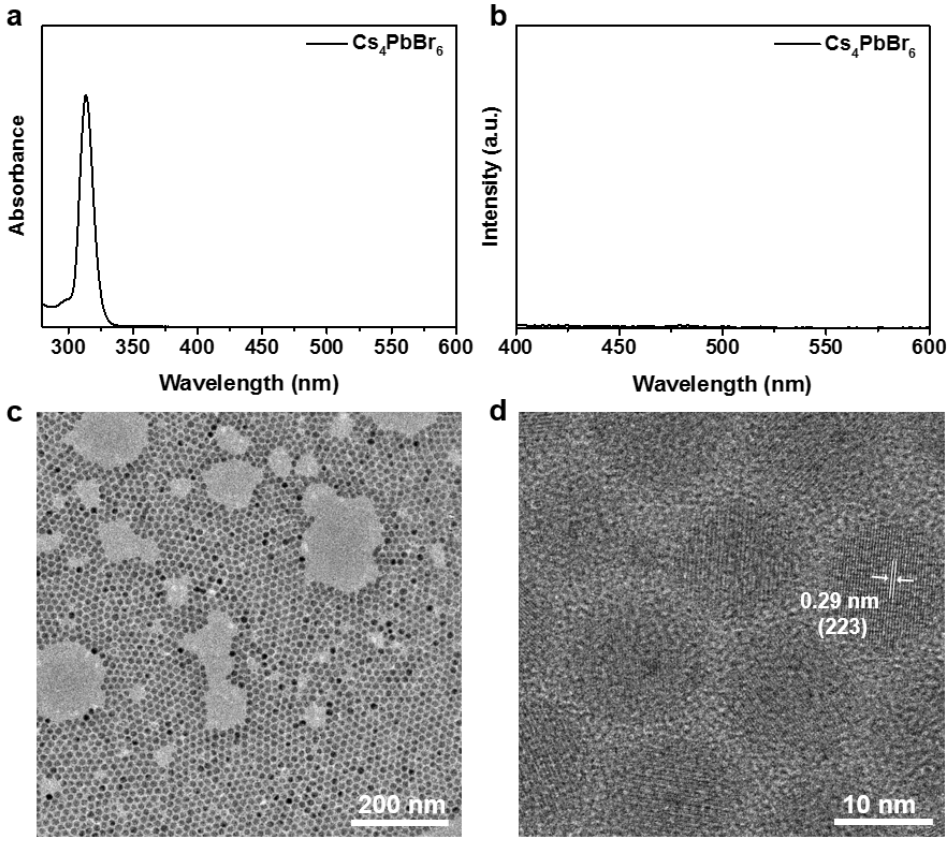

Figure 4.8. (a) UV-vis absorption spectrum, (b) PL spectrum, and (c,d) TEM images of pure Cs_4PbBr_6 NCs (NC_{416}).

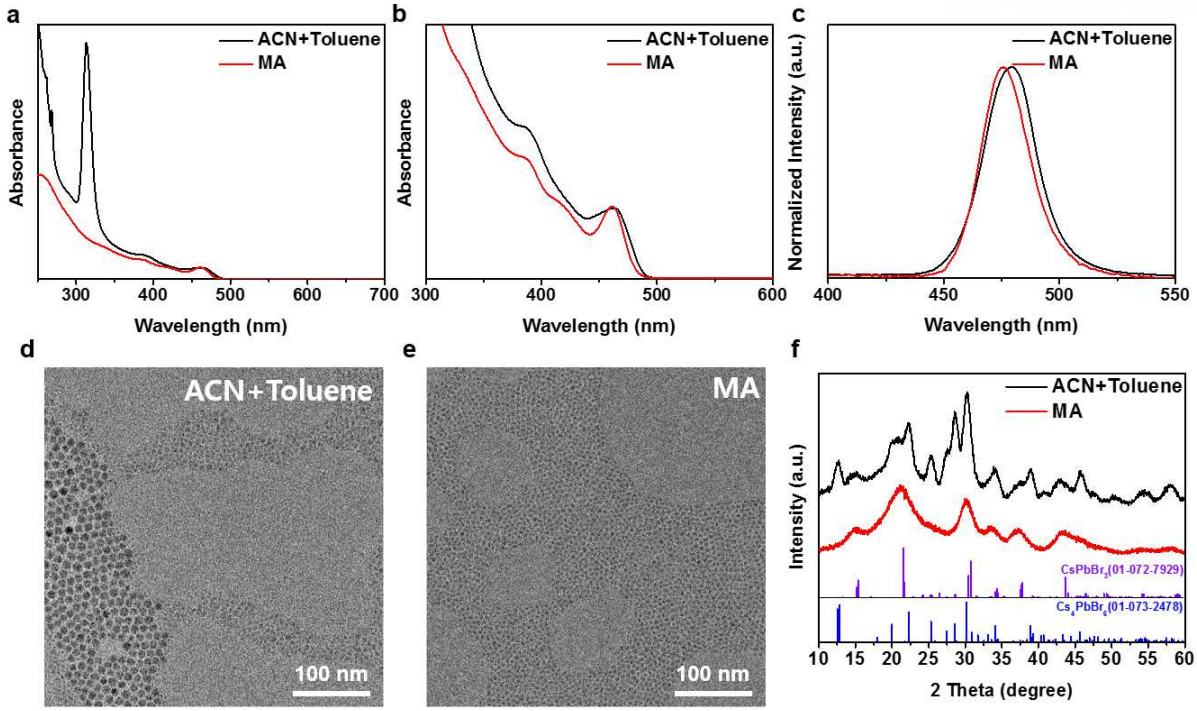

Figure 4.9. (a) UV-vis absorption spectra, (b) magnified view of the absorption spectra in the region 300-600 nm, and (c) Photoluminescence (PL) spectra of NCs washed with methyl acetate and the mixture of acetonitrile and toluene. TEM images of NCs washed with (d) the mixture of acetonitrile and toluene and (e) methyl acetate. (f) XRD patterns according to the washing method.

After mixing the separated $CsPbBr_3$ QDs (denoted by S-QD_{113}) and NC_{416} for 1 h at room temperature in a weight ratio of 1:0 to 1:5, changes in morphology and optical properties were observed in a non-polar solvent (Figure 4.10). As the relative NC_{416} amount was increased, the absorption intensity at 313 nm increased, while the first exciton peaks of S-QD_{113} gradually decreased in intensity and was blue-shifted. (Figure 10a). The emission peaks were also shifted to shorter wavelength, and the PL intensity was concomitantly improved. (Figure 4.10b and 4.11). In addition to the optical properties, changes in particle size and morphology were observed. In the 1:2 ratio mixed solution, the size of the S-QD_{113} decreased from 4.32 nm to 3.87 nm, while the NC_{416} size increased from 13.38 nm to 14.51 nm (Figure 4.10c and 4.12). The morphology of the NC_{416} transformed from hexagonal to truncated diamond and assembled into zig-zag shapes (Figure 4.13). The etching of S-QD_{113} and the variation in the NC_{416} shape are a result of the high surface energy of the small $CsPbBr_3$ QDs and the structural lability of perovskite as a function of its ligand environment. The $CsPbBr_3$ phase was successfully converted into the Cs_4PbBr_6 phase and vice versa using excess oleylamine (OLAM) and oleic acid (OA) in a previous study.[50] In our system, NC_{416} had a relative excess of the OLAM ligand, so small S-QD_{113} were easily etched and the NC_{416} size was increased (Figure 4.14).

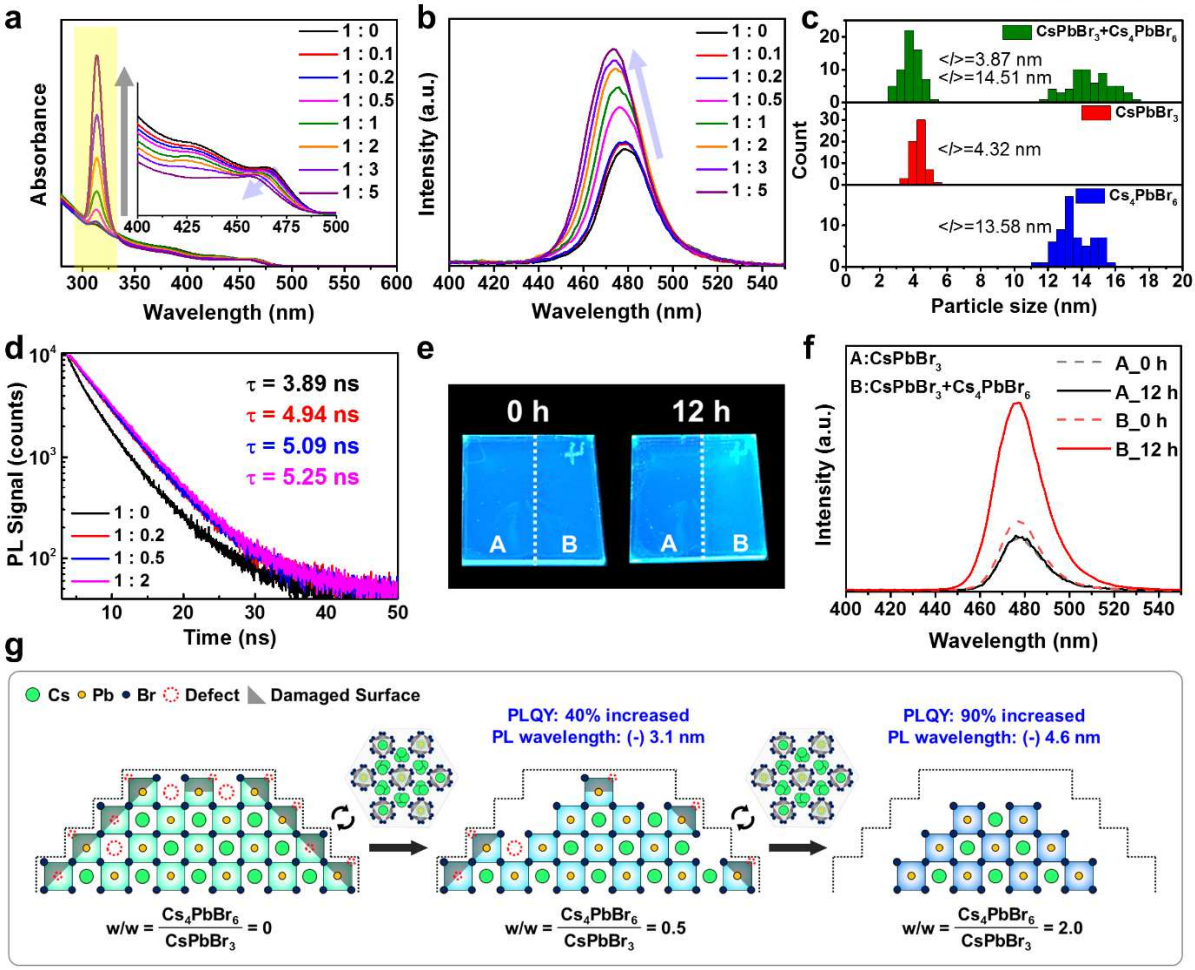

Figure 4.10. Characterization of the interaction between $CsPbBr_3$ QDs and Cs_4PbBr_6 NCs. (a) UV–vis absorption and (b) PL spectra for various ratios of separately prepared $CsPbBr_3$ QDs (S-QD_{113}) and Cs_4PbBr_6 NCs (NC_{416}). (c) NC size histograms before and after mixing S-QD_{113} and NC_{416} at a weight ratio of 1:2. (d) PL decay curves of S-QD_{113} and mixed S-QD_{113} and NC_{416}. (e) Photographs acquired under UV light illumination of the as-prepared sample (left) and the sample after storage for 12 h under ambient conditions (right). (f) PL spectra of film in part A and B of the sample slide after 0 h and 12 h. Part A of the film was coated with S-QD_{113} only and part B was sequentially coated with NC_{416} and then S-QD_{113}. (g) Schematics of S-QD_{113} surfaces produced by mixing S-QD_{113} and NC_{416} in weight ratios from 1:0 to 1:2. Imperfect octahedrons on the S-QD_{113} surface were peeled off upon addition of NC_{416}.

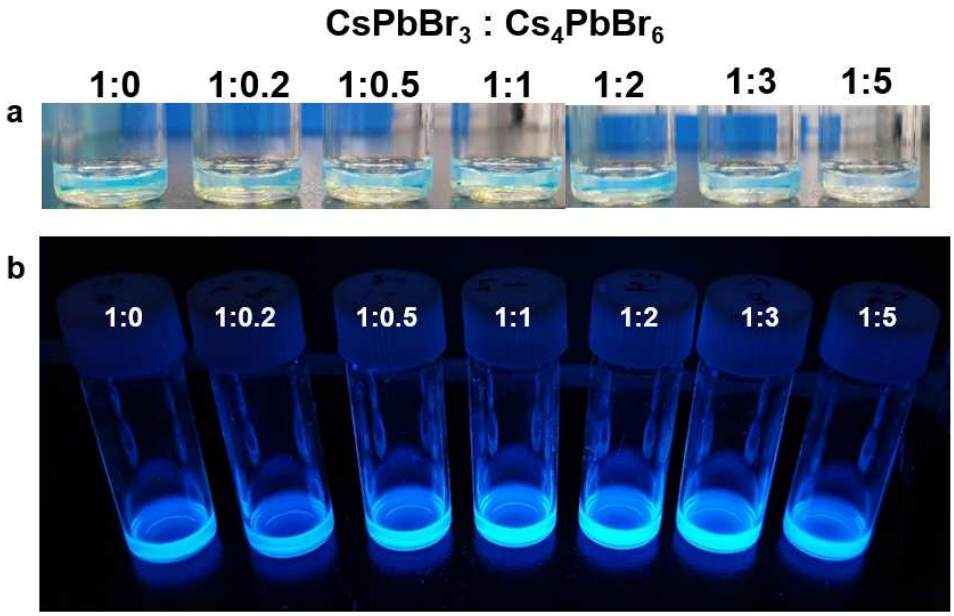

Figure 4.11. Photographs under (a) room light and (b) 365 nm UV light of the mixture according to the weight ratio of S-QD_{113} and NC_{416}.

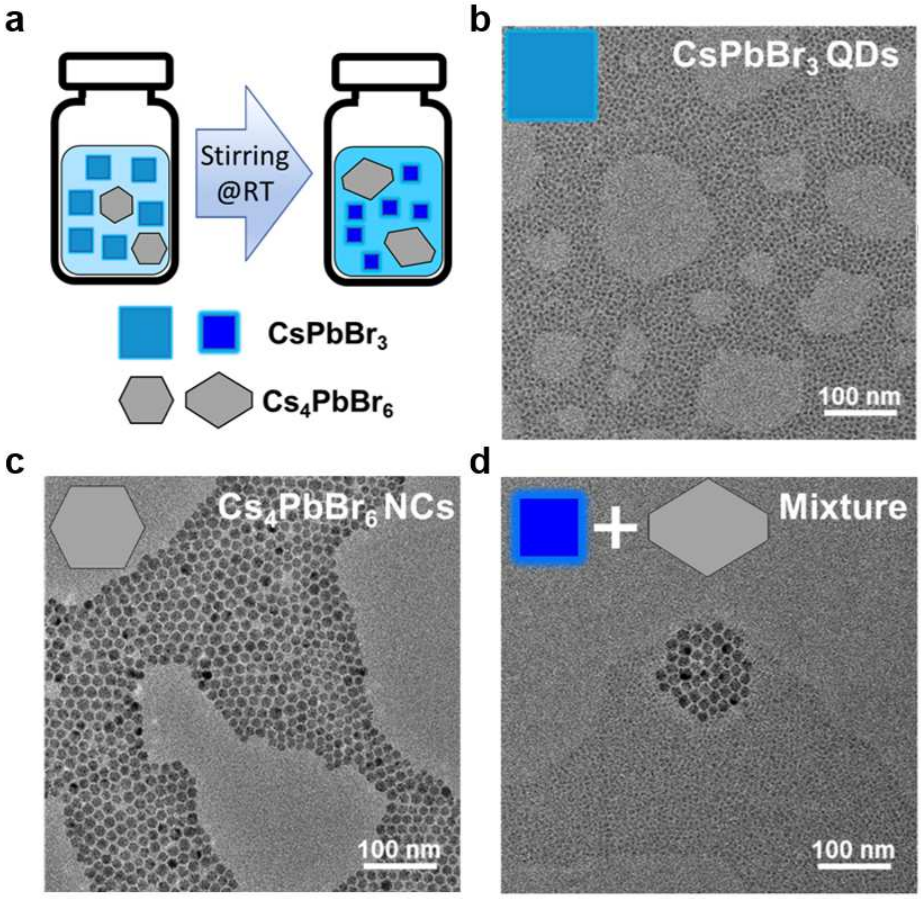

Figure 4.12. (a) The schematic illustration of the experiment mixing S-QD_{113} and NC_{416} at a weight ratio is 1:2. TEM images of (b) S-QD_{113}, (c) NC_{416}, and (d) mixed S-QD_{113} and NC_{416}.

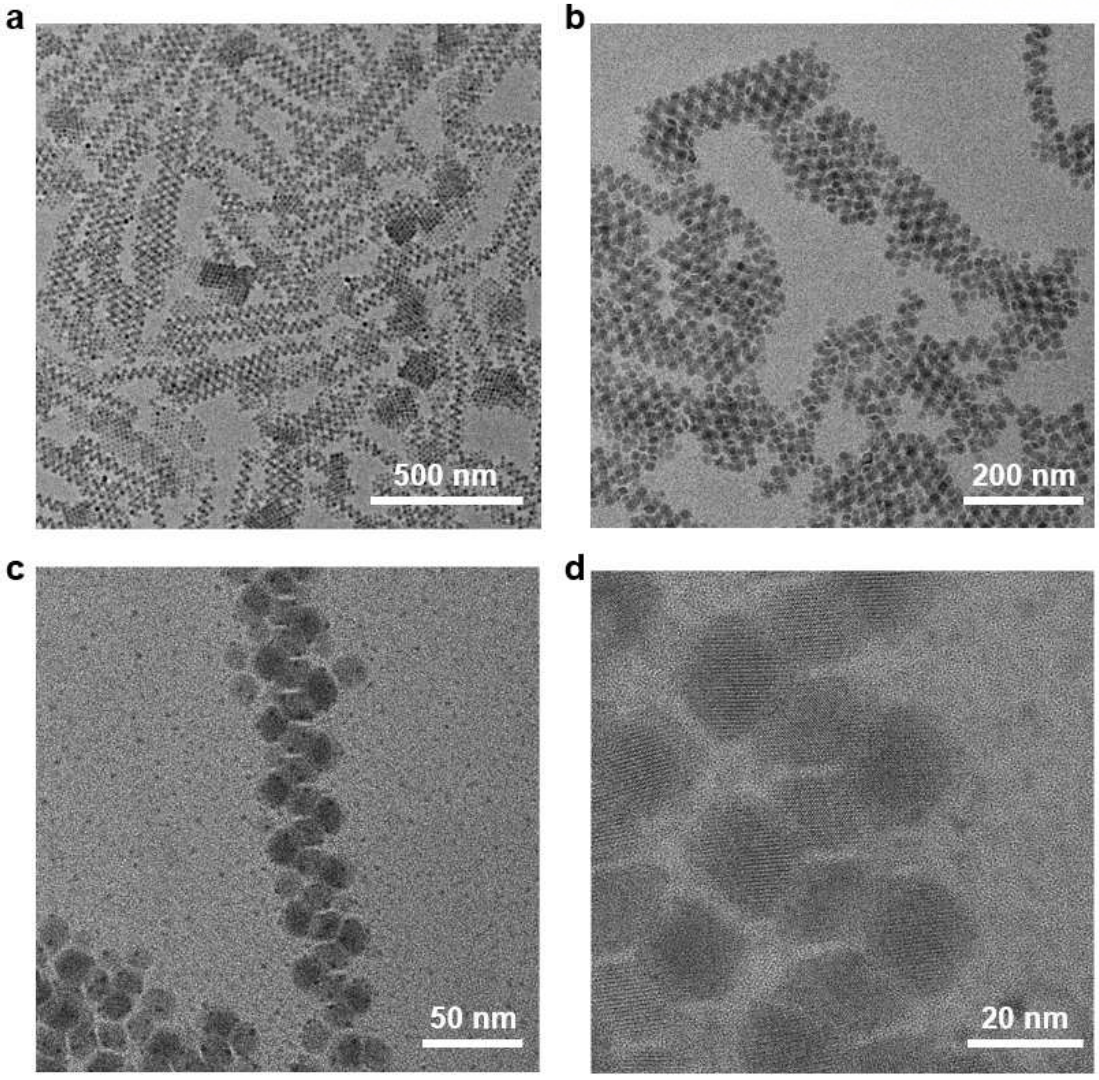

Figure 4.13. TEM images with different magnifications at (a) 13.5k, (b) 26.5k (c) 88k, and (d) 255k when S-QD_{113} and NC_{416} are mixed in a 1:2 weight ratio.

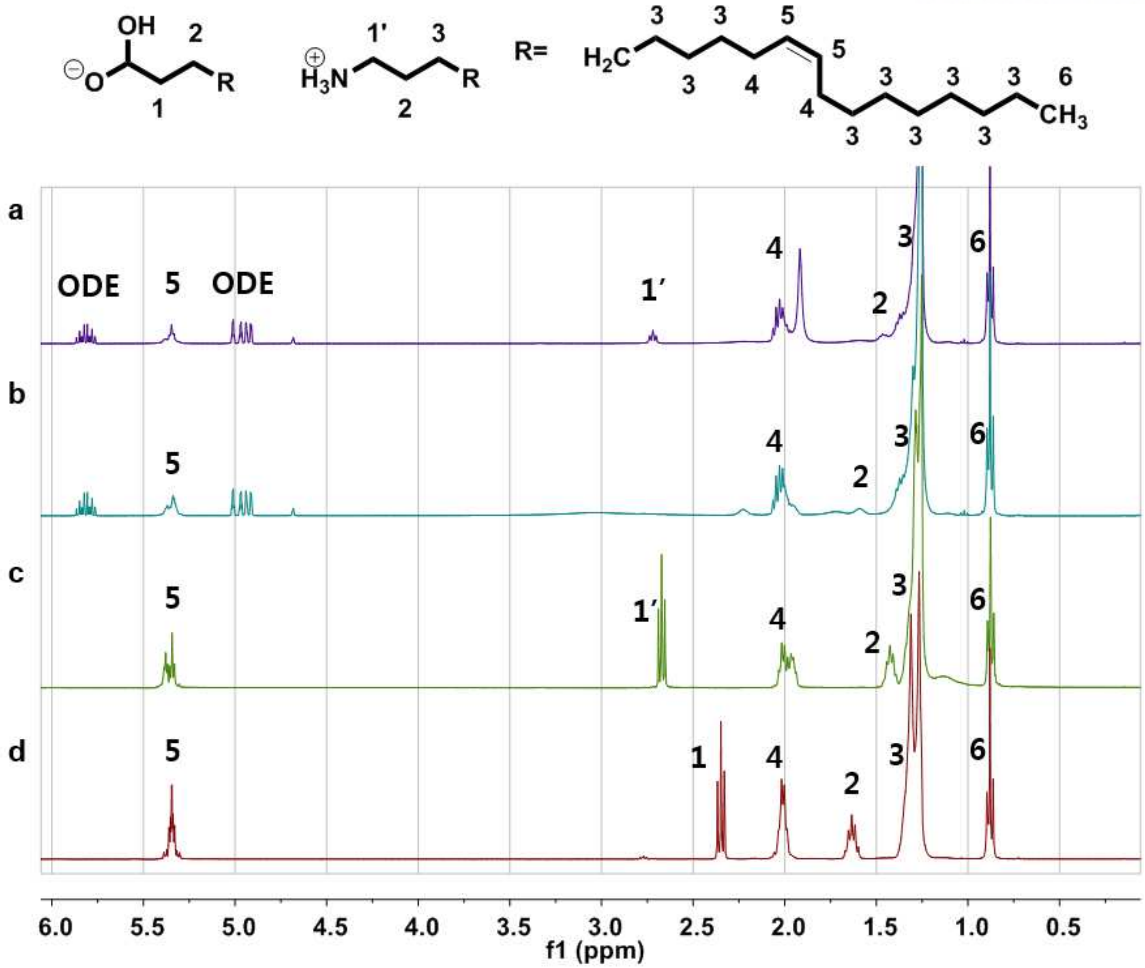

Figure 4.14. ^{1}H nuclear magnetic resonance spectra of (a) NC_{416}, (b) S-QD_{113}, (c) oleylamine, and (d) oleic acid dissolved in $CDCl_3$.

Time resolved photoluminescence (TRPL) measurements were performed to determine the effects of the PLQY enhancement along with NC etching on the optical spectroscopic characteristics (Figure 4.10d). Decay curves were used to analyze the excited state radiative relaxation dynamics. The S-QD_{113} decay curve was fitted to a biexponential function with a 3.89 ns average lifetime. When S-QD_{113} was mixed with NC_{416}, the decay curve of the resultant mixture fitted a monoexponential function well, and the average lifetime was gradually increased to 5.25 ns. This increment in the average lifetime could be a result of various effects, such as energy transfer between S-QD_{113} and NC_{416}, a S-QD_{113} size effect, and a reduction in trap-state density; hence, we decided to examine each of these possible causes in turn. First, Cs_4PbBr_6 NCs have a wider band gap than $CsPbBr_3$ NCs, so energy transfer is possible when the distance between the two materials is sufficiently close. Xuan *et al.* reported that the lifetime and PLQY were increased in a perovskite composite, in a study in which $CsPbBr_3$ NCs were embedded in Cs_4PbBr_6 NCs.[38] In addition, Chen *et al*. synthesized $CsPbBr_3$-embedded Cs_4PbBr_6 and analyzed the effect of metal halide interlayer in determining their photoluminescence excitation (PLE) properties.[51] To

investigate the energy transfer, we acquired PLE and PL spectra of S-QD$_{113}$ and ISNCs for various the excitation wavelengths (Figure 4.15). The S-QD$_{113}$ emission intensity gradually decreased as the excitation wavelength increased, in line with the trend observed for the PLE spectrum. The PLE spectrum of the ISNCs included a sharp drop centered at around 313 nm corresponding to the Cs_4PbBr_6 NC absorption peak. These results demonstrate that the origin of the PL of the ISNCs can be attributed to band edge emission of the $CsPbBr_3$ QDs rather than energy transfer from the Cs_4PbBr_6 NCs. In the latter case, the ISNC emission would have improved significantly before the Cs_4PbBr_6 NC absorption region. Therefore, we excluded the energy transfer effect in ISNCs. Second, for perovskites, lifetimes tend to decrease as band gaps widen.[52–55] Since S-QD$_{113}$ is in the strong quantum confinement regime, the lifetime is expected to decrease with the decrease in particle size. However, in our study, when NC$_{416}$ was mixed with S-QD$_{113}$, the size of the S-QD$_{113}$ particles decreased slightly because of surface etching. This result, indicating a longer lifetime for smaller NCs, was contrary to our expectation. Therefore, we conclude that surface passivation effects are likely to be the main reasons for the longer lifetime, as reported previously.[56,57] The Cs_4PbBr_6 NCs might promote the elimination of defects and radiative recombination in the $CsPbBr_3$ QDs.

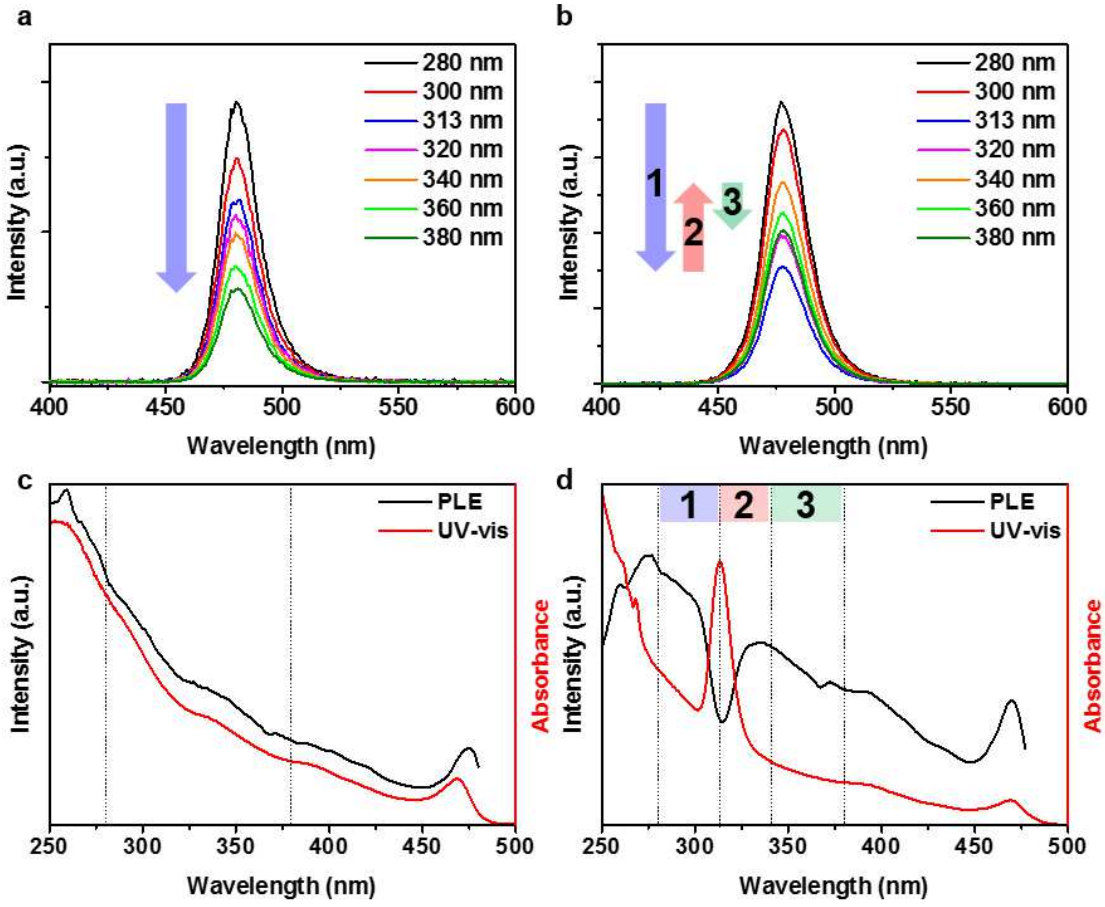

Figure 4.15. PL spectra of (a) S-QD$_{113}$ and (b) ISNCs as a function of excitation wavelength. UV-vis absorption and PL excitation spectra of (c) S-QD$_{113}$ and (d) ISNCs.

To investigate in detail the optical properties of the NCs, the temperature-dependent PL of the S-QD_{113} and ISNC samples was measured (Figure 4.16). The PL intensity of the S-QD_{113} sample gradually decreased as the temperature increased, in agreement with previous reports.[58–60] In metal halide perovskites, because of the low exciton binding energy, excitons are dissociated into free charge carriers by thermal energy, promoting nonradiative decay.[60–62] However, the ISNCs displayed a constant PL intensity, for the entire temperature range from 20 K to 300 K. As the exciton binding energies of NCs are highly dependent on the size of the NCs.[59,62] we expect the exciton binding energy of the S-QD_{113} (~4.32 nm) and ISNC (~4.33 nm) samples would be similar. Therefore, the constant ISNC PL intensity as a function of temperature suggests that nonradiative decay paths are substantially reduced by the presence of Cs_4PbBr_6.

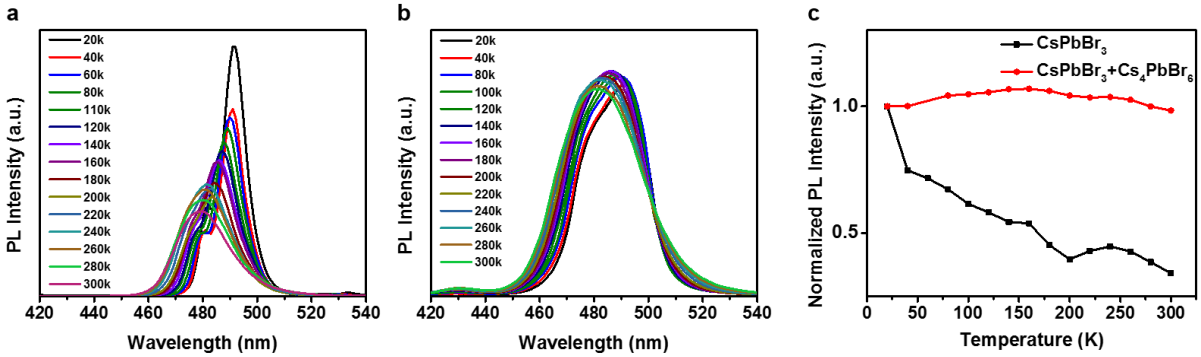

Figure 4.16. Temperature-dependent PL spectra of (a) S-QD_{113} and (b) ISNCs in the temperature range of 20-300k. (c) Normalized PL intensities of S-QD_{113} and ISNCs as a function of temperature.

In addition, we induced an interaction between the S-QD_{113} and NC_{416} samples on the substrate to identify the effects of defect passivation in the solid state. First, half of the substrate was covered with Kapton tape (3M #5413) and then NC_{416} was spin coated on the exposed part. Subsequently, the experiment proceeded in order with the removal of ligands with methyl acetate, peeling off the tape, and coating S-QD_{113} over the entire substrate. As a result, half of the substrate was covered with only S-QD_{113}, and the other coated with a double layer, with S-QD_{113} and NC_{416} in contact at the layer interface (Figure 4.17). For this as-prepared film, initially there was no difference in emission between the two regions (A and B); however, the PL intensity was greatly improved in the double layer (layer B) after 12 h (Figure 4.10e, f). Although the interaction was relatively slow in the solid state, the S-QD_{113} defects were also passivated similar to the solution. We summarized the above-described mechanistic findings in a schematic illustration (Figure 4.10g). Surface reconstruction takes place at the interfaces between the $CsPbBr_3$ QDs and Cs_4PbBr_6 NCs, and imperfect octahedrons on the $CsPbBr_3$ QD surfaces are reduced during the etching process. In this process, the $CsPbBr_3$ QD crystal size decreases, resulting in a blue shift of the emission wavelength, and the optical properties and colloidal stability are increased by the addition of Cs_4PbBr_6 NCs.

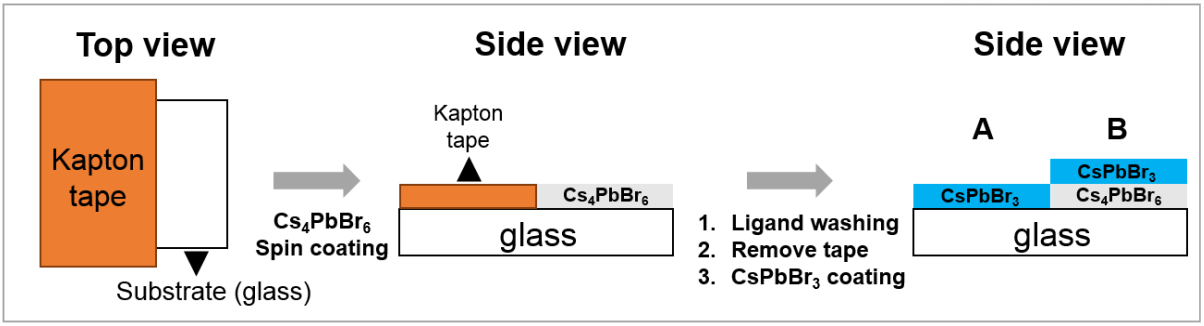

Figure 4.17. The schematic illustration of the mixing S-QD_{113} and NC_{416} in solid state.

Fabrication and characterization of blue perovskite LEDs

Encouraged by the high PLQY and stability of the ISNCs, we constructed LEDs with glass/indium tin oxide (ITO)/poly(3,4-ethylenedioxythiophene):poly(p-styrene sulfonate) (PEDOT:PSS)/ poly[(9,9-dioctylfluorenyl-2,7-diyl)-co-(4,4'-(N-(4-sec-butylphenyl)diphenylamine)] (TFB)+ poly(9-vinylcarbazole) (PVK) (30 nm)/ISNCs (20 nm)/ 2,2',2"-(1,3,5-benzinetriyl)-tris(1-phenyl-1-H-benzimidazole) (TPBi) (70 nm)/LiF (1 nm)/Al (100 nm) structures. The thickness of each layer was confirmed via the acquisition of cross-sectional scanning electron microscopy (SEM) images (Figure 4.18a). Energy band diagrams for the materials employed in the LEDs are shown in Figure 4.18b. Due to the low Cs_4PbBr_6 HOMO energy level (7.2 eV), a triple hole injection layer including a polymer with a deep work-function was used for efficient hole injection. The device performance characteristics of the ISNCs LEDs are shown in Figure 4.18c–f, Table 4.1. The LEDs fabricated with ISNCs exhibited a maximum luminance of 23 cd m^{-2} and EQE of 4.65% at wavelength of 480 nm. Histogram of maximum EQEs of ISNCs LEDs are shown in Figure 4.19.

One of the most important problems for blue-emitting metal halide perovskites is the spectral instability that results from halide segregation. LED emission spectra measured using various voltage bias values are shown in Figure 4.18e. Because the ISNCs exhibited blue emission at 480 nm without halide mixing, the ISNC LEDs exhibited stable electroluminescence (EL) emission spectra over the entire range of device operating voltages.

Table 4.1. Summary of device performance of ISNCs LEDs.

Conditions	L_{max} [cd m^{-2}] @bias	LE_{max} [cd A^{-1}] @bias	EQE_{max} [%] @bias	EQE_{avr} [%] from 12 devices
ITO/PEDOT:PSS/PVK+TFB/ISNCs /TPBi/LiF/Al	23 @ 5.2	5.10 @ 4.2	4.65 @ 4.2	3.13

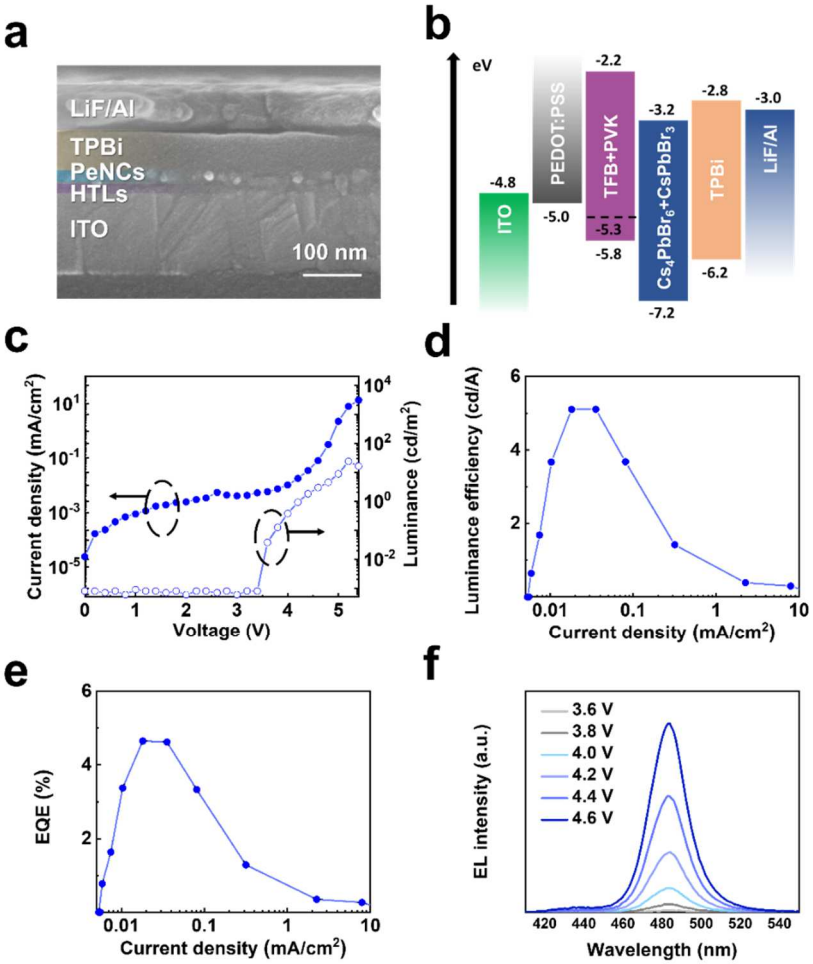

Figure 4.18. Blue perovskite LED device structure and performance characteristics. (a) Cross-sectional SEM image of ISNCs LED. (b) Energy band diagram of the materials employed in LEDs. (c) Current density–voltage (*J*–*V*) curve and luminance–voltage (*L*–*V*) curve, (d) luminous efficiency–current density (LE–*J*) curve, and (e) EQE–current density (EQE–*J*) curve of ISNCs LEDs. (f) EL spectra of ISNCs LEDs at various voltages.

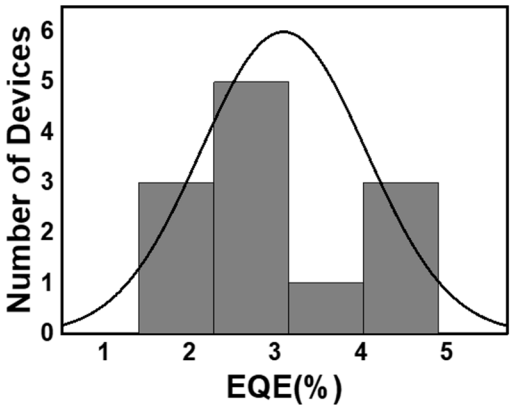

Figure 4.19. Histogram of maximum EQEs of ISNCs LEDs.

4.3 Conclusion

In summary, we demonstrated a novel synthetic method to simultaneously obtain ultra-small $CsPbBr_3$ QDs and Cs_4PbBr_6 NCs by controlling the ratio of the Cs- and Pb-precursors as well as the reaction temperature. $CsPbBr_3$ QDs of 3.5 nm and 4.3 nm in size – smaller than the exciton Bohr radius – were synthesized at 60 °C and 80 °C, respectively. These QDs emitted blue light at 470 nm and 477 nm, respectively, with high PLQYs of more than 90%. The Cs_4PbBr_6 NCs eliminated the imperfect octahedron defect sites on the surfaces of the $CsPbBr_3$ QDs, which resulted in suppression of nonradiative recombination; this was confirmed via TRPL and temperature-dependent PL measurements. In addition, the colloidal and thermal stabilities of the ISNCs were significantly enhanced by suppressing particle aggregation and fusion. We realized efficient blue LEDs with a maximum EQE of 4.65% at 480 nm. In particular, the EL spectra were stable across various applied voltages, without exhibiting any peak shifts. This surface defect etching method, which relied on $CsPbBr_3$ and Cs_4PbBr_6 phase surface reconstruction, was found to be effective even for solid-state films. Thus, our strategy could expand the development of a wide range of perovskite optoelectronic applications, including solar cells and NCs-based LEDs, thanks to the introduction of a new method for controlling the amount of defects.

4.4 Experimental section

Materials. Oleylamine (OLAM, 98%), hydrobromic acid (HBr, 48%), cesium carbonate (Cs_2CO_3, 99.9%), Lead oxide (PbO, 99.999%), 1-octadecene (ODE, 90%), oleic acid (OA, 90%), and lead bromide ($PbBr_2$, 98%) were purchased from Sigma-Aldrich. Acetonitrile (ACN, 99.5%), toluene (99.8%), methyl acetate (99.5%), and hexane (99.5%) were purchased from Samchun Chemicals. All the chemicals were used without further purification.

Preparation of OLAM-Br precursor. The OLAM-Br salt was synthesized according to a previous method with some modifications.[41] In a typical synthesis, OLAM (10 mL) and HBr solution (1.3 mL) were loaded into a 50 mL three-necked round-bottom flask, and the resulting solution was stirred under an Ar atmosphere at 120 °C for 2 h. Then, it was heated to 150 °C and left to react for an additional 30 min. After cooling the solution to 100 °C, it was vacuum dried for 1 h to remove any residual water. The precursor was collected in an Ar-filled vial and stored in a glove box for further use.

Synthesis of ISNCs. Mixed $CsPbBr_3$–Cs_4PbBr_6 NCs were prepared via an OLAM-Br precursor hot-injection method. Typically, Cs_2CO_3 (32.6 mg, 0.1 mmol), PbO (44.6 mg, 0.2 mmol), OA (1.0 mL), and ODE (10 mL) were stirred in a 50 mL three-necked round-bottom flask and degassed under vacuum at 120 °C for 1 h. After complete solubilization of the reaction mixture, the flask was filled with Ar and heated (or cooled) to obtain the desired temperature (60–160 °C). Then, the pre-heated OLAM-Br solution (0.9 mL) was swiftly injected into the reaction mixture. The reaction was quenched in an ice water bath after 30 min.

Purification of synthesized NCs. The crude solution was transferred to a 50 mL conical tube and ACN and toluene were then added to the solution in a volume ratio of 1:2:3 (crude mixture:ACN:toluene). The nanocrystals were precipitated in a centrifuge at 7000 rpm for 5 min. The supernatant was discarded, and the precipitate was collected and dissolved in hexane. One more centrifugation (7800 rpm, 5 min) was required to purify the NCs and obtain the final product. The clear supernatant was collected and used for future studies.

To eliminate the Cs_4PbBr_6 NCs from the crude solution, we used methyl acetate as an anti-solvent instead of the mixture of ACN and toluene. Typically, methyl acetate (5 mL) was added to the crude solution (5 mL). This solution was centrifuged at 7800 rpm for 5 min and the precipitate was discarded. An additional methyl acetate (20 mL) was added to the supernatant, and this mixture was centrifuged at 7800 rpm for 5 min. The precipitated $CsPbBr_3$ QDs (S-QD_{113}) were used in further studies after dispersion in hexane.

Synthesis of pure NC_{416}. Monodisperse Cs_4PbBr_6 NCs were synthesized according to a previously reported method.[49] The Cs-oleate precursor and NCs were prepared in air. For the Cs-oleate preparation, Cs_2CO_3 (0.4 g) and OA (8 mL) were loaded in a 20 mL vial and stirred on a hotplate at 150 °C for 20 min. In a typical synthesis, $PbBr_2$ (36.7 mg), OA (0.2 mL), OLAM (1.5 mL), and ODE (5 mL) were stirred at 150 °C until the solution became transparent. After cooling the solution to 80 °C, pre-heated Cs-oleate (0.75 mL) was swiftly injected into it. The reaction was quenched in an ice water bath after 3 min. The crude solution was washed via centrifugation (4500 rpm, 10 min), which was followed by redispersion in hexane.

Synthesis of C-QD_{113}. Small $CsPbBr_3$ QDs were synthesized according to a previously reported method with some modifications.[48] The synthetic approach was based on hot-injection of the Cs-oleate precursor. In brief, $PbBr_2$ (69 mg) and ODE (5 mL) were loaded in a 50 mL three-necked round-bottom flask and degassed under vacuum at 120 °C for 1 h. Dried OA (0.6 mL) and OLAM (0.3 mL) were injected to the reaction mixture at 120 °C under Ar. After complete solubilization of the reaction mixture, pre-heated Cs-oleate precursor (0.4 mL) was swiftly injected into the reaction mixture at 90 °C. The reaction was quenched in an ice water bath after 10 s. For Cs-oleate preparation, Cs_2CO_3 (0.4 g), OA (1.2 mL), and ODE (15 mL) were stirred in a 50 mL three-necked round-bottom flask and degassed under vacuum at 120 °C for 1 h. Then the solution was heated to 150 °C and reacted for an additional 30 min. The Cs-oleate precursor was preheated to 100 °C before use. Purification of the obtained QDs was achieved via the method mentioned above.

Preparation of ex situ mixed S-QD_{113} and NC_{416}. The solution was prepared by adding an amount of NC_{416} to S-QD_{113} (2 mg) to achieve the desired weight ratio in hexane (500 μL). After the addition of NC_{416}, it was observed that the PL intensity increased within a few seconds. To achieve a homogeneity, the mixture was stirred for 1 h at room temperature. It is worth noting that when the QD_{113}:NC_{416} weight ratio exceeded 1:10, the QD_{113} sample was completely etched and the emission was lost. To apply this system to the solid state, we used glass substrates, Kapton tape, QD_{113} (10 mg mL^{-1} in hexane), and NC_{416} (20 mg mL^{-1} in hexane). The glass substrates were first cleaned by sonification while sequentially immersed in deionized water, acetone, and isopropyl alcohol. Then, half of the glass was covered with Kapton tape, and NC_{416} was spin coated at 3,000 rpm for 1 min. To avoid dissolution of NC_{416} layer, methyl acetate was then spin coated on the slide twice at 3,000 rpm for 1 min. After peeling off the Kapton tape, S-QD_{113} was spin coated at 3,000 rpm for 1 min on the entire substrate.

Thermal stability test. After dissolving the NCs in toluene and adjusting the concentration to 10 mg mL^{-1}, we observed a change in the PL spectrum of the sample in a 120 °C oil bath as the time elapsed.

Device fabrication. ITO-patterned glass substrates were cleaned by sonification while sequentially immersed in deionized water, acetone, and isopropyl alcohol. The PEDOT:PSS layer was spin coated at 5,000 rpm for 40 s on the ITO substrates after 30 min of UV treatment. The slide was then transferred into a glove box and annealed at 140 °C for 10 min. TFB and PVK (volume ratio 1:1) were blended and dissolved in chlorobenzene such that the concentration of the mixture was 3 mg mL^{-1}. The TFB/PVK mixture solution was spin coated on the substrates (3,000 rpm, 40 s) and then annealed at 130 °C for 20 min. Perovskite NCs were then spin coated on the substrates (2,000 rpm, 30 s). Lastly, the slide was sequentially coated with TPBi (50 nm), LiF (1 nm), and Al (100 nm) by thermal evaporation.

Characterization. Absorption spectra were acquired by a Shimadzu UV-1800 UV–vis spectrometer. Photoluminescence (PL) spectroscopy was carried out and quantum yields were obtained for the NCs via the use of a quantum efficiency measurement system (Otsuka QE-2000). Photoluminescence emission (PLE) spectra were obtained by using an Agilent fluorescence spectrophotometer. X-ray diffraction (XRD) was performed by using a Rigaku Ultimate-IV X-ray diffractometer operated at 40 kV and 200 mA using the Cu K line (λ = 1.5418 A). Transmission electron microscopy (TEM) images were acquired by a JEOL JEM-2100 microscope with an acceleration voltage of 200 kV using copper grids (Ted Pella, USA). The particle sizes and distributions were measured using DigitalMicrograph software in TEM micrographs. Time resolved photoluminescence (TRPL) spectra were obtained by means of a time-correlated single-photon counting (TCSPC) setup (FluoTime 300, PicoQuant) at room temperature. ^{1}H nuclear magnetic resonance (^{1}H NMR) spectra were acquired using a Bruker AVANCE III HD (400 MHz) spectrometer. The residual proton signal of the deuterated solvent was selected as the reference standard. Temperature-dependent PL measurements were performed in the temperature range of 20–300 K using a liquid helium cooler. PL spectra of the nanocrystal films were obtained using the Agilent fluorescence spectrophotometer. Water contact angles were measured using a drop shape analyzer (DSA-100, Krüss). Cross-sectional scanning electron microscopy (SEM) images of the device structures were obtained using a Nova Nano230 FEI SEM (accelerating voltage 10 kV). To prevent the occurrence of charging, a 5 nm platinum layer was deposited on the samples via sputter coating (Emitech K575x, Tescan). The device performances of the encapsulated LEDs were measured using a Keithley 2400 sourcemeter and spectroradiometer (CS-2000, Konica Minolta) under ambient conditions.

4.5 References

(1) Lu, M.; Zhang, Y.; Wang, S.; Guo, J.; Yu, W. W.; Rogach, A. L. Metal Halide Perovskite Light-Emitting Devices: Promising Technology for Next-Generation Displays. *Adv. Funct. Mater.* **2019**, *29*, 1902008.

(2) Liu, X. K.; Xu, W.; Bai, S.; Jin, Y.; Wang, J.; Friend, R. H.; Gao, F. Metal Halide Perovskites for Light-Emitting Diodes. *Nat. Mater.* **2021**, *20*, 10-21.

(3) Chang, S.; Bai, Z.; Zhong, H. In Situ Fabricated Perovskite Nanocrystals: A Revolution in Optical Materials. *Advanced Optical Materials* **2018**, *6*, 1800380.

(4) Shen, Y.; Cheng, L. P.; Li, Y. Q.; Li, W.; Chen, J. D.; Lee, S. T.; Tang, J. X. High-Efficiency Perovskite Light-Emitting Diodes with Synergetic Outcoupling Enhancement. *Adv. Mater.* **2019**, *31*, 1901517.

(5) Lin, K.; Xing, J.; Quan, L. N.; de Arquer, F. P. G.; Gong, X.; Lu, J.; Xie, L.; Zhao, W.; Zhang, D.; Yan, C.; *et al*. Perovskite Light-Emitting Diodes with External Quantum Efficiency Exceeding 20 Per Cent. *Nature* **2018**, *562*, 245-248.

(6) Chiba, T.; Hayashi, Y.; Ebe, H.; Hoshi, K.; Sato, J.; Sato, S.; Pu, Y.-J.; Ohisa, S.; Kido, J. Anion-Exchange Red Perovskite Quantum Dots with Ammonium Iodine Salts for Highly Efficient Light-Emitting Devices. *Nat. Photonics* **2018**, *12*, 681-687.

(7) Cao, Y.; Wang, N.; Tian, H.; Guo, J.; Wei, Y.; Chen, H.; Miao, Y.; Zou, W.; Pan, K.; He, Y.; *et al*. Perovskite Light-Emitting Diodes Based on Spontaneously Formed Submicrometre-Scale Structures. *Nature* **2018**, *562*, 249-253.

(8) Xu, W.; Hu, Q.; Bai, S.; Bao, C.; Miao, Y.; Yuan, Z.; Borzda, T.; Barker, A. J.; Tyukalova, E.; Hu, Z.; *et al*. Rational Molecular Passivation for High-Performance Perovskite Light-Emitting Diodes. *Nat. Photonics* **2019**, *13*, 418-424.

(9) Dong, Y.; Wang, Y. K.; Yuan, F.; Johnston, A.; Liu, Y.; Ma, D.; Choi, M. J.; Chen, B.; Chekini, M.; Baek, S. W.; *et al*. Bipolar-Shell Resurfacing for Blue LEDs Based on Strongly Confined Perovskite Quantum Dots. *Nat. Nanotechnol.* **2020**, *15*, 668-674.

(10) Wang, C.; Han, D.; Wang, J.; Yang, Y.; Liu, X.; Huang, S.; Zhang, X.; Chang, S.; Wu, K.; Zhong, H. Dimension Control of In Situ Fabricated $CsPbClBr_2$ Nanocrystal Films Toward Efficient Blue Light-Emitting Diodes. *Nat. Commun.* **2020**, *11*, 6428.

(11) Yong, Z. J.; Guo, S. Q.; Ma, J. P.; Zhang, J. Y.; Li, Z. Y.; Chen, Y. M.; Zhang, B. B.; Zhou, Y.; Shu, J.; Gu, J. L.; *et al*. Doping-Enhanced Short-Range Order of Perovskite Nanocrystals for Near-Unity Violet Luminescence Quantum Yield. *J. Am. Chem. Soc.* **2018**, *140*, 9942-9951.

(12) Sun, C.; Gao, Z. Y.; Liu, H. X.; Wang, L.; Deng, Y. C.; Li, P.; Li, H. R.; Zhang, Z. H.; Fan, C.; Bi, W. G. One Stone, Two Birds: High-Efficiency Blue-Emitting Perovskite Nanocrystals for LED and Security Ink Applications. *Chem. Mater.* **2019**, *31*, 5116-5123.

(13) Hou, S.; Gangishetty, M. K.; Quan, Q.; Congreve, D. N. Efficient Blue and White Perovskite Light-Emitting Diodes via Manganese Doping. *Joule* **2018**, *2*, 2421-2433.

(14) Gangishetty, M. K.; Hou, S.; Quan, Q.; Congreve, D. N. Reducing Architecture Limitations for Efficient Blue Perovskite Light-Emitting Diodes. *Adv. Mater.* **2018**, *30*, 1706226.

(15) Pan, G.; Bai, X.; Xu, W.; Chen, X.; Zhai, Y.; Zhu, J.; Shao, H.; Ding, N.; Xu, L.; Dong, B.; *et al*. Bright Blue Light Emission of Ni(2+) Ion-Doped $CsPbCl_xBr_{3-x}$ Perovskite Quantum Dots Enabling Efficient Light-Emitting Devices. *ACS Appl. Mater. Interfaces* **2020**, *12*, 14195-14202.

(16) Bi, C.; Wang, S.; Li, Q.; Kershaw, S. V.; Tian, J.; Rogach, A. L. Thermally Stable Copper(II)-Doped Cesium Lead Halide Perovskite Quantum Dots with Strong Blue Emission. *J. Phys. Chem. Lett.* **2019**, *10*, 943-952.

(17) Yang, F.; Chen, H.; Zhang, R.; Liu, X.; Zhang, W.; Zhang, J.; Gao, F.; Wang, L. Efficient and Spectrally Stable Blue Perovskite Light-Emitting Diodes Based on Potassium Passivated Nanocrystals. *Adv. Funct. Mater.* **2020**, *30*, 1908760.

(18) Ahmed, G. H.; El-Demellawi, J. K.; Yin, J.; Pan, J.; Velusamy, D. B.; Hedhili, M. N.; Alarousu, E.; Bakr, O. M.; Alshareef, H. N.; Mohammed, O. F. Giant Photoluminescence Enhancement in $CsPbCl_3$ Perovskite Nanocrystals by Simultaneous Dual-Surface Passivation. *ACS Energy Lett.* **2018**, *3*, 2301-2307.

(19) Wu, Y.; Li, X.; Zeng, H. Highly Luminescent and Stable Halide Perovskite Nanocrystals. *ACS Energy Lett.* **2019**, *4*, 673-681.

(20) Nenon, D. P.; Pressler, K.; Kang, J.; Koscher, B. A.; Olshansky, J. H.; Osowiecki, W. T.; Koc, M. A.; Wang, L. W.; Alivisatos, A. P. Design Principles for Trap-Free $CsPbX_3$ Nanocrystals: Enumerating and Eliminating Surface Halide Vacancies with Softer Lewis Bases. *J. Am. Chem. Soc.* **2018**, *140*, 17760-17772.

(21) Zhang, H.; Fu, X.; Tang, Y.; Wang, H.; Zhang, C.; Yu, W. W.; Wang, X.; Zhang, Y.; Xiao, M. Phase Segregation Due to Ion Migration in All-Inorganic Mixed-Halide Perovskite Nanocrystals. *Nat. Commun* **2019**, *10*, 1088.

(22) Li, G.; Rivarola, F. W.; Davis, N. J.; Bai, S.; Jellicoe, T. C.; de la Pena, F.; Hou, S.; Ducati, C.; Gao, F.; Friend, R. H.; *et al*. Highly Efficient Perovskite Nanocrystal Light-Emitting Diodes Enabled by a Universal Crosslinking Method. *Adv Mater* **2016**, *28*, 3528-3534.

(23) Bekenstein, Y.; Koscher, B. A.; Eaton, S. W.; Yang, P.; Alivisatos, A. P. Highly Luminescent Colloidal Nanoplates of Perovskite Cesium Lead Halide and Their Oriented Assemblies. *J. Am. Chem. Soc.* **2015**, *137*, 16008-16011.

(24) Bertolotti, F.; Nedelcu, G.; Vivani, A.; Cervellino, A.; Masciocchi, N.; Guagliardi, A.; Kovalenko, M. V. Crystal Structure, Morphology, and Surface Termination of Cyan-Emissive, Six-Monolayers-Thick $CsPbBr_3$ Nanoplatelets from X-ray Total Scattering. *ACS Nano* **2019**, *13*, 14294-14307.

(25) Bohn, B. J.; Tong, Y.; Gramlich, M.; Lai, M. L.; Doblinger, M.; Wang, K.; Hoye, R. L. Z.; Muller-Buschbaum, P.; Stranks, S. D.; Urban, A. S.; *et al*. Boosting Tunable Blue Luminescence of Halide Perovskite Nanoplatelets through Postsynthetic Surface Trap Repair. *Nano Lett.* **2018**, *18*, 5231-5238.

(26) Hoye, R. L. Z.; Lai, M. L.; Anaya, M.; Tong, Y.; Galkowski, K.; Doherty, T.; Li, W.; Huq, T. N.; Mackowski, S.; Polavarapu, L.; *et al*. Identifying and Reducing Interfacial Losses to Enhance Color-Pure Electroluminescence in Blue-Emitting Perovskite Nanoplatelet Light-Emitting Diodes. *ACS Energy Lett.* **2019**, *4*, 1181-1188.

(27) Wu, Y.; Wei, C.; Li, X.; Li, Y.; Qiu, S.; Shen, W.; Cai, B.; Sun, Z.; Yang, D.; Deng, Z.; *et al*. In Situ Passivation of PbBr64– Octahedra toward Blue Luminescent $CsPbBr_3$ Nanoplatelets with Near 100% Absolute Quantum Yield. *ACS Energy Lett.* **2018**, *3*, 2030-2037.

(28) Ni, L. M.; Huynh, U.; Cheminal, A.; Thomas, T. H.; Shivanna, R.; Hinrichsen, T. F.; Ahmad, S.; Sadhanala, A.; Rao, A. Real-Time Observation of Exciton-Phonon Coupling Dynamics in Self-Assembled Hybrid Perovskite Quantum Wells. *ACS Nano* **2017**, *11*, 10834-10843.

(29) Dong, Y.; Qiao, T.; Kim, D.; Parobek, D.; Rossi, D.; Son, D. H. Precise Control of Quantum Confinement in Cesium Lead Halide Perovskite Quantum Dots via Thermodynamic Equilibrium. *Nano Lett.* **2018**, *18*, 3716-3722.

(30) Shao, H.; Bai, X.; Pan, G.; Cui, H.; Zhu, J.; Zhai, Y.; Liu, J.; Dong, B.; Xu, L.; Song, H. Highly Efficient and Stable Blue-Emitting $CsPbBr_3$@SiO_2 Nanospheres Through Low Temperature Synthesis for Nanoprinting and WLED. *Nanotechnology* **2018**, *29*, 285706.

(31) Wang, S. X.; Bi, C. H.; Yuan, J. F.; Zhang, L. X.; Tian, J. J. Original Core-Shell Structure of Cubic $CsPbBr_3$@Amorphous $CsPbBr_x$ Perovskite Quantum Dots with a High Blue Photoluminescence Quantum Yield of over 80%. *ACS Energy Lett.* **2018**, *3*, 245-251.

(32) Zhang, X. T.; Wang, H.; Hu, Y.; Pei, Y. X.; Wang, S. X.; Shi, Z. F.; Colvin, V. L.; Wang, S. N.; Zhang, Y.; Yu, W. W. Strong Blue Emission from Sb^{3+}-Doped Super Small $CsPbBr_3$ Nanocrystals. *J. Phys. Chem. Lett.* **2019**, *10*, 1750-1756.

(33) Li, J.; Gan, L.; Fang, Z.; He, H.; Ye, Z. Bright Tail States in Blue-Emitting Ultrasmall Perovskite Quantum Dots. *J. Phys. Chem. Lett.* **2017**, *8*, 6002-6008.

(34) Bi, C.; Yao, Z.; Sun, X.; Wei, X.; Wang, J.; Tian, J. Perovskite Quantum Dots with Ultralow Trap Density by Acid Etching-Driven Ligand Exchange for High Luminance and Stable Pure-Blue Light-Emitting Diodes. *Adv Mater* **2021**, *33*, 2006722.

(35) Chen, Y. M.; Zhou, Y.; Zhao, Q.; Zhang, J. Y.; Ma, J. P.; Xuan, T. T.; Guo, S. Q.; Yong, Z. J.; Wang, J.; Kuroiwa, Y.; *et al*. Cs_4PbBr_6/$CsPbBr_3$ Perovskite Composites with Near-Unity Luminescence Quantum Yield: Large-Scale Synthesis, Luminescence and Formation Mechanism, and White Light-Emitting Diode Application. *ACS Appl. Mater. Interfaces* **2018**, *10*, 15905-15912.

(36) Wang, Q.; Wu, W.; Wu, R.; Yang, S.; Wang, Y.; Wang, J.; Chai, Z.; Han, Q. Improved Thermal Stability of Photoluminescence in Cs_4PbBr_6 Microcrystals/$CsPbBr_3$ Nanocrystals. *J. Colloid Interface Sci.* **2019**, *554*, 133-141.

(37) Xu, L.; Li, J.; Fang, T.; Zhao, Y.; Yuan, S.; Dong, Y.; Song, J. Synthesis of Stable and Phase-Adjustable $CsPbBr_3$@Cs_4PbBr_6 Nanocrystals via Novel Anion–Cation Reactions. *Nanoscale Adv.* **2019**, *1*, 980-988.

(38) Xuan, T.; Lou, S.; Huang, J.; Cao, L.; Yang, X.; Li, H.; Wang, J. Monodisperse and Brightly Luminescent $CsPbBr_3$/Cs_4PbBr_6 Perovskite Composite Nanocrystals. *Nanoscale* **2018**, *10*, 9840-9844.

(39) Jung, Y. K.; Calbo, J.; Park, J. S.; Whalley, L. D.; Kim, S.; Walsh, A. Intrinsic Doping Limit and Defect-Assisted Luminescence in Cs_4PbBr_6. *J. Mater. Chem. A* **2019**, *7*, 20254-20261.

(40) Shin, M.; Nam, S. W.; Sadhanala, A.; Shivanna, R.; Anaya, M.; Jimenez-Solano, A.; Yoon, H.; Jeon, S.; Stranks, S. D.; Hoye, R. L. Z.; *et al*. Understanding the Origin of Ultrasharp Sub-bandgap Luminescence from Zero-Dimensional Inorganic Perovskite Cs_4PbBr_6. *Acs Appl Energ Mater* **2020**, *3*, 192-199.

(41) Dutta, A.; Behera, R. K.; Pal, P.; Baitalik, S.; Pradhan, N. Near-Unity Photoluminescence Quantum Efficiency for All $CsPbX_3$ (X=Cl, Br, and I) Perovskite Nanocrystals: A Generic Synthesis Approach. *Angew. Chem. Int. Ed.* **2019**, *58*, 5552-5556.

(42) Jing, Q.; Xu, Y.; Su, Y. C.; Xing, X.; Lu, Z. D. A systematic study of the synthesis of cesium lead halide nanocrystals: does Cs_4PbBr_6 or $CsPbBr_3$ form? *Nanoscale* **2019**, *11*, 1784-1789.

(43) Liu, Z. K.; Bekenstein, Y.; Ye, X. C.; Nguyen, S. C.; Swabeck, J.; Zhang, D. D.; Lee, S. T.; Yang, P. D.; Ma, W. L.; Alivisatos, A. P. Ligand Mediated Transformation of Cesium Lead Bromide Perovskite Nanocrystals to Lead Depleted Cs_4PbBr_6 Nanocrystals. *J. Am. Chem. Soc.* **2017**, *139*, 5309-5312.

(44) Babin, V.; Fabeni, P.; Mihokova, E.; Nikl, M.; Pazzi, G. P.; Zazubovich, N.; Zazubovich, S. Luminescence of Cs_4PbBr_6 Aggregates in As-Grown and in Annealed CsBr:Pb Single Crystals. *physica status solidi (b)* **2000**, *219*, 205-214.

(45) Kondo, S.; Amaya, K.; Saito, T. Localized Optical Absorption in Cs_4PbBr_6. *J. Phys.: Condens. Matter* **2002**, *14*, 2093-2099.

(46) Nikl, M.; Mihokova, E.; Nitsch, K.; Somma, F.; Giampaolo, C.; Pazzi, G. P.; Fabeni, P.; Zazubovich, S. Photoluminescence of Cs_4PbBr_6 Crystals and Thin Films. *Chem. Phys. Lett.* **1999**, *306*, 280-284.

(47) Protesescu, L.; Yakunin, S.; Bodnarchuk, M. I.; Krieg, F.; Caputo, R.; Hendon, C. H.; Yang, R. X.; Walsh, A.; Kovalenko, M. V. Nanocrystals of Cesium Lead Halide Perovskites (CsPbX(3), X = Cl, Br, and I): Novel Optoelectronic Materials Showing Bright Emission with Wide Color Gamut. *Nano Lett.* **2015**, *15*, 3692-3696.

(48) Liang, Z. Q.; Zhao, S. L.; Xu, Z.; Qiao, B.; Song, P. J.; Gao, D.; Xu, X. R. Shape-Controlled Synthesis of All-Inorganic $CsPbBr_3$ Perovskite Nanocrystals with Bright Blue Emission. *ACS Appl. Mater. Interfaces* **2016**, *8*, 28824-28830.

(49) Akkerman, Q. A.; Park, S.; Radicchi, E.; Nunzi, F.; Mosconi, E.; De Angelis, F.; Brescia, R.; Rastogi, P.; Prato, M.; Manna, L. Nearly Monodisperse Insulator Cs_4PbX_6 (X = Cl, Br, I) Nanocrystals, Their Mixed Halide Compositions, and Their Transformation into $CsPbX_3$ Nanocrystals. *Nano Lett.* **2017**, *17*, 1924-1930.

(50) Udayabhaskararao, T.; Houben, L.; Cohen, H.; Menahem, M.; Pinkas, I.; Avram, L.; Wolf, T.; Teitelboim, A.; Leskes, M.; Yaffe, O.; *et al*. A Mechanistic Study of Phase Transformation in Perovskite Nanocrystals Driven by Ligand Passivation. *Chem. Mater.* **2018**, *30*, 84-93.

(51) Chen, X.; He, M.; Huang, S.; Zhang, L.; Zhong, H. Interlayer Determined Photoluminescence Excitation Properties of Cs-Rich and Pb-Rich Cs4PbBr6 Samples. *The Journal of Physical Chemistry C* **2021**, *125*, 16103-16109.

(52) Li, X.; Wu, Y.; Zhang, S.; Cai, B.; Gu, Y.; Song, J.; Zeng, H. $CsPbX_3$ Quantum Dots for Lighting and Displays: Room-Temperature Synthesis, Photoluminescence Superiorities, Underlying Origins and White Light-Emitting Diodes. *Adv. Funct. Mater.* **2016**, *26*, 2435-2445.

(53) Makarov, N. S.; Guo, S.; Isaienko, O.; Liu, W.; Robel, I.; Klimov, V. I. Spectral and Dynamical Properties of Single Excitons, Biexcitons, and Trions in Cesium-Lead-Halide Perovskite Quantum Dots. *Nano Lett.* **2016**, *16*, 2349-2362.

(54) Diroll, B. T.; Zhou, H.; Schaller, R. D. Low-Temperature Absorption, Photoluminescence, and Lifetime of $CsPbX_3$ (X = Cl, Br, I) Nanocrystals. *Adv. Funct. Mater.* **2018**, *28*, 1800945.

(55) Naghadeh, S. B.; Luo, B.; Pu, Y.-C.; Schwartz, Z.; Hollingsworth, W. R.; Lindley, S. A.; Brewer, A. S.; Ayzner, A. L.; Zhang, J. Z. Size Dependence of Charge Carrier Dynamics in Organometal Halide Perovskite Nanocrystals: Deciphering Radiative Versus Nonradiative Components. *The Journal of Physical Chemistry C* **2019**, *123*, 4610-4619.

(56) Koscher, B. A.; Swabeck, J. K.; Bronstein, N. D.; Alivisatos, A. P. Essentially Trap-Free $CsPbBr_3$ Colloidal Nanocrystals by Postsynthetic Thiocyanate Surface Treatment. *J. Am. Chem. Soc.* **2017**, *139*, 6566-6569.

(57) Ahmed, T.; Seth, S.; Samanta, A. Boosting the Photoluminescence of $CsPbX_3$ (X = Cl, Br, I) Perovskite Nanocrystals Covering a Wide Wavelength Range by Postsynthetic Treatment with Tetrafluoroborate Salts. *Chem. Mater.* **2018**, *30*, 3633-3637.

(58) Wang, R. Z.; Hu, S.; Yang, X.; Yan, X. L.; Li, H.; Sheng, C. X. Circularly Polarized Photoluminescence and Hanle Effect Measurements of Spin Relaxation in Organic-Inorganic Hybrid Perovskite Films. *J. Mater. Chem. C* **2018**, *6*, 2989-2995.

(59) Wang, Q.; Liu, X.-D.; Qiu, Y.-H.; Chen, K.; Zhou, L.; Wang, Q.-Q. Quantum Confinement Effect and Exciton Binding Energy of Layered Perovskite Nanoplatelets. *AIP Adv.* **2018**, *8*, 025108.

(60) Han, Q. J.; Wu, W. Z.; Liu, W. L.; Yang, Y. Q. The Peak Shift and Evolution of Upconversion Luminescence from $CsPbBr_3$ Nanocrystals under Femtosecond Laser Excitation. *RSC Adv.* **2017**, *7*, 35757-35764.

(61) Zhang, F.; Zhong, H.; Chen, C.; Wu, X.-g.; Hu, X.; Huang, H.; Han, J.; Zou, B.; Dong, Y. Brightly Luminescent and Color-Tunable Colloidal $CH_3NH_3PbX_3$ (X = Br, I, Cl) Quantum Dots: Potential Alternatives for Display Technology. *ACS Nano* **2015**, *9*, 4533-4542.

(62) Li, J. M.; Yuan, X.; Jing, P. T.; Li, J.; Wei, M. B.; Hua, J.; Zhao, J. L.; Tian, L. H. Temperature-Dependent Photoluminescence of Inorganic Perovskite Nanocrystal Films. *RSC Adv.* **2016**, *6*, 78311-78316.

Chapter 5.

Summary

In this thesis, we have investigated the effects of interface/surface engineering of nanomaterials on optoelectronic devices such as solar cells and LEDs. We developed a highly versatile catechol-based coating system among various surface treatment methods. The catechol-based nanocoating method changed the surface properties and energy band alignment of nanomaterials. Additionally, we presented a defect engineering method for perovskite nanomaterials with low stability owing to their ionic bonding nature. The density of the trap state was reduced through etching-driven surface passivation between perovskite nanomaterials. These works were monitored with systematic analyses, improving the efficiency of optoelectronic devices.

In Chapter 1, we briefly introduced types of nanomaterials and their unique properties resulting from high surface-area-to-volume ratios. After then, the representative surface/interface engineering methods, such as encapsulation of nanomaterials, ligand exchange, and mussel-inspired coating were summarized. Finally, we presented the effects of these treatments on optoelectronic devices.

In Chapter 2, we applied amine-mediated catechol nanocoating to 1D graphene electrodes in OSCs. The intrinsically hydrophobic graphene surface was changed to a more hydrophilic one by a uniform pNE thin film. This surface modification made it possible to cover a typical hole-transporting material uniformly and without pinhole formation. As a result, we fabricated efficient graphene-based OSCs with performance on par with the ITO reference device.

In Chapter 3, we developed a PEM-based ligand exchange method for PGMEA soluble InP@ZnSeS QDs. The defects on the QDs surface were reduced, and PLQY was preserved by more than 75% during ligand exchange by optimizing reaction conditions. This PEM-based ligand system was effective for InP@ZnSeS QDs with various sizes and emission wavelengths. Additionally, the PEM-capped QDs showed high colloidal stability without PLQY degradation in PGMEA.

In Chapter 4, we demonstrated a novel strategy for highly efficient, stable $CsPbBr_3$ QDs via *in situ* surface reconstruction of $CsPbBr_3$–$Cs4PbBr_6$ NCs. A high PLQY of >90% at 470 nm was obtained because octahedron $CsPbBr_3$ QD surface defects were removed by the Cs_4PbBr_6 NCs. The defect-engineered QDs exhibited high colloidal and thermal stability. Blue LEDs fabricated from $CsPbBr_3$ QDs with reconstructed surfaces exhibit a maximum external quantum efficiency of 4.65% at 480 nm and excellent spectral stability.

Acknowledgement

2009 년부터의 UNIST 생활을 마무리하며 그동안 많은 도움을 주신 분들께 감사의 말을 전하고자 합니다. 먼저 2010 년도에 학부 연구생으로 연을 맺어 지금까지 길잡이를 해주신 지도 교수님, 박종남 교수님께 진심으로 감사의 말씀을 드립니다. 항상 부족한 저에게 연구 방향을 제시해주시고 묵묵히 기다려 주셔서 길었던 학위 과정을 무사히 마칠 수 있었습니다. 연구뿐만 아니라 교수님께서 인생 멘토로서 해주신 조언들이 고민이 많았던 20 대를 보내는 데 큰 도움이 되었습니다. 한때, 제가 방황하고 진로에 대한 걱정이 많아 군대에 다녀왔을 때 교수님께서 반갑게 맞이해 주시던 모습을 잊을 수가 없습니다. 자식처럼 제자를 사랑해주신 스승님을 만나 영광이었습니다. 감사합니다. 그리고 박사 논문 심사위원으로 참석해주신 김진영 교수님, 권태혁 교수님, 송명훈 교수님, 정유진 박사님께도 큰 감사의 말씀을 드립니다. 교수님들과 박사님께서 해주신 격려와 조언들이 제 연구를 마무리하고 확장하는 데 원동력이 되었습니다. 말씀해주신 내용들 잊지 않고 사회에 나가서도 중요한 역할을 할 수 있도록 노력하겠습니다.

학위 기간 동안 온종일 함께 생활했던 MCL 구성원분들께도 감사의 인사를 드립니다. 제가 학부생 때 MCL 첫 대학원생으로 입학하셨던 창진이 형, 기철이 형, 대철이 형, 충호 형이 있었기에 지금의 MCL 이 있다고 생각합니다. 고맙습니다, 형들. 그리고 많은 시간을 같이 보냈던 요한이 형, 선영 누나, 도훈이, 진환이, 은별이, 진희, 동우, 태윤이, 임경이, 성원이, 창희, 정식이, 성한이, 백명진 박사님께도 고맙다고 전하고 싶습니다. 힘들 때마다 옆에 계신 선후배님들 덕분에 기운을 내고 문제를 해결해 나갈 수 있었습니다. 그리고 대학원 13 학번 동기 용훈이, 성환이, 현홍이에게 고맙습니다. 같은 어려움에 있음에도 자신의 일보다 먼저 저를 도와주고 배려해준 모습에서 친구로서 많이 의지했고 제게 큰 힘이 되었습니다. 그리고 앞으로 연구실을 이끌어 갈 강용이, Ning, 양필이, 진호, 동일이 정말 고마웠고, 남은 학위 기간 동안 즐겁게 좋은 연구하기를 바랍니다. MCL 구성원분들과 함께한 시간은 조금씩 달랐지만 모두 제 가슴속에 소중한 기억을 남겨 주셨습니다. 감사합니다.

마지막으로 언제나 저를 응원해주시고 지원해주신 가족분들께 진심으로 감사하다고 전하고 싶습니다. 항상 표현은 안 하시지만 걱정해주시고, 보살펴주신 부모님의 사랑이 없었다면 학위 과정을 이겨내지 못했을 겁니다. 부모님께서 주신 사랑에는 부족하겠지만 평생 부모님께 효도하며 받은 사랑을 갚아 나가는 큰아들이 되겠습니다. 그리고 추운

강원도에서 나라를 지키느라 고생하는 동생 대중이, 대중이와 주환이를 돌보느라 고생 많으신 제수씨, 쑥쑥 자라고 있는 복덩이 조카 주환이도 고맙습니다. 다들 건강하고 앞으로 좋은 일들만 있기를 바랍니다. 사랑합니다.

박사 졸업의 마무리 단계에서 오랜 학위 과정을 뒤돌아보고, 벅차오르는 감정을 추스르며 감사의 글을 마칩니다.

2022 년 12 월 6 일

김 현 중 올림

Curriculum Vitae

Hyeonjung Kim

School of Energy and Chemical Engineering

Ulsan National Institute of Science and Technology (UNIST)

UNIST-gil 50, Ulsan 689-798, Republic of Korea

Email: khjguswnd@gmail.com

Education

2013.03 – 2023.02	**Ph. D. of Energy and Chemical Engineering** Ulsan National Institute of Science and Technology (UNIST), Ulsan, South Korea Under Advisor Prof. Jongnam Park
2009.03 – 2013.02	**Bachelor of Nano-Bioscience and Chemical Engineering** Ulsan National Institute of Science and Technology (UNIST), Ulsan, South Korea

Military Service

2014.01 – 2016.01	Served and discharged from **Republic of Korea Air Force** as air materials supplier, Sergeant

Research Interests

- ✓ Colloidal synthesis of inorganic nanomaterials
- ✓ Design and synthesis of organic ligands
- ✓ Surface engineering of nanomaterials
- ✓ Optoelectronic applications of nanomaterials

Journal Publication

1. T. Kim, K. Kim, **H. Kim**, and J. Park*, “Synthesis of Homogeneous and Bright Deep Blue $CsPbBr_3$ Perovskite Nanoplatelets with Solidified Surface for Optoelectronic Material”, *Bull. Korean Chem. Soc.* **2022**, *43*, 1007.

2. **H. Kim**†, J. H. Park†, K. Kim, D. Lee, M. H. Song*, and J. Park*, "Highly emissive blue quantum dots with superior thermal stability via in situ surface reconstruction of mixed $CsPbBr_3$–Cs_4PbBr_6 nanocrystals", *Adv. Sci.* **2022**, *9*, 2104660. (†These authors contributed equally to this work.)
3. K. Kim†, **H. Kim**†, and J. Park*, "Bandgap Modulation of Cs_2AgInX_6 (X=Cl, Br) Double Perovskite Nano- and Microcrystals via Cu^{2+} Doping", *ACS Omega* **2021**, *6*, 26952. (†These authors contributed equally to this work.)
4. H. Kim†, **H. Kim**†, S. H. Kim, J. M. Park, Y. J. Jung*, S. K. Kwak* and J. Park*, "Molecularly Smooth and Conformal Nanocoating by Amine-Mediated Redox Modulation of Catechol", *Chem. Mater.* **2021**, *33*, 952. (†These authors contributed equally to this work.)
5. **H. Kim**, K. Kim, H. Kim, D. J. Lee and J. Park*, "Eco-Friendly Synthesis of Water-Glass-Based Silica Aerogels via Catechol-Based Modifier", *Nanomaterials*, **2020**, *10*, 2406.
6. S. Jung†, **H. Kim**†, J. Lee†, G. Jeong, H. Kim, J. Park*, and H. Park*, "Bio-Inspired Catecholamine-Derived Surface Modifier for Graphene-Based Organic Solar Cells", *ACS Appl. Energy Mater*. **2018**, *1*, 6463. (†These authors contributed equally to this work.)
7. J. H. Jung, S. Kim, **H. Kim**, J. Park*, and J. H. Oh*, "High-Performance Flexible Organic Nano-Floating Gate Memory Devices Functionalized with Cobalt Ferrite Nanoparticles", *Small* **2015**, *11*, 4976.

Awards and Honors

2013.03 – Present	**Graduate School Scholarship, UNIST**
2022.07	**Outstanding Poster Presentation Award** 2022 Summer Symposium of the Korean Chemical Society
2009.03 – 2013.02	**Undergraduate School Scholarship, UNIST**

Technical Skills

- ✓ **Synthesis of inorganic nanoparticles**: Schlenk line technique, Ball milling, Furnace
  - Noble metal (Au, Ag)
  - Quantum dots (CdSe, InP, InGaN, ZnSe ...)
  - Ceramic (Fe_3O_4, $CoFe_2O_4$, SiO_2, Aerogel, ZnO, NiO…)
  - Perovskite (ABX_3, $A_2B'B"X_6$…)
- ✓ **Organic synthesis**: Chromatography, RAFT polymerization

- ✓ **Film preparation**: Dip coating, Spin coating, Drop casting
- ✓ **Microscopy for micro/nano imaging**: Optical microscope (OM), Scanning electron microscope (SEM), Transmission electron microscope (TEM), Atomic force microscope (AFM)
- ✓ **Spectroscopies**: X-Ray photoelectron spectroscopy (XPS), Fourier transform infrared spectroscopy (FT-IR), Raman spectroscopy, Nuclear magnetic resonance spectroscopy (NMR), UV-Vis absorption spectroscopy, Photoluminescence spectroscopy (PL), Time-correlated single-photon counting (TCSPC), X-ray absorption near edge structure (XANES), Photoluminescence excitation (PLE), Electron paramagnetic resonance spectroscopy (EPR)
- ✓ **Dispersed nanoparticles analysis**: Dynamic light scattering (DLS), Zeta-potential
- ✓ **Chromatography:** High-performance liquid chromatography (HPLC), Gel permeation chromatography (GPC)
- ✓ **Elemental analysis:** Energy dispersive X-ray spectroscopy (EDAX), Inductively Coupled Plasma (ICP)